UNIVERSITAT POLITÈCNICA DE VALÈNCIA

Escuela Técnica Superior de Ingeniería del Diseño

STUDY ON THE BOX-WING CONFIGURATION IN SWEEP AND RELATIVE POSITION

FINAL PROJECT OF THE

Bachelor's Degree in Aerospace Engineering

MADE BY

Adrián Moreno Romero

SUPERVISED BY

Andrés O. Tiseira Izaguirre

Mario Lázaro Navarro

ACADEMIC YEAR: 2019/2020

Abstract

The main objective of this document is to study the box-wing configuration, represented by tandem fore-and-aft wings joined at their tips. To achieve this objective, the influence of two of the fundamental parameters on the aerodynamic behavior of the airplane is analysed: the sweep angle and the relative position of the wings. In addition, different dihedral angles are also considered during the conceptual design of the aircraft.

In order to carry out the study in a satisfactory manner, avoiding further dispersion in the results, the same wing cross-sectional shape is maintained for both lifting surfaces, as well as the wingspan. Besides, the fuselage is considered to have no influence on the aerodynamic research.

Finally, a preliminary static aeroelastic analysis in regard to the aircraft's wing structure is proposed as possible guide for future projects.

The tools used for the theoretical development of the work are the software STAR-CCM+ ® and MatLab ®, and Tornado, a code for implementing a vortex-lattice method.

The main results focus mainly on both aerodynamic coefficients and aerodynamic efficiency, as well as on the distributions of the velocity and pressure fields. In general terms, it can be concluded that the lift, and induced and parasitic drag aerodynamic coefficients increase as both, fore and aft, wing sweep angles decrease. If the relative height is reduced, lift diminishes, but induced drag is increased. As for the aerodynamic efficiency, it increases if the relative position (both, longitudinally and vertically) between the wings increases.

Resumen

El presente documento tiene como principal objetivo el estudio de la configuración *box-wing*, caracterizada por disponer de alas en tándem unidas por sus extremos. Para llevar a cabo dicho objetivo, se analiza la influencia de dos de los parámetros fundamentales sobre el comportamiento aerodinámico del avión: el ángulo de flecha y la posición relativa de las alas. De manera complementaria, también se examinan distintos ángulos diedro durante el diseño conceptual de la aeronave.

Para efectuar el estudio de manera satisfactoria y sin mayor dispersión en los resultados, se mantiene un mismo perfil alar en ambas superficies alares, así como también la envergadura. Además, se considera que el fuselaje no tiene incidencia sobre la investigación de la aerodinámica.

Finalmente, se propone un análisis aeroelástico estático preliminar con respecto a la estructura del ala de la aeronave como posible guía para futuros proyectos.

Las herramientas de cálculo utilizadas para el desarrollo teórico del trabajo son los *software* STAR-CCM+ ® y MatLab ®, y Tornado, un código de implementación de un método *vortex-lattice*.

Los principales resultados se centran, fundamentalmente, tanto en los coeficientes como en la eficiencia aerodinámica, así como también en las distribuciones de los campos de velocidades y presión, y el análisis de la divergencia. En términos generales, se puede concluir que la sustentación y los coeficientes aerodinámicos de resistencia inducida y parásita aumentan a medida que disminuyen los ángulos de flecha de las alas, tanto en la delantera como en la trasera. Si se reduce la altura relativa, la sustentación disminuye, pero aumenta la resistencia inducida. En cuanto a la eficiencia aerodinámica, aumenta si se incrementa la posición relativa (tanto longitudinal como vertical) de las alas.

Resum

El present document té com a principal objectiu l'estudi de la configuració *box-wing*, caracteritzada per disposar d'ales en tàndem unides pels seus extrems. Per dur a terme aquest objectiu, s'analitza la influència de dos dels paràmetres fonamentals sobre el comportament aerodinàmic de l'avió: l'angle de fletxa i la posició relativa de les ales. De manera complementària, també s'examinen diferents angles díedre durant el disseny conceptual de l'aeronau.

Per efectuar l'estudi de manera satisfactòria i sense major dispersió en els resultats, es manté un mateix perfil alar en ambdues superfícies alars, així com també l'envergadura. A més, es considera que el fusellatge no té incidència sobre la investigació de l'aerodinàmica.

Finalment, es proposa una anàlisi aeroelàstica estàtica prèvia sobre l'estructura de l'ala de l'aeronau com a guia possible per a futurs projectes.

Les eines de càlcul utilitzades per al desenvolupament teòric de la feina són els *software* STAR-CCM+ ® i MatLab ®, i Tornado, un codi d'implementació d'un mètode *vortex-lattice*.

Els principals resultats se centren, fonamentalment, tant en els coeficients com en l'eficiència aerodinàmica, així com també en les distribucions dels camps de velocitats i pressió, i l'anàlisi de la divergència. En termes generals, es pot concloure que els coeficients aerodinàmics de sustentació i resistència induïda i paràsita augmenten a mesura que disminueixen els angles de fletxa de l'ala. Si es redueix l'alçada relativa, disminueix la sustentació, però la resistència induïda augmenta. Pel que fa a l'eficiència aerodinàmica, augmenta si s'incrementa la posició relativa (tant, longitudinalment com verticalment) entre les ales.

Acknowledgements

I would like to thank Professor Andrés O. Tiseira for his expert and helpful advice, as well as Professor Mario Lázaro for his valuable feedback during the preparation of my final degree project.

My sincere thanks are extended to Pablo, Guillermo and my many other friends, who have helped me along the journey of my project. Especially to Noelia, who went through hard times together and celebrated each accomplishment. I want to acknowledge your friendship and how much it means to me.

I also want to thank those who ever told me useful critiques and those who ever taught me something positive.

Finally, I wish to acknowledge with sincere gratitude and appreciation my family for the support and encouragement provided throughout the development of this challenging research. They stood by me during every struggle, so none of my successes would have been possible without them.

Contents

List of Figures

List of Tables

Notation

Relevant parameters		
AR	Aspect ratio	-
AoA	Angle of attack	^{o}
b	Wingspan	m
C_{D_i}	Induced drag coefficient	-
C_L	Total lift coefficient	-
C_{L_α}	Lift-curve slope	-
D_i	Induced drag	N
e	Span efficiency factor	-
EI	Sectional stiffness at flexion	$N{\cdot}m^2$
GJ	Sectional stiffness at torsion	$N{\cdot}m^2$
h	Vertical stagger	m
L	Length	m^2
l	Characteristic length	m
M	Mach number	-
q	Dynamic pressure	N/m^2
S	Surface	m^2
t/c	Thickness-to-chord ratio	%
V	Speed of the fluid/aircraft	m/s
x	Longitudinal position	m
x/c	Relative position of the thickness-to-chord ratio	%

Subscripts	
AC	Aerodynamic centre
aft	Rearward wing
bi	Biplane configuration
box	Box-wing configuration
eff	Effective
fore	Forward wing
m	Maximum
mono	Monoplane
NP	Neutral point
ref	Reference
wet	Wetted

Greek alphabet		
Γ	Dihedral/anhedral angle	^{o}
Λ	Sweep angle	^{o}
α	Angle of attack	^{o}
ε	Downwash	-
μ	Dynamic viscosity of the fluid	$N{\cdot}s/m^2$
ρ	Density of the fluid	kg/m^3

Chapter 1

Introduction

1.1 Motivation

The aviation sector, among others, is responsible for more than the 2 % of the total greenhouse gas emanation. Regarding the CO_2 emissions, it accounts for the 12 % of the transport modes, and, during the current year, they are known to be around a 70 % higher than in 2005. This aggravated growth rate has involved EC (European Commission), in co-operation with ICAO (International Civil Aviation Organization), to set some demanding goals, such as reducing the emissions by a 50 % before 2050 and stabilising them from 2020 onwards through carbon-neutral growth. Otherwise, if no further preventive actions are taken, it has been foreseen that they could even escalate up to a 300 % [1].

In fact, global greenhouse gas emissions, mainly carbon dioxide emissions from the burning of fossil fuels, have significantly risen for the last decades, aggravating global warming (Figure 1.1).

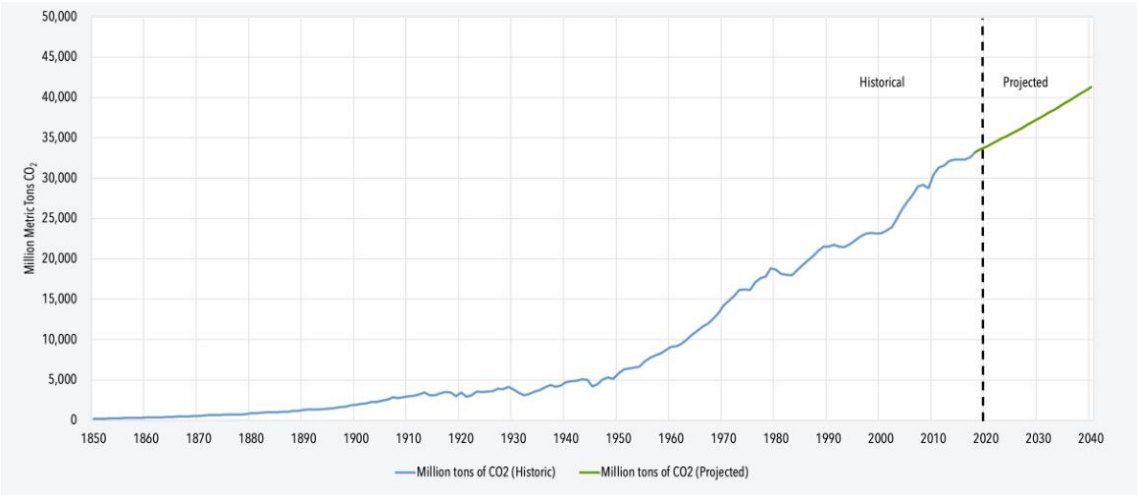

Figure 1.1: Evolution of the global carbon dioxide emissions [2].

Despite the fact that the most effective measure of reducing aviation emissions would be to cut the development of the industry, it is essential for the world economy that it remains viable. Hence, its growth should be maintained. Actually, there are several facts (related to 2019) that demonstrate that it is one of the most relevant industries worldwide [3]:

- Over 65 million jobs are supported in aviation and related tourism worldwide, 10.2 of which work directly in the aviation industry.
- Air transport involves around the 0.5 % of the volume of world trade shipments, but the value of the products is over the 35 %, which means that highly priced assets are more often transported by air.
- The average occupancy of a commercial aircraft is frequently greater than other modes of transport.

After all, to guarantee the feasibility of the aviation industry, aircraft will need to satisfy different requirements in order to increase fuel efficiency, assuring an economically and environmentally sustainable industry.

According to many experts in the aerospace industry, innovative technologies and design practices, as well as new materials, must be considered to meet these requirements, since major optimization of the performance of conventional monoplane configurations seems inconceivable. Therefore, improved engines, enhanced aerodynamics and lighter materials could help aircraft producing less CO_2. In fact, a drag reduction of approximately 1 % can save around 400,000 L of fuel, or the equivalence to 5,000 kg of emissions per year [4]. That is why engineers are looking for unconventional solutions for the future of aviation.

Several aircraft configurations, such as the Boeing Truss-Braced Wing (a high aspect ratio wing aircraft), the Blended Wing Body aircraft, or the box-wing geometry (a closed system with non-planar wings), are amongst the most relevant concepts proposed by researchers (Figure 1.2). In particular, the fundamentals of aerodynamics regarding the latest configuration mentioned are considered in the present project to reduce emissions by reducing fuel consumption, since it can diminish the induced drag and increase the aerodynamic capabilities, without requiring an increase in the aircraft's dimensions.

(a) Truss-Braced Wing. (b) Blended Wing Body. (c) Box-wing.

Figure 1.2: Non-conventional aircraft configurations.

Therefore, the study of non-conventional aircraft with non-planar lifting surfaces is of significant interest, providing a trade-off among aerodynamic efficiency, structural effectiveness and weight savings.

1.2 Objectives

1.2.1 General objective

The aim of this thesis is to analyse the effect of the sweep angle and the relative position of the wings as influential parameters in the conceptual design of a box-wing configuration, carrying out a parametric study using mathematical software and Computational Fluid Dynamics (CFD).

1.2.2 Particular objectives

- Design of a box-wing configuration considering the fundamental data from different theoretical investigations.
- Advanced analysis of the geometry with the help of MatLab ®.
- Study of the aerodynamics by means of the vortex lattice method Tornado and the CFD software STAR-CCM+ ®.
- Introduction to the static aeroelastic problem of divergence for a future implementation in a real scale model.

1.3 Potential applications

The use of the joined-wing layout may be interesting in many applications as a consequence of the outstanding benefits it exhibits (Figure 1.3). The fact that some of the bending moments generated on the front wing are supported by the rear wing allows, on the one hand, to reduce the weight of the structure, increase the wingspan, or a combination of both; but, on the other hand, if the lifting properties are maintained in comparison to a conventional design, it is possible to reduce the dimensions of the lifting surfaces.

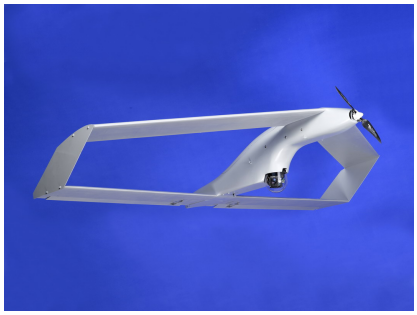

(a) Innocon's Micro-Falcon UAV.

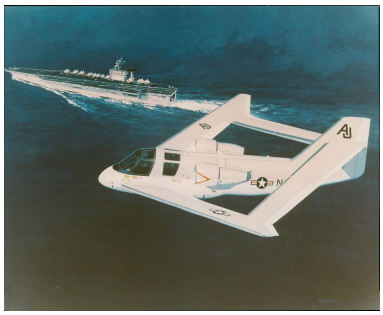

(b) Boeing EX.

(c) GBU-39/B I.

Figure 1.3: Potential applications of the joined-wing configuration.

A joined-wing configuration can provide an unmanned aerial vehicle (UAV) with a more compact structure, reducing the weight and increasing the aerodynamic performance through high aspect ratio wings.

Another fundamental consideration attainable with this unconventional geometry comprehends surveillance aircraft. The arrangement of the wings can be used to improve radar capability with large antennas and sensors in all wings, providing a greater detection range

and full azimuth coverage with no aerodynamic penalty.

Furthermore, high-altitude platforms (HAPs), which are aircraft that usually operate in the stratosphere performing remote sensing, display very-high-aspect-ratio wings that may involve unacceptable low flutter speeds. The rigidity of the joined-wing layout can significantly increase the flutter speed, thus avoiding the issue.

Some hazardous missions, such as aerial fire fighting, require aircraft designs in which robust structures can be more important than aerodynamic efficiency, in order to enhance safety [5]. The structural rigidity required can be provided by the joined-wing configuration.

There are also advantages offered by the joined-wing geometry in range, maneuverability, and terrain-following capabilities for cruise missile configurations.

1.4 Methodology

A first approach to the final box-wing model under development is achieved after performing a broad research of similar already existing concepts. Relevant data is collected and used for scatterplots, in which correlations between different variables are established.

Once general trends are found, the geometry factors that appear to be more convenient for the design of the prototype are implemented in MatLab ®, so as to calculate the lift and drag coefficients, as well as an approximate solution for the aerodynamic efficiency. From the original parameters, the sweep angles and the dihedral/anhedral of both, the fore and aft wings, are altered to determine which combination determines the best aerodynamic performance.

Then, the selected geometry is executed in Tornado for further analysis. In this case, the previous parameters remain fixed, but the relative vertical and horizontal position of the wings are changed by relocating the aft wing in different points.

After all, the final model is evaluated by means of a 2-D CFD simulation with the software STAR-CCM+ ®. For that, some longitudinal sections of the wings configuration are considered, so that the aerodynamics of the flow among the airfoils of both wings is analysed.

Eventually, a first contact with aeroelasticity and structural capabilities is established by stating an static aeroelasticity problem in the whole wing geometry.

1.5 Structure of the Thesis

Chapter 2 includes a thorough explanation concerning the convenience of considering the design of the box-wing configuration.

Chapters 3 to 6 show from the very first approach to the final layout of the model under investigation, following the design, estimation and computation processes implemented.

Appendices contain supplementary data and pictures about the geometries that have been subject of the study.

Specifically, the organization of the chapters is the following:

Chapter 1 Introduces the reasons and potential applications for the use of box-wing aircraft. Moreover, the methodology implemented along the document is also overviewed. Establishes the objectives to be accomplished in the present project.

Chapter 2 Provides a general overview of the main theoretical concepts involved in the design of aircraft.

Chapter 3 Sets the flight conditions, and presents the reference aircraft and the most relevant design parameters to understand.

Chapter 4 Examines different layouts through aerodynamic calculations from different perspectives: mathematical, analytical and numerical approach.

Chapter 5 Collects overall conclusions and results from the development of the project.

Chapter 6 Comprises the final wing geometry design.

Chapter 7 States future promising investigations regarding box-wing aircraft.

Chapter 8 Computes the total estimated budget for the development of the project.

Appendix A Provides more precise data for the estimation of the aircraft's parameters.

Chapter 2

Joined-Wing configurations

2.1 Design overview

Non-planar wings, i.e. wings that are not placed within one single plane, offer such a wide range of possibilities regarding geometries and combinations that they show a great potential for the conceptual aircraft design. Indeed, they involve numerous configurations, as biplanes, box-wing and wings with winglets, which may be divided into different categories depending on the aerodynamic characteristics:

- Multiplanes.
- Closed systems.
- Non-planar monoplanes.
- Planar wings with non-planar wakes.

As stated in section 1.1, the proposal for this thesis is a box-wing aircraft; that is, a joined-wing layout enclosed in the closed systems.

A closed wing is defined by two main planes which join at their tips. The joined-wing configuration, which is an unconventional aircraft design that emerge from within the aforementioned concept, consists of tandem fore-and-aft wings that are joined with a structural connection.

As it was the case for the non-planar wings, there also exist different arrangements respecting the joined-wing configurations (Figure 2.1).

The box-wing is composed by two wings with approximately the same span, joined at their tips by a vertical structure (vertical tip fin). The fore wing, often placed at the bottom of the fuselage, is swept back and the aft wing, typically at the top of the vertical stabilizer, is swept forward.

The diamond wing presents a direct junction of the wings placed in the *extrados* of the front wing, which is commonly referred to as the *main* wing, and is located in a lower position than the rear wing.

The strut-braced wing includes a main high wing supported by a lower strut. Several reinforcements (juries) may connect the structure to inboard locations. In that case, the

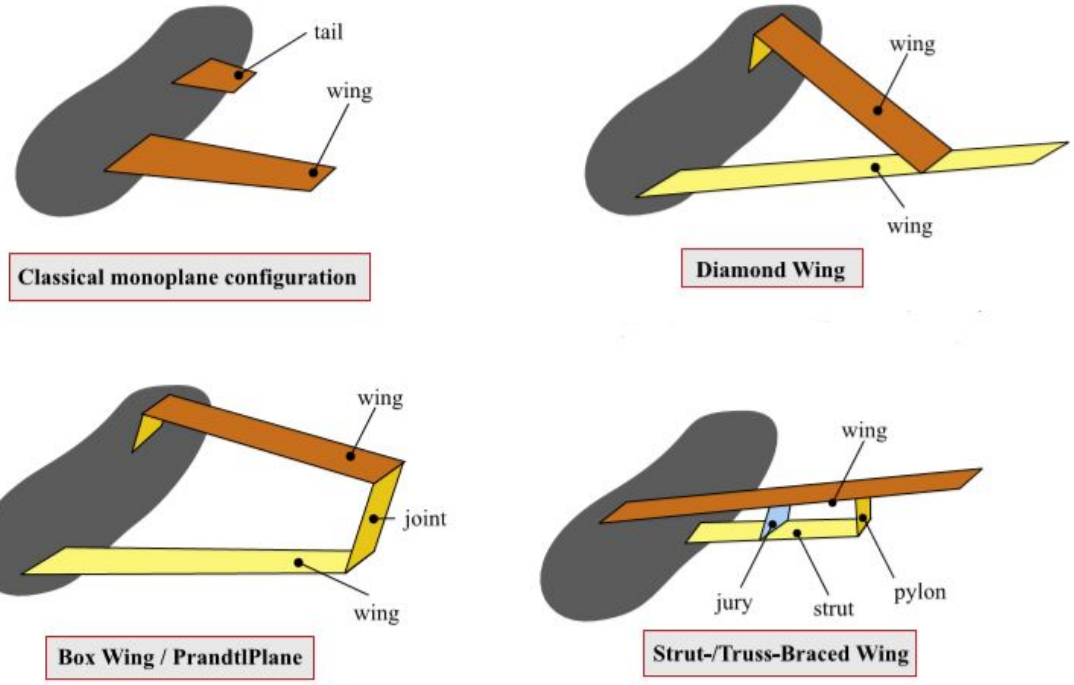

Figure 2.1: Joined-wing layouts [6].

layout is called truss-braced wing.

2.2 Historical background

Back in the days, monoplanes could not resist high wing surfaces due to structural limitations. Hence, multiple wing planes were usual in order to manage to achieve enough lift to perform the proper maneuvers. In fact, a remarkable feature of multiplanes was their high structural efficiency, since the aspect ratio was relatively low, and the struts and wires between planes increased the stiffness of the structure. However, the presence of these rods generated a significant aerodynamic drag, which was even higher due to the existent aerodynamic interference between the different planes, so monoplanes eventually became the most recurrent aircraft.

Still, significant aerodynamic and structural researches of multiplane configurations have been performed for decades now, leading to several interesting concepts, like the closed systems, in which the aerodynamic penalties are minimized. Nonetheless, technical problems regarding aeroelasticity, structural efficiency and certification difficulties invalidated any application of these concepts to commercial production.

Early designs include the Bleriot III (1906) by Louis Blériot and Gabriel Voisin, a glider designed by Reinhold Platz in 1920, and a joined-wing airplane by Ben Brown in 1932.

Further theoretical research was presented by Durand in 1935 about the aerodynamics in a box-wing configuration. In 1954, Cahill performed several wind tunnel tests.

In 1972, Lockheed initiated investigations of the box-wing configuration due to the potential advantages for applications in commercial aviation, freighters and military tankers.

Despite the fact that the box-wing layout was proposed by Prandtl in 1924 as the best wing

system, in terms of reduction of the induced drag with respect to equivalent monoplanes, it was not until the early 1970s that Julian Wolkovitch and Luis R. Miranda (of the Lockheed-Georgia Corporation) designed and patented the joined-wing and box-wing configurations, respectively. Further study was implemented through wind tunnel tests regarding the first geometry, after Wolkovitch proposed to NASA to modify the AD-1, an aircraft with an oblique wing, to test the joined-wing architecture on it, resulting in the first widely studied model (1986).

Aldo Frediani, a professor at the University of Pisa (Italy), was able to demonstrate, back in the 1990s, that the theory proposed by Prandtl was acceptable. That is why, until now, Frediani and his team have started to design a new aircraft prototype, based on the original Prandtl concept of the best wing system: the PrandtlPlane.

Currently, several European researchers are developing new box-wing aircraft models, capable of carrying a greater number of passengers, as well as more cargo, than the actual commercial aircraft, without a significant increase in size or fuel consumption. In fact, according to some calculations and predictions, this type of aircraft would be able to carry up to 100 more passengers, compared to a current common jet of the same size. Likewise, the first models in the industry are expected to start flying around 2035, if all challenges (economically, environmentally and industrially) are far accomplished.

The PARSIFAL project (Prandtlplane ARchitecture for the Sustainable Improvement of Future Airplanes), coordinated by Frediani, aims to open a new path in future aviation with the introduction of the innovative PrandtlPlane, with box-wing configuration. However, it should be mentioned that companies in the aeronautical sector as well known as Lockheed Martin have also proposed prototypes of box-wing models, thanks, to a large extent, to new lightweight composite materials and to developed technology of the landing gear.

2.3 Conceptual background

Several studies and wind tunnel tests suggest that joined-wing aircraft demonstrate aerodynamic and structural advantages [7]:

- Light weight.
- High stiffness.
- Low induced drag.
- Reduced parasite drag.
- Good stability and control.

This joined-wing concept results in a highly integrated approach in which maximum improvements are obtained with an appropriate compromise between aerodynamic and structural design.

2.3.1 Geometric parameters

- **Sweep angle**

Sweep is the angle between the quarter-chord line of the wing and the perpendicular line

to the symmetry plane of the aircraft.

The sweep angle is benefitial for high speed flights as it reduces compressibility effects.

However, the wing system becomes heavier, because the length of the spars of the wing increases, thus increasing weight, but also reducing stiffness. Therefore, the wing must be strengthened, resulting even heavier than the equivalent unswept wing. These wings also happen to be more complex, due to aeroelastic and control problems. The most relevant drawback of aft sweep is the wing tip stall due to the tendency of the boundary layer to flow outwards (there is more suction towards the wing tip); whereas that of the forward sweep is the increased chance of aeroelastic divergence, due to the induced further torsional deflection of the wing under increased lift.

Consequently, caution must be taken when designing a box-wing aircraft, considering that both types of sweep are generally required for describing a proper layout.

Besides, according to Wolkovitch, the outward flow in the boundary layer of a swept-back wing increases the maximum attainable total lift coefficient near the wing root, hence increasing on the entire front wing. Moreover, aft sweep provides a nose-up moment allowing the rear wing to be trimmed at higher total lift coefficients [7].

- **Horizontal stagger and stagger-to-span ratio**

The horizontal stagger (or just stagger) is the relative longitudinal position between the quarter-chord points of each wing. It is positive when the upper wing is ahead of the lower wing, thus closer to the nose of the aircraft. Its non-dimensionalisation with respect to the wingspan gives way to the stagger-to-span ratio.

This geometric parameter is of great interest (refer to subsection 2.3.2) because, there exist a wide variety of publications that show disagreement as to whether the performance of a box-wing design depends on the longitudinal position of the lifting elements or no dependency is found at all (as stated by the Munk's stagger theorem).

- **Vertical stagger (or gap) and height-to-span ratio**

The gap is the vertical distance between the quarter-chord points of the two wings. As was the case with horizontal stagger, the gap's non-dimensionalisation with respect to the wingspan yields to the height-to-span ratio, which is one of the most important design variables for a box-wing configuration. The reason for it to be so relevant is that induced drag decreases if the said ratio increases (Figure 2.2).

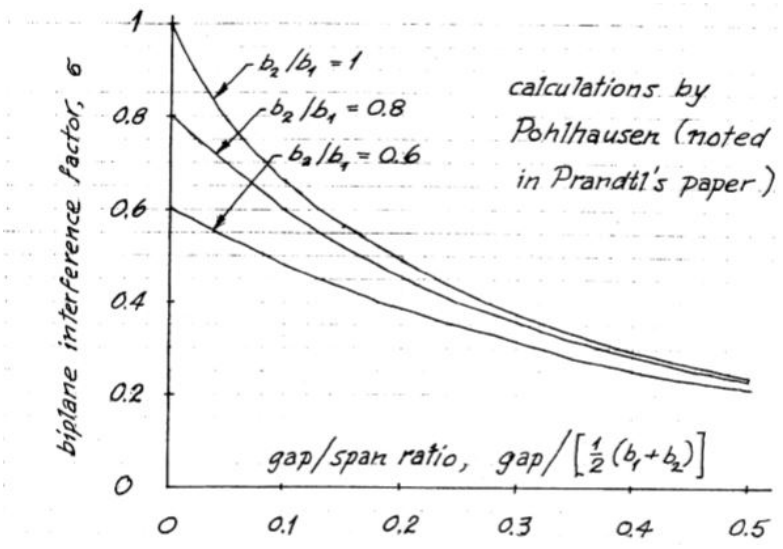

Figure 2.2: Interference factor in biplanes [8].

In fact, this reduction becomes more noticeable as the gap increases, since the interference factor among the wings decreases. In the same way, a shortening of the gap emphasises interference between the two wings, hence raising the overall drag. In particular, the critical distance is found to be at the wing tips [9].

A theoretical infinite gap would reduce the induce drag of the non-planar configuration down to half of that of a monoplane with equal span. However, structural weight and the drag developed due to the vertical fins are some of the limitations to establish proper dimensions of the gap.

- **Span and aspect ratios**

The span ratio is the ratio between the shorter and the longer wing. A specially interesting arrangement is the one in which both wings are the same length, because span can be limited for many reasons; in particular, due to the available hangar width. When span is limited, the minimum induced drag is obtained for wings with equal length.

The aspect ratio is the ratio of the span to the chord for rectangular wings, but the span of the wing squared divided by the reference wing surface for tapered wings.

The Wright brothers found that a high aspect ratio wing has less drag for a given amount of lift than one with low aspect ratio. The reason lies on the 3-D effects caused by the vortex flow pattern generated on the wings. That is, for the same total area, the strength of the vortices is reduced in a high aspect ratio wing when compared to the one with low aspect ratio, since wing tips are further apart, so that the amount of wing affected by the trailing wake is lower. A direct consequence is that high aspect ratio wings do not experience as much of a loss of lift and increase of induced drag as a low aspect ratio wings [10].

Regarding box-wing aircraft, a conventional approach is to define the aspect ratio of the whole wing configuration by means of Equation 2.1.

$$AR_{box} = \frac{b^2}{S_{fore} + S_{aft}} = \frac{b^2}{S_{box}} \tag{2.1}$$

Provided that the wing of a conventional reference aircraft is split into the two wings of the box-wing aircraft, with the further assumptions that the total wing surface and the wingspan remain the same, the reference aspect ratio is equal to that of the box-wing layout.

- **Decalage**

Decalage is the relation between the angle of incidence of the upper and lower wings in a biplane. It is said to be positive when the upper wing is set at a higher angle of incidence than the lower wing, and negative the other way around. In the early years, the selection of decalage was a significant matter, because it influences the distribution of lift, in the sense that positive decalage enlarges the lift of the upper wing with respect to the lower wing.

Nevertheless, a survey of representative biplanes, revealed that typical real designs included no decalage, so the same angle of incidence was generally set to both wings.

- **Wing twist**

Wing twist allows to prevent stall at the wing tips and to modify a given lift distribution so that it resembles the optimal theoretical elliptic distribution.

There exist two different ways to analyse this parameter: geometric twist and aerodynamic twist. Geometric twist is the change in the airfoil's angle of incidence with respect to the wing root airfoil. A well-known concept arises from this definition when the airfoil at the wingtip is at a negative angle compared to the one at the wing root: wash-out. Aerodynamic twist, however, is the angle between the zero-lift angle of an airfoil and the one at the wing root. If an identical airfoil is used along the whole spanwise direction, both the aerodynamic and geometric twists are equal.

The effect on the lift distribution depends on the original angle of attack of the wing, which in turn depends on the lift coefficient obtained from the flight conditions at which the wing is flying. Therefore, an optimization of the lift distribution by twisting the wing is valid only at a particular lift coefficient. The greater the twist required to enhance the lift distribution at the design lift coefficient, the worse the performance gets at any other flight conditions. That is the main reason why wings are typically twisted between zero and five degrees [10].

In conclusion, an optimised wing twist requires a laborious study of the wing configuration. In fact, for preliminary design purposes, adequate background data in relation to the planform under study should be used.

In relation to box-wing aircraft, wing twist plays an important role on the Munk's stagger theorem (subsection 2.3.2).

- **Dihedral angles**

Wing dihedral is the angle of the wing with respect to the horizontal reference line when seen from the front view.

Dihedral induces a rolling moment on the aircraft whenever it is banked (i.e. inclined about its longitudinal axis with respect to the horizontal reference line), which is actually caused by a sideslip introduced by the bank angle itself that increases the angle of attack of the lowered wing. The resulting motion is approximately proportional to the dihedral

angle.

Moreover, an increase of the positive dihedral results in greater and destabilizing nose-up pitching moments at stall conditions, whereas an increase of the anhedral (negative dihedral) results in higher stabilizing nose-down moments. Theoretically, the lift-curve slope decreases with increasing positive or negative geometric dihedral (Equation 2.2), but, on contrary, the variation of the lateral force with sideslip increases [11].

$$C_{L_\alpha}|_\Gamma = C_{L_\alpha}|_{\Gamma=0^o} \cdot \cos^2(\Gamma) \tag{2.2}$$

A disproportionate dihedral effect can produce Dutch roll, a combination of oscillatory movements in roll and yaw that occurs when the dihedral effects of an aircraft are stronger than directional stability. To counteract such an undesired motion, the vertical tail area must be increased, with the corresponding weight and drag growth.

Wing sweep also produces a rolling moment due to sideslip, which is negative for an aft-swept wing, creating an additional effective dihedral different from the actual geometric dihedral. About 10 degrees of sweep approximately provide 1 degree of effective dihedral [10]. In the case of a forward-swept wing, sweep produces a negative dihedral effect, thus requiring a higher geometric dihedral in order to maintain the usual directional stability.

The position of the wings on the fuselage is also a relevant parameter in view of the effective dihedral. The most noticeable effect occurs for high-mounted wings, due to the fact that the airflow over the top of the fuselage lifts the forward wing, providing an increased dihedral effect.

The static directional stability of joined-wing models is very strong as compared to the dihedral effect in maintaining lateral stability, so no tendency to Dutch roll is found at all. Directional stability also appears to be acceptable [7]. Per contra, when employing dihedral angles, the ratio of wetted area to lifting area increases with respect to conventional configurations, resulting in an adverse effect called the dihedral cosine effect. All these characteristics can be obtained by adjusting the positive and negative dihedral angles of the front and rear wings.

There are still no methods to select an optimal dihedral angle that accounts for all the effects. Hence, it must be initially estimated from historical data, like so many other design parameters.

- **Taper ratio**

Wing taper ratio is the ratio of tip chord to root chord. It affects the lift distribution in the spanwise direction in such a way that it resembles that of an ideal elliptical distribution, which, according to Prandtl, produces the minimum induced drag.

Even though rectangular wings with an elliptical wing platform are the ideal geometry concerning lift distribution, they are difficult and expensive to manufacture. Then, untapered wings have been quite common in the aviation industry. However, they have excessive chord towards the tip if compared to the ideal elliptical wing, causing about 7 % more lift-induced drag than an elliptical wing of the same aspect ratio [10].

When a rectangular wing is tapered, the undesired effects due to the constant chord are mitigated. Furthermore, an aft-swept wing tends to divert the airflow towards the tips,

thus creating more lift outboard than for an equivalent unswept wing. Therefore, to recover the desired elliptical lift distribution, it is necessary to reduce the taper ratio.

It should also be expected that, if taper ratio increases, the wetted area of the vertical fin increases too, so that aerodynamic performance can be penalised due to the viscous drag generated.

2.3.2 Aerodynamic performance

The aerodynamic analysis is critical in the design phase of a model in terms of determining various parameters of the arrangement, such as the interference drag for evaluating the overall performance, the static margin and loads on the lifting surfaces for subsequent structural calculations.

According to Prandtl [12], a box-wing configuration has the capacity to reach lower values for the induced drag than any other layout (Figure 2.3). This effect is improved when the number of wings is increased towards infinity. However, the design becomes nonviable due to manufacturing issues. Therefore, nearly all researches focus on biplane configurations.

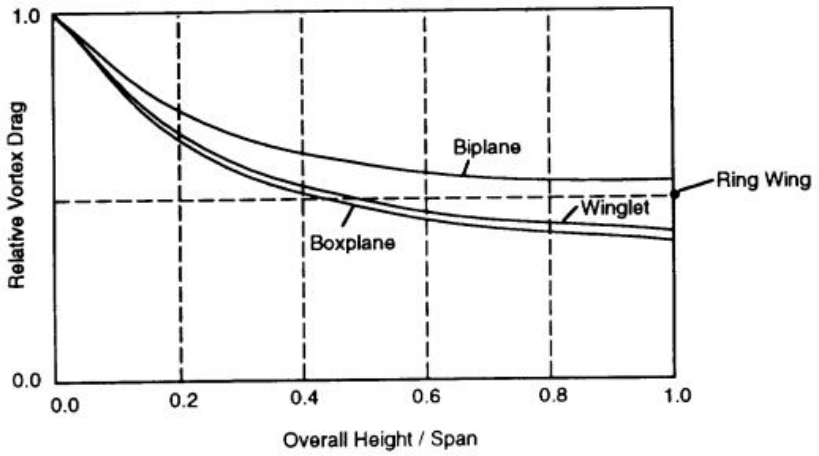

Figure 2.3: Comparison of the induced drag for different wing geometries.

The optimum configuration to achieve the minimum induced drag is obtained for an equal lift distribution on both wings, being the addition of a constant and an elliptical distributions, and a linear distribution on the vertical planes, with a null value near the midpoint. The total lift must also be the same. This wing configuration is known as the Prandtl's best wing system (Figure 2.4).

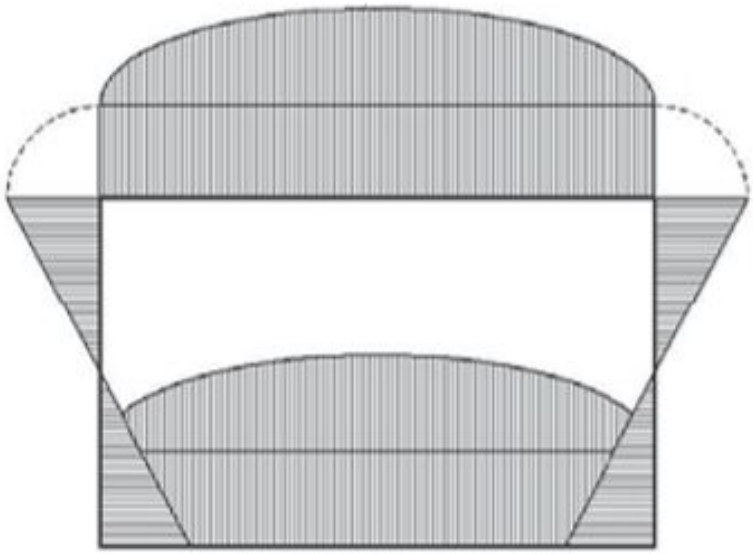

Figure 2.4: Optimum lift distribution of a box-wing aircraft.

The efficiency of a tandem-wing design can be maximised by placing the wings as distant as possible, both in the horizontal and vertical directions [10], and increasing the wingspan.

However, the interference between the wings plays an important role that makes the actual distribution differ from the one expected in theory. The problem arises from the fact that the aft wing perceives the downwash produced by the fore wing, so that the incidence angle of the flow direction may vary substantially. Likewise, the wake of the forward wing also tends to create turbulence, which affects the trailing lifting surface. Furthermore, it is frequent in tandem wing aircraft to place the center of gravity closer to the front to prevent stability complications derived from an imbalanced weight split, thus preventing the aft wing from reaching its maximum lift efficiency.

The lift distribution is prone to change with the stagger, sweep angles, gap, angle of incidence and twist, out of the main parameters to consider. According to Munk [8], if the lift distribution (or circulation) is kept constant, the total induced drag does not depend on the longitudinal position of the components. This theorem is known as the Munk's stagger theorem. Therefore, a box-wing design should be independent of the sweep angles and stagger if the proper span loading is achieved [13]. However, recent analytic studies of the box-wing configuration [14], [15] found that the performance increased with greater stagger, despite the fact that the center of gravity needs to be placed forward in order to allow the aircraft to remain statically stable.

- **Induced drag**

At subsonic speeds, the two most important types of drag are the induced drag and parasitic drag. The induced, lift-induced, or vortex drag, is the drag caused by the generation of lift on a three-dimensional wing.

In contrast to two-dimensional wings (infinite wings or airfoils), a real wing has a finite span, along which its shape may vary (different airfoil or chord), thus producing a change in the circulation and lift, so that its behaviour results more complex. The flow generally deviates from the wingtip to the wing root over the *extrados*, and the opposite way on the

intrados (Figure 2.5 (a)), due to the pressure difference between both sides of the wing, which causes the flow to curl around the wing tips towards the low pressure region on the *extrados*, generating vortices (Figure 2.5 (b)).

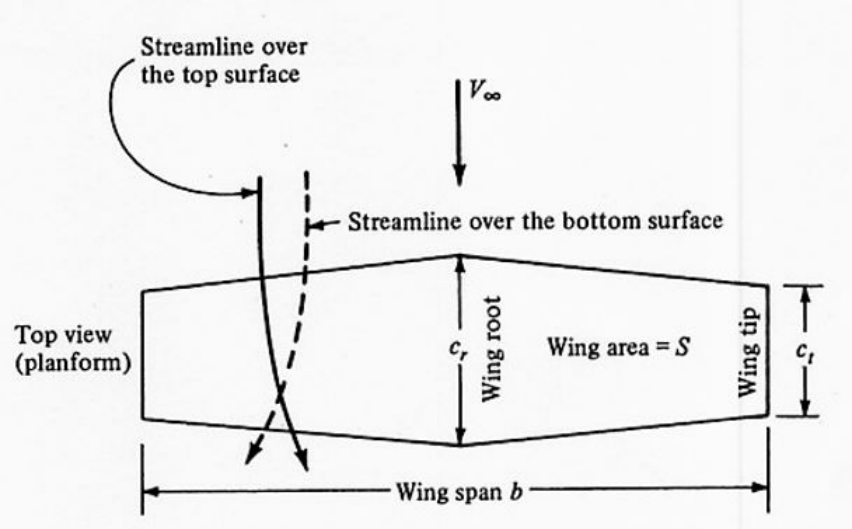

(a) Streamline deviation over and below a wing.

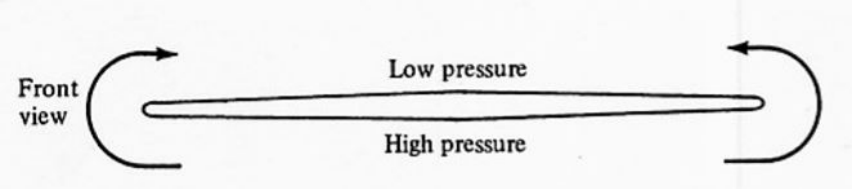

(b) Flow deviation from the *intrados* to the *extrados*.

Figure 2.5: Generation of the wingtip vortices [16].

Vortices trail downstream forming a wake that induces a descending velocity component on the surrounding freestream velocity (downwash), which is the responsible for the induced drag. In fact, it is the energy derived from these vortices that is extracted as a drag force. If these trailing vortices are evaluated as a series of semi-infinite straight line vortices, the Prandtl's lifting line theory arises, which allows to calculate the effect of the downwash, thus predicting a reduction in the amount of lift at a given angle of attack when compared to a theoretical two-dimensional wing using the Kutta–Joukowski theorem. This is due to the influence of the added downwash, which reduces the effective angle of attack of the wing (Figure 2.6).

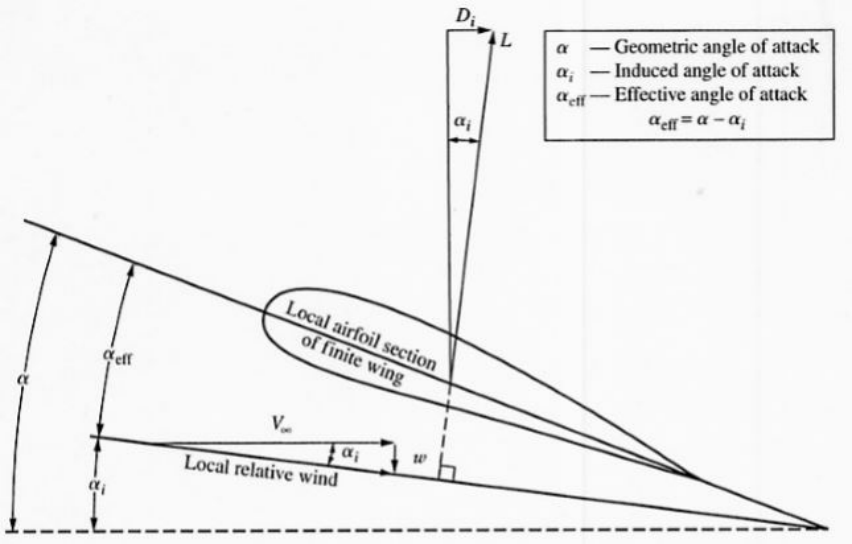

Figure 2.6: Effect of downwash over a local section of a finite wing.

A reduction of the induced drag is essential, because, as stated in Figure 2.7, it comprises about a 40 % of the drag created by a subsonic commercial aircraft. Actually, lift-induced drag is even more significant during take-off and landing conditions, accounting for the 80 % to 90 % of the aircraft's total drag. Despite the fact that these critical stages of flight do not constitute a large fragment of time, they appreciably determine the overall design of an aircraft, since numerous constraints for the aircraft's performance are found. Therefore, an indirect effect on the cruise stage is produced.

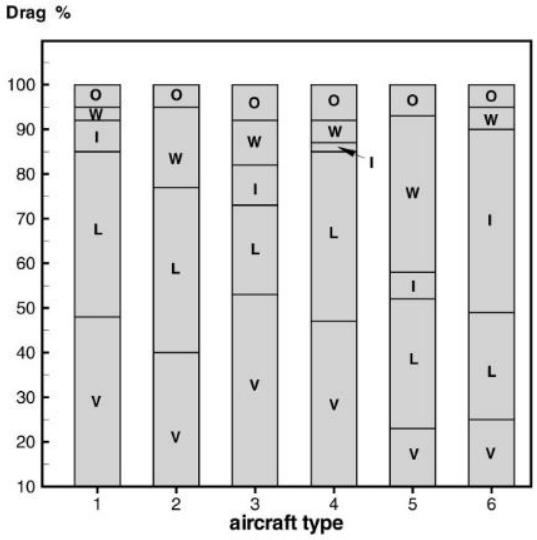

Figure 2.7: Drag build-up: 1. Subsonic transport; 2. Supersonic transport; 3. Executive jet; 4. Fighter at subsonic speed; 5. Fighter at supersonic speed; 6. Civil utility helicopter. Drag causes: L. Lift-induced; V. Viscous; I. Interference; W. Wave; O. Other [17].

To reduce the adverse effects of downwash on current monoplanes, engineers have invented specially design lifting surfaces on the wing tips, called winglets. These devices were broadly studied by Richard Whitcomb, of the NASA Langley Research Center, and their main purpose is to deviate and reduce the vortices, thus reducing induced drag, since they

are not able to completely cancel the vortex wake. Furthermore, their impact on weight and viscous drag must be taken into account to determine the net potential they offer.

The induced drag of a biplane should theoretically be lower than that of a monoplane, considering equal wingspan and the same total lift; actually, it should exactly be halved, if the gap between both wings were large enough so as to consider them separately. The reason lies in the fact that induced drag is a function of the square of the lift that is generated, as well as of the aspect ratio, which is doubled. Hence, if that lift is evenly split between two wings, each wing should produce only a quarter of the induced drag of a monoplane (Equation 2.3). Therefore, the total induced drag of the whole biplane should be only one half of that of a monoplane.

$$\frac{D_{i_{bi}}}{D_{i_{mono}}} = \frac{\frac{{C_L}^2}{\pi \cdot 2 \cdot AR_{ref} \cdot e} \cdot q_\infty \cdot \frac{1}{2} \cdot S_{ref}}{\frac{{C_L}^2}{\pi \cdot AR_{ref} \cdot e} \cdot q_\infty \cdot S_{ref}} = \frac{1}{4} \tag{2.3}$$

Though, interference among both wings prevent the aircraft from taking the full benefit of the ideal concept. That is why adequate biplane designs can grant a reduction in vortex drag of about a 30 % [18].

A closed wing does not either cancel the trailing vortex wake. Nevertheless, these configurations are interesting because if a constant circulation loop is added to a system whose lifting surfaces are horizontally staggered without changing the wake, the lift remains constant and no induced drag penalties are observed, but a pitching moment is generated, providing additional manoeuvrability and trim over different positions for the lift centroid [13].

- **Efficiency factor**

As reported by the lifting line theory, the optimum (minimum) induced drag occurs for an elliptic lift distribution, which can only be obtained with elliptic wings. However, they are rather difficult to be manufactured, so only few existing wings are elliptic.

The Oswald span efficiency factor is a correction factor applied to the classical wing theory computation of the induced drag coefficient of a three-dimensional wing with an ideal elliptical lift distribution, so that the drag due to flow separation is also considered. Assuming a conventional monoplane, the values the efficiency factor may take vary from the maximum value of 1.0 (for an elliptic lift distribution) to any other lower value for different distributions. For a rectangular wing, the efficiency factor is equal to 0.7. Actually, the range of values for the Oswald efficiency factor is typically between 0.7 and 0.85.

If non-planar systems are contemplated, the results for the span efficiency of each design (with equal projected span and total lift, and a height-to-span ratio of 0.2) show a theoretical high potential of induced drag decrease (Figure 2.8). Out of all, the box-wing configuration represents the best solution, although other concepts provide similar drag reductions.

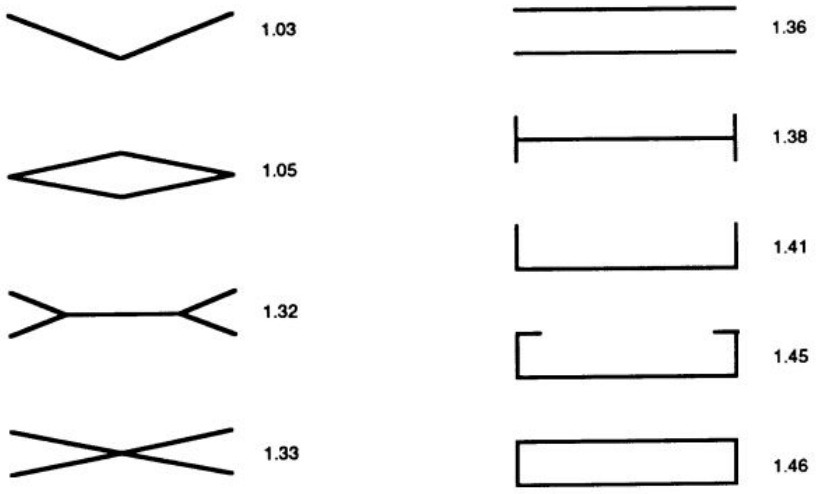

Figure 2.8: Oswald span efficiency factor of non-planar wings [13].

- **Parasitic drag**

The parasite, parasitic or zero-lift drag is the drag which is not related to lift, but rather the one that acts on an aircraft when moving through the atmosphere. It is mostly skin-friction drag, so it is directly proportional to the aircraft's total wetted area (net surface in contact with the surrounding fluid).

For typical commercial aircraft, the parasite drag dominates the total drag during cruise conditions, accounting for approximately 65 % of the total cruise drag [19].

The relative improvement in total drag achieved through induced drag advantages could be remarkably reduced if the parasitic drag coefficient is not enhanced as well, since added wetted area from the vertical tip fins should be dealt with.

In order to lower the parasitic drag in a joined-wing configuration, Wolkovitch recommends to attach the front wing ahead of the maximum fuselage cross-section, so that the wing root is placed in a favorable (or negative) pressure gradient (Figure 2.9). Such pressure gradient enables the motion of the flow, reducing the boundary layer thickness at the wing-fuselage junction. Moreover, filleting is recommended for both wings to minimise flow separation and interference drag.

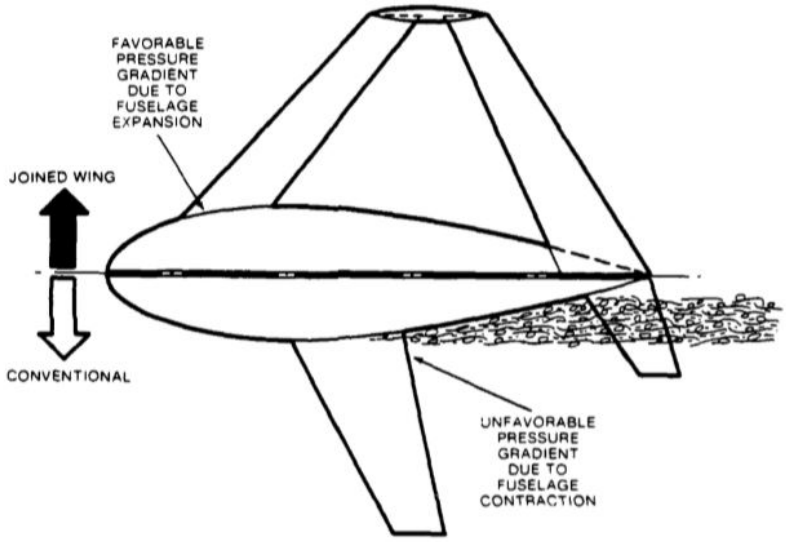

Figure 2.9: Joined wing's front wing attachment in a favorable pressure gradient [7].

Besides, several researches from Bagwill, Selberg, Frediani and Wolkovitch himself, suggest not to overlap both wingtips in plan view to avoid a reduction in the aerodynamic efficiency.

- **Reynolds number**

The Reynolds number (Equation 2.4), ratio between dynamic and viscous forces in a fluid, strongly determines the airfoil characteristics depending on the flight conditions at which it is operating. In particular, the Reynolds number concludes whether the flow is laminar or turbulent, and even whether flow separation occur.

$$\Re = \frac{\rho \cdot V \cdot \ell}{\mu} \tag{2.4}$$

The correlation between wind tunnel tests and real flight data is a tedious issue mainly due to scaling effects, since the wind tunnel Reynolds numbers (partially laminar boundary layers) are often lower than those experienced by the real aircraft, whose boundary layers are fully turbulent. However, viscous forces are dominant for flow regimes with low Reynolds number, so the laminar flow may likely separate by reason of an adverse pressure gradient.

A low Reynolds number regime implies low velocities and low dimensions. In general, these features involve a low friction drag. Nevertheless, in box-wing configuration the wetted surface is enlarged, so the parasite drag become more significant than that of a conventional aircraft, despite the fact that the induced drag decreases. Hence, it is fundamental to determine if the reduction of induced drag is more relevant than the increase of the parasite drag.

Chapter 3

Preliminary requirements

The design of an aircraft contains many different branches of study of aeronautical engineering, such as aerodynamics, structures and propulsion. Therefore, design involves analytical processes and deep studies to properly develop an aircraft (Figure 3.1).

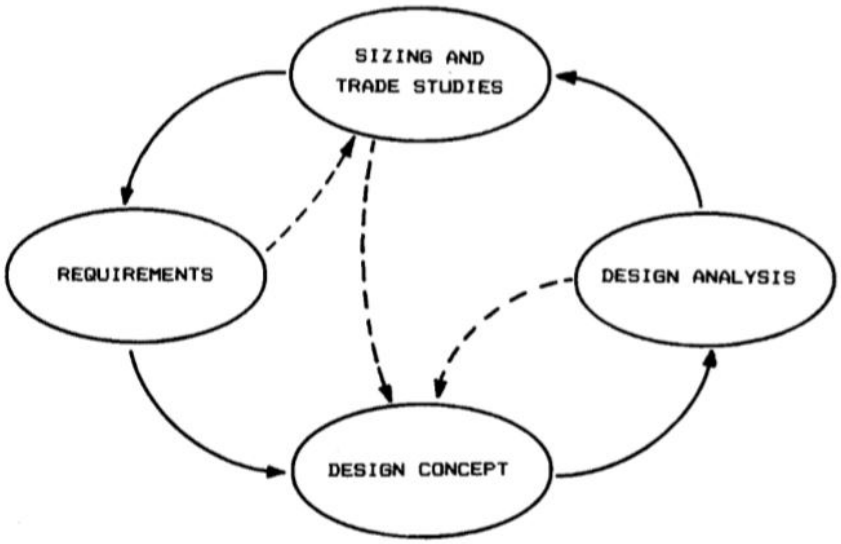

Figure 3.1: The design process [16].

3.1 Geometric constraints

The present project is dedicated to develop and study the wings layout on a box-wing aircraft. In order to do that, several parameters must be fixed according to the author's judgement; otherwise, the large number of existing variables that are required to accurately define a box-wing geometry would make the development too complex to be performed. Therefore, the research is more manageable and the remaining parameters are designed so as to ensure geometric compatibility.

The major assumptions for the conceptual model under study are related to the lifting surfaces. A fixed wingspan of 2 m is set for both wings, which have no wing twist for further simplification, and their surface is maintained constant throughout the whole investigation, so is the aircraft's total lifting surface too. Moreover, the forward wing is placed according

to Wolkovitch's statement, explained in subsection 2.3.2.

With respect to the empennage, no horizontal stabilizer is considered. The main reason is that the main flight control functions are expected to be fulfilled by the wing system. Moreover, not having such an element considerably lightens the total structural weight. In addition, the vertical stabilizer is either not taken into consideration for the aerodynamic estimations, but only for placing the aft wing on top, in order to achieve higher gap-to-span ratios (for the same reason, the forward wing is considered as a low wing). Therefore, the only interesting parameter from the vertical estabilizer is its span, but a deeper study of its design is not needed.

Another design constraint is the simple ogive-like shape chosen for the fuselage to ease calculations to a greater extent, since the aim of the project is to focus on the wings.

Moreover, concerning weight and balance, the overall weight of the aircraft model is initially assumed to be 15 kg, and the static margin is set around 5 to 10 %, just like that of a typical transport aircraft [10].

3.2 Reference aircraft

As a first approach to an initial layout, it is common practice for innovative ideas to analyse and supplement (or even improve) already existing models, so that all the particular requirements established by the designers can be certainly guaranteed.

Significant parameters to be determined from the reference aircraft (some of which are shown in Figure 3.2) appear in Table A.1. It needs to be said that, to achieve firm conclusions, the relevant dimensions have been non-dimensionalised with respect to the overall length of each aircraft for the ease of comparison.

All in all, after evaluating the tendency of each parameter and considering the already previously fixed data for the model, an initial geometry set-up is defined (Table 3.1).

	Forward wing	**Rearward wing**
Wing surface [m^2]	0.46	0.44
Sweep angle [º]	35	-30
Dihedral angle [º]	0	0
MAC [m]	0.25	0.22
Taper ratio [-]	0.43	0.69
Aspect ratio [-]	8.70	9.10

Table 3.1: Initial conceptual design. Significant parameters.

Theoretically, box-wing configurations have low or no dihedral angle at all, so that the front view describes a box shape. Therefore, despite the fact that reference aircraft do have a specific value for that parameter, the basic preliminary geometry is not considered with dihedral nor anhedral angles.

Moreover, the mean aerodynamic chords are approximately calculated through a well-known graphical procedure shown in Figure A.1. For that, a top-view drawing with the wings' parameters of the aircraft is required.

Additional data is the overall length of 2.04 m (slightly larger than the wingspan), the

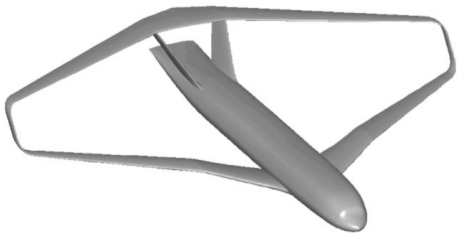

(a) PrandtlPlane [20].

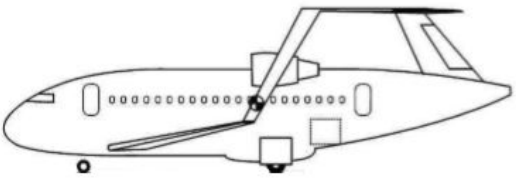

(b) Schiktanz's box-wing configuration [21].

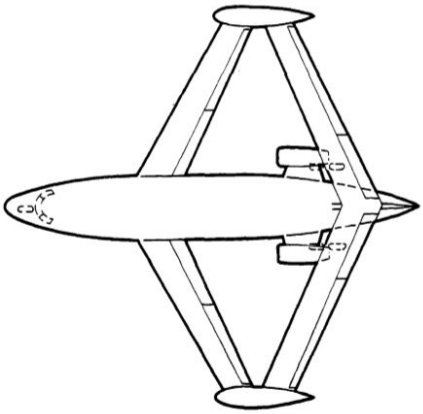

(c) JW-3 [22].

Figure 3.2: Reference aircraft.

maximum diameter of the fuselage at the maximum cross-section (0.29 m), and the span of the vertical estabilizer (0.32 m).

3.2.1 Airfoil selection

In selecting the airfoil sections, several general requirements must be taken into special consideration. The NACA four-digit airfoils are low-drag profiles, but drag and pitching moment increase with lift is reasonably appreciable. Nevertheless, they are cambered sections with relatively high maximum lift and the stalling conditions are quite governable [23].

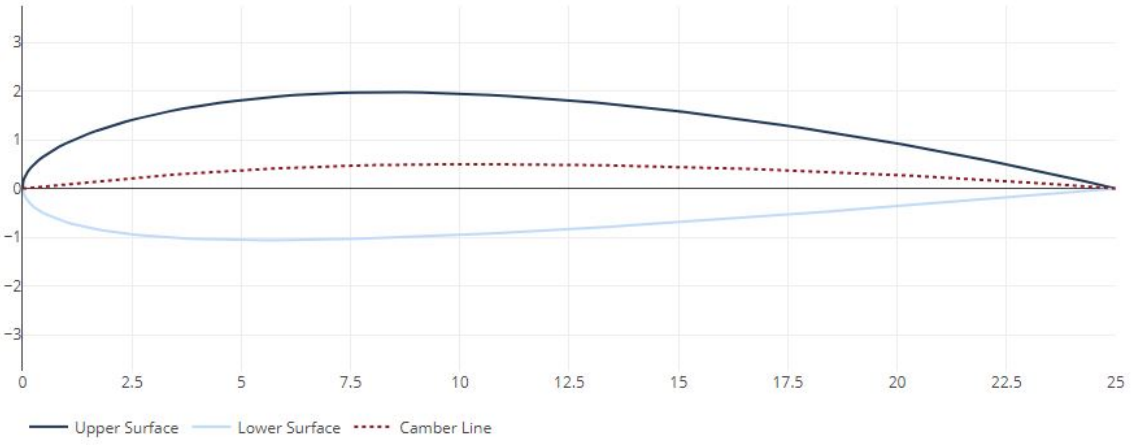

Figure 3.3: NACA 2412 airfoil.

Both wings are provided with a NACA 2412 (Figure 3.3). This choice is also made in line with different biplanes used as reference, such as the BT-120 Mercury, the SMAN Petrel and the Lavel Laco 125. Additionally, this airfoil is used for the Houck Aircraft Configuration, which is a joined-wing UAV.

The vertical fins at both wing tips are provided with a NACA 0012 (Figure 3.4), that is, a symmetrical airfoil. The choice is made due to the same reasons vertical stabilizers are made of these types of airfoils in conventional configurations: at zero angle of attack a symmetric airfoil produces no lift, unless a deflection of the corresponding primary control surface is performed. In this way, no side force is produced, so the plane is more manoeuvrable.

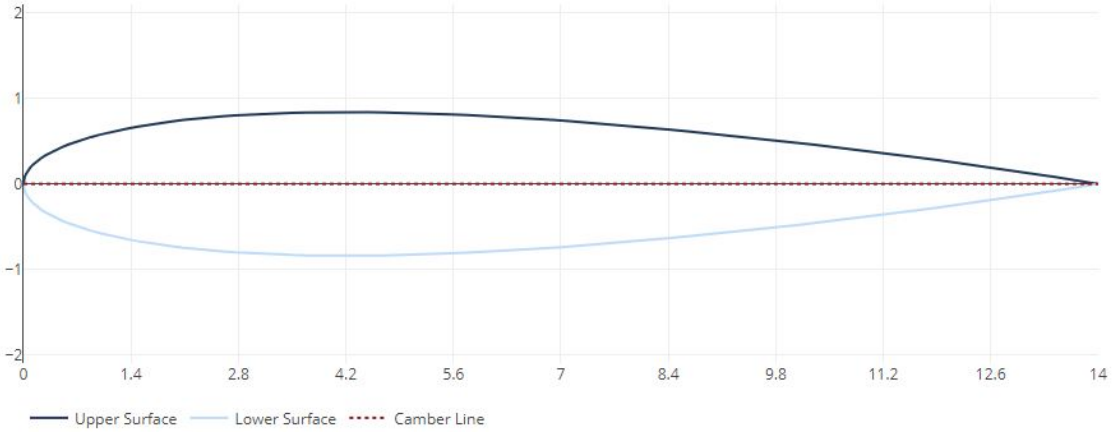

Figure 3.4: NACA 0012 airfoil.

The main parameters of both airfoils are shown in Table 3.2.

$\frac{t}{c}\|_m$ [%]	12
$\frac{x}{c}\|_m$ [%]	30

Table 3.2: NACA 2412 and NACA 0012: main parameters.

3.3 Flight conditions

The most significant simplifying condition is the evaluation of only one cruise design point. Hence, any relevant data that can be obtained from the study is referred to the particular settings in Table 3.3.

Flight speed [m/s]	30
Altitude [m]	500

Table 3.3: Flight conditions.

The fact that the flight altitude is set to approximately 500 m is to ease further comparisons to data that could be obtained from a real experimental model operating at the same conditions, since representative values depend on the state of the air and on the altitude. Furthermore, the flight speed could also be achievable by such a model in both, real flight

and wind tunnel tests (although not implemented in this document). For the latter, the similarity parameters that must be considered for a valid experiment are the Mach and Reynolds numbers. If both, numerical and experimental analysis have comparable values for the similarity parameters, then the relative importance of the aerodynamic forces are modeled properly, so results are reliable.

A fundamental laws of physics in cruise level flight is that lift equal weight. However, the lift produced by the wings does not necessary equal the weight of the aircraft, since the fuselage and other elements are also partly responsible for it. Nevertheless, the current model only considers the wing configuration, so the previous statement is omitted, i.e. wings are fully responsible for the lift generated. As explained in section 3.1, weight is a fixed parameter, so once the aerodynamic approach is implemented, a proper angle of attack for the flight conditions of the aircraft can be established.

Chapter 4

Aerodynamics

Once an initial reference layout is fixed, it is determining to analyse how it behaves and what adjustments can be implemented to significantly upgrade its performance. In first place, the sweep angle is set as a variable in both wings. Hence, several values are tested from among a range of ±15 degrees, five by five (Table 4.1).

Forward wing	20	25	30	35	40	45	50
Rearward wing	-15	-20	-25	-30	-35	-40	-45

Table 4.1: Range of sweep angles (in degrees).

Moreover, in order to perform a deeper evaluation on the effect of the geometry of the wings, the dihedral/anhedral angles are also considered as variables. In this latter case, the range is established at ±10 degrees, respectively, but also five by five (Table 4.2).

Forward wing	0	5	10
Rearward wing	0	-5	-10

Table 4.2: Range of dihedral/anhedral angles (in degrees).

So, combining all possibilities that arise from the sweep and dihedral angles, it follows that a total amount of approximately 400 models are studied. It must be noted that not all geometries are analysed, but only those with negative stagger along the whole wingspan. The reason is to avoid further interference between the wings in the spanwise direction.

In general terms, the following chapter includes the most relevant conclusions derived from the aerodynamic approach implemented in MatLab ®, Tornado and STAR-CCM+ ®, as well as the preferred alternatives for the future development of a real scale model.

4.1 Mathematical and analytical approach

The first development comprises the MatLab ® code implemented so as to get a clearer and more comprehensible idea of how the introduced parameters modify the aircraft's behaviour. For that, specific flight mechanics and aircraft design formulae are evaluated for each case.

4.1.1 Total lift coefficient

The total lift coefficient of a box-wing aircraft comprises the lift coefficients of the forward and rearward wings (Equation 4.1). In addition, the reference surface is a relevant parameter to be determined in order to handle data from both wings. In this case, the whole lifting area of the aircraft (i.e. the addition of the surface of both wings) is used, since both wings are practically identical.

$$C_{L_{box}} = C_{L_{fore}} + C_{L_{aft}} \tag{4.1}$$

Nevertheless, the direction of the free-stream flow velocity must be considered related to the trailing edge of the airfoil. Hence, a conversion for the whole wing is needed considering the effect of the sweep angle (Equations 4.2 and 4.3).

$$C_{L_{fore}} = C_{L_{fore}}|_{\Lambda=0^{\circ}} \cdot \cos^2(\Lambda_{fore}) \tag{4.2}$$

$$C_{L_{aft}} = C_{L_{aft}}|_{\Lambda=0^{\circ}} \cdot \cos^2(\Lambda_{aft}) \tag{4.3}$$

The individual lift coefficient of each wing (unswept) basically comprises the design lift coefficient of the airfoil, determined for specific flight conditions, and the lift curve slope, which depends on the angle of attack (Equations 4.4 and 4.5).

$$C_{L_{fore}}|_{\Lambda=0^{\circ}} = C_{L_0} + C_{L_{\alpha_{fore}}} \cdot \alpha_{fore} \tag{4.4}$$

$$C_{L_{aft}}|_{\Lambda=0^{\circ}} = C_{L_0} + C_{L_{\alpha_{aft}}} \cdot \alpha_{aft} \tag{4.5}$$

- **Design lift coefficient**

This parameter depends on the Reynolds number, which, for the geometry and flight conditions under study, is around 500,000 (refer to subsection 4.1.2), considerably low if compared to that of a typical aircraft's wing (which operates at a Reynolds number of about ten million). Therefore, the value for the design lift coefficient for each wing is approximately 0.3, as can be seen in Figure 4.1.

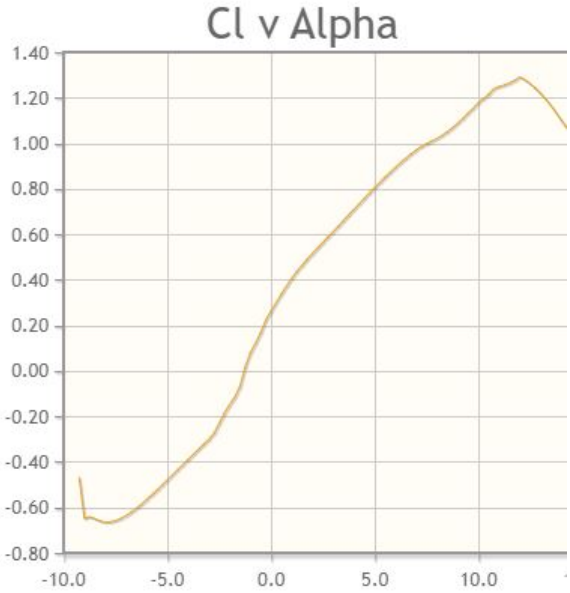

Figure 4.1: Design lift coefficient for the NACA 2412 [24].

- **Lift-curve slope**

The lift-curve slope measures how lift changes as the angle of attack is varied. For the forward wing, this dependence is established in Equation 4.6.

$$C_{L_{\alpha_{fore}}} = \frac{\partial C_L}{\partial \alpha}_{fore} \cdot \alpha_{fore} \tag{4.6}$$

However, the interaction effects among the wings due to the angle of deviation of the airstream are also modelled, but contemplating reasonable simplifications for such an aerodynamic phenomenon, since it can not be accurately calculated from the general aerodynamic theory. Therefore, the aft wing receives the downwash of the forward wing, so its effective angle of attack is reduced, as explained in subsection 2.3.2. Equation 4.7 deals with the aerodynamic behaviour of the rearward wing. In this study, downwash is approximated through Equation 4.8.

$$C_{L_{\alpha_{aft}}} = \frac{\partial C_L}{\partial \alpha}_{aft} \cdot \left(1 - \frac{\partial \varepsilon}{\partial \alpha}\right) \cdot \alpha_{aft} \tag{4.7}$$

$$\frac{\partial \varepsilon}{\partial \alpha} = -\frac{16}{\pi^3} \cdot \frac{\frac{\partial C_L}{\partial \alpha}_{fore}}{AR_{fore}} \tag{4.8}$$

A simplifying assumption is that the upwash of the aft wing is not considered on the forward wing, so that the analysis is much straightforward but still acceptable. Moreover, both wings are supposed to have the same geometric angle of attack, which is set to 1 degree to satisfy the fundamental condition stated in section 3.3.

For each wing, the lift curve slope is given by Equation 4.9. It can be observed that the effect of the dihedral angles is already included, from the relation established in Equation 2.2.

$$\frac{\partial C_L}{\partial \alpha} = \frac{2 \cdot \pi \cdot AR}{2 + \sqrt{4 + AR^2 \cdot \left(1 - M^2 + \tan^2\left(\Lambda|_{\frac{c}{2}}\right)\right)}} \cdot \cos^2(\Gamma) \tag{4.9}$$

4.1.2 Total drag coefficient

- **Parasitic drag coefficient**

There exist several methods that allow to estimate the parasite (zero-lift) drag, such as the equivalent skin-friction method or the component build-up method (Equation 4.10).

$$C_{D_0} = \frac{\sum C_f \cdot FF \cdot FI \cdot S_{wet}}{S_{ref}} \tag{4.10}$$

The latter is a fairly consistent estimation of the subsonic parasite drag of each component of the aircraft through a flat-plate skin-friction drag coefficient (C_f), a component form factor (FF) and an interference factor (FI). As stated earlier in this document, only the wing system is fully modelled, so the components to take into account for the parasitic drag coefficient are both wings and both vertical fins.

Flat-plate skin-friction drag coefficient

The most important factors that affect the flat-plate skin friction coefficient are the Reynolds number, the Mach number and the skin roughness.

In order to account for the influence of the roughness of the surface (Figure 4.2), the cut-off Reynolds number must be evaluated. For the subsonic regime, it is expressed in Equation 4.11.

$$\Re = 38.21 \cdot \left(\frac{\ell}{k}\right)^{1.053} \tag{4.11}$$

Surface	k (ft)
Camouflage paint on aluminum	3.33×10^{-5}
Smooth paint	2.08×10^{-5}
Production sheet metal	1.33×10^{-5}
Polished sheet metal	0.50×10^{-5}
Smooth molded composite	0.17×10^{-5}

Figure 4.2: Skin roughness value (k) [10].

The lower of the actual Reynolds number (calculated as stated in Equation 2.4) and the cut-off Reynolds number should be used to determine the friction coefficient, so that eventually the highest parasitic drag coefficient is calculated. In that way, the worst-case scenario is assessed for the design.

For laminar flow, the friction coefficient is expressed by Equation 4.12; whereas for turbulent flow, Equation 4.13 appears.

$$C_f = \frac{1.328}{\sqrt{\Re}} \tag{4.12}$$

$$C_f = \frac{0.455}{\log_{10}(\Re)^{2.58} \cdot (1 + 0.144 \cdot M^2)^{0.65}} \tag{4.13}$$

After all, an average flat-plate skin friction coefficient must be calculated. This procedure requires to estimate the percentage of laminar flow over each of the surfaces, which mainly depends on the local Reynolds number and the smoothness of the skin. This estimation is determined according to the literature [10]: laminar flow represents typically a 20 % over the lifting surfaces.

Component form factor: FF

Form factors for the lifting surfaces in subsonic regime are calculated as specified in Equation 4.14.

$$FF = \left[1 + \frac{0.6}{\frac{x}{c}\big|_m} \cdot \frac{t}{c} + 100 \cdot \left(\frac{t}{c}\right)^4\right] \cdot \left[1.34 \cdot M^{0.18} \cdot \{\cos(\Lambda|_m)\}^{0.28}\right] \tag{4.14}$$

Interference factor: FI

Parasite drag is increased due to the mutual interference between components. The interference factor for each of the components is based on empirical data [10]. For the wings, the factor is in the range 1.0-1.4; whereas for tail surfaces (or, in this case, the vertical tip fins), a factor of about four (1.04) to five (1.05) percent may be assumed.

- **Induced drag coefficient**

The induced drag coefficient is defined in Equation 4.15.

$$C_{Di} = \frac{{C_L}^2}{\pi \cdot AR_{eff} \cdot e_{box}} \tag{4.15}$$

The effective aspect ratio (Equation 4.16, retaken from Equation 2.1) is a geometric relation obtained by weighing the surface and aspect ratio of both individual wings, without accounting for any aerodynamic coupling. Through this method, an equivalent aspect ratio of the overall geometry is calculated (similar to that of a reference aircraft with the same wingspan).

$$AR_{eff} = \frac{b^2}{S_{fore} + S_{aft}} = \frac{b^2}{S_{box}} \tag{4.16}$$

Moreover, the Oswald span efficiency factor of a box-wing layout allows a potential decrease of the induced drag, since values closer to unity (or even greater) may be achieved. Rizzo and Frediani derived an expression for the ratio between the Oswald span efficiency factor of a box-wing configuration and a reference aircraft based on numerical calculations, from which Equation 4.17 arises. The estimated span efficiency factor for cruise of a conventional aircraft is set to 0.85.

$$e_{box} = e_{ref} \cdot \frac{0.44 + 2.219 \cdot \frac{h}{b}}{0.44 + 0.9594 \cdot \frac{h}{b}} \tag{4.17}$$

4.1.3 Aerodynamic efficiency

The aerodynamic efficiency, or lift-to-drag ratio, of an aircraft is a measure of the overall flight performance. It highly depends on the design of the configuration. It is most directly affected by the wingspan and wetted surface, especially in the subsonic speed regime. In this particular study, the height-to-span and the stagger-to-span ratios are two of the main design variables for a box-wing configuration, which can be directly modified by other geometry parameters, such as the wing sweep and dihedral angles, or the relative position (geometric height and longitudinal separation) of the wings.

These parameters essentially represent a contribution to the overall drag of the aircraft. However, there might well be a trade-off between induced and viscous drag. Therefore, selecting the ideal layout regarding aerodynamics is not a straightforward choice, so a meticulous review of each geometry is performed.

4.1.4 Conclusions

After all possible combinations mentioned at the beginning of the chapter are evaluated, general conclusions in relation to their aerodynamic performance can be derived. First, the effects of sweep on the lift and drag coefficients are evaluated, as well as on the overall aerodynamic efficiency, keeping constant the reference values for the dihedral and anhedral angles of the initial conceptual design, set at 0°.

With regard to the overall lift coefficient (Figure 4.3), a great contribution is provided by the sweep angle. In broad terms, it can be said that, as wing sweep increases (in both, fore and aft wings), the lift coefficient is substantially reduced. Basically, wing sweep flattens the lift-curve slope and it causes the wing to generate less lift per area than a straight wing.

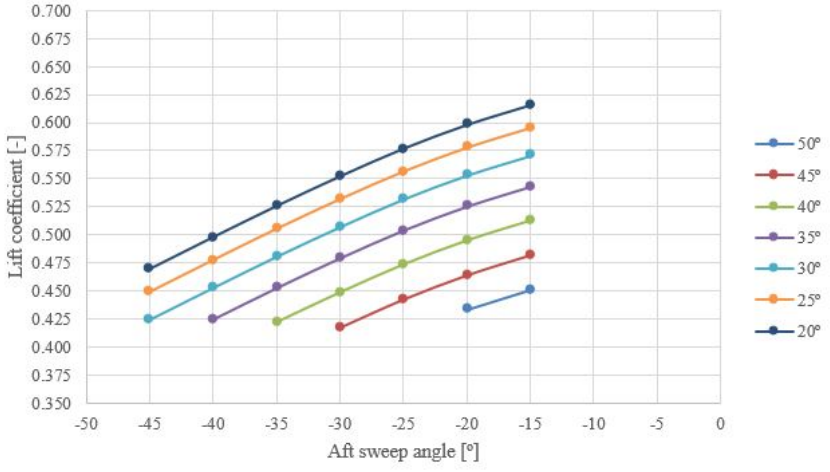

Figure 4.3: Lift coefficient as a function of the sweep angle.

In terms of drag, both the parasitic and induced drag coefficients are evaluated independently (Figures 4.4 (a) and (b)). The lower the sweep angles, the larger the parasitic drag

coefficient. This aspect is evident due to the fact that wings eventually become more distant at the tips, leading to a larger exposed area of vertical fin, the main cause of such an increase in the parasite drag. Regarding the induced drag coefficient, the patterns followed are remarkably similar to those of the total lift coefficient, since sweep reduction causes a gradual increase in drag because of lift. Therefore, further study of the wing twist and lift distribution in biplanes is required to support the Munk's stagger theorem (mentioned in subsection 2.3.2) to achieve the minimum induced drag wing configuration.

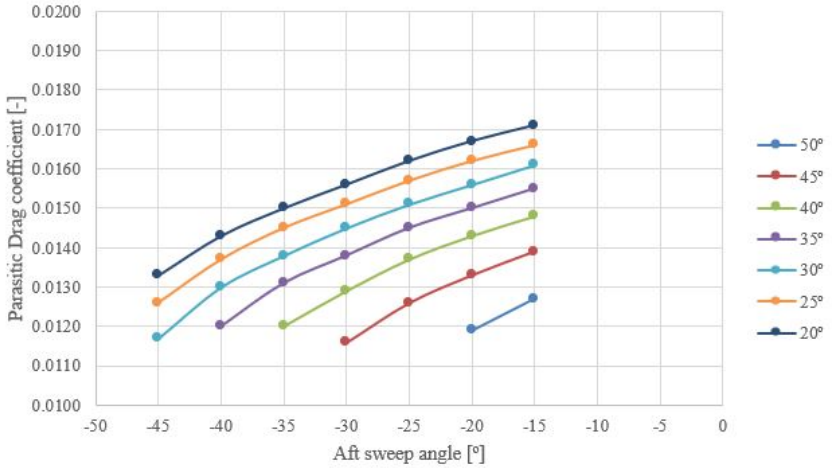

(a) Parasitic drag coefficient.

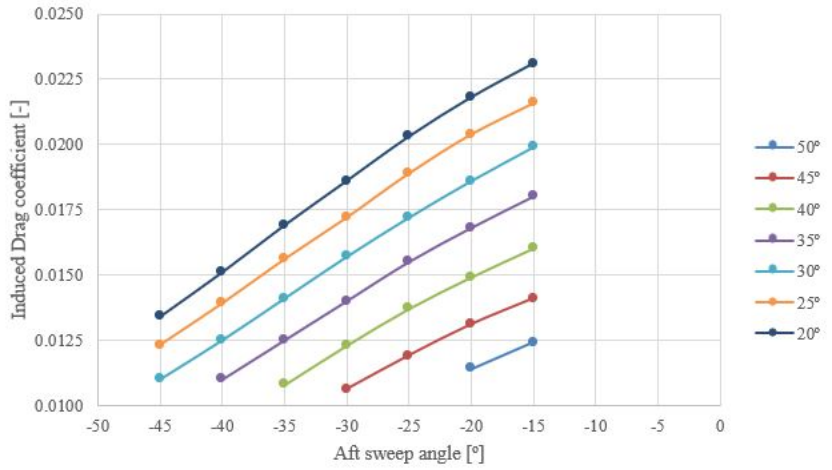

(b) Induced drag coefficient.

Figure 4.4: Drag coefficients as a function of the sweep angle.

Nevertheless, the Oswald span efficiency factor obtained is 1.17, so the induced drag produced in such configurations is definitely lower than the one conventional aircraft with similar features (same aspect ratio and generating the same lift) would cause.

Aerodynamic efficiency is an essential parameter when it comes to flight performance. It is shown in Figure 4.5. Examining the trends of the drag and lift coefficients, and the aerodynamic efficiency, the solid dependency of the latter on the first parameters is specially emphasised. The fact that the lift-to-drag ratio diminishes as the sweep angle is reduced is based on the consolidated growth experienced by both, the parasite and induced drag, which overcome the actual increase experienced by the lift coefficient, as previously mentioned.

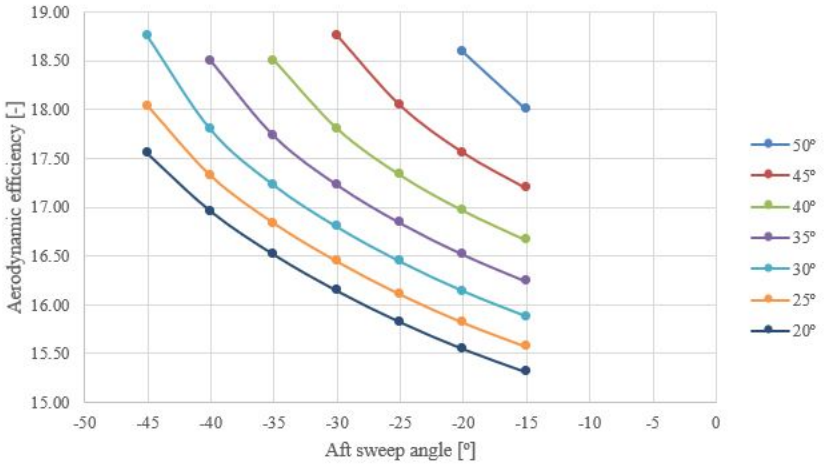

Figure 4.5: Aerodynamic efficiency as a function of the sweep angle.

Despite the fact that there may be more than one possible geometry that offers an exceptional aerodynamic efficiency, a few decisive factors make the selection somewhat easier, like the fact that for enlarging the envelope of the center of gravity the sweep angle of the forward wing should be the highest attainable; on the contrary, the sweep of the rearward wing should be as low as possible. Therefore, the chosen layout is the one in which the fore wing is swept back 45 degrees and the aft wing is swept forward 30 degrees.

Once the sweep angle is fixed, a set of different dihedral and anhedral angles are evaluated on the geometry to broaden the research.

Figure 4.6 depicts the lift coefficient with respect to different dihedral angles. As happened with the sweep angle, dihedral angle also involves a reduction of the lift-curve slope, as stated in Equation 2.2. Nevertheless, such dependency is not visualised at all due to the short range of values considered. That is the main reason why it actually seems that lift is maintained constant for any given dihedral/anhedral angle combination.

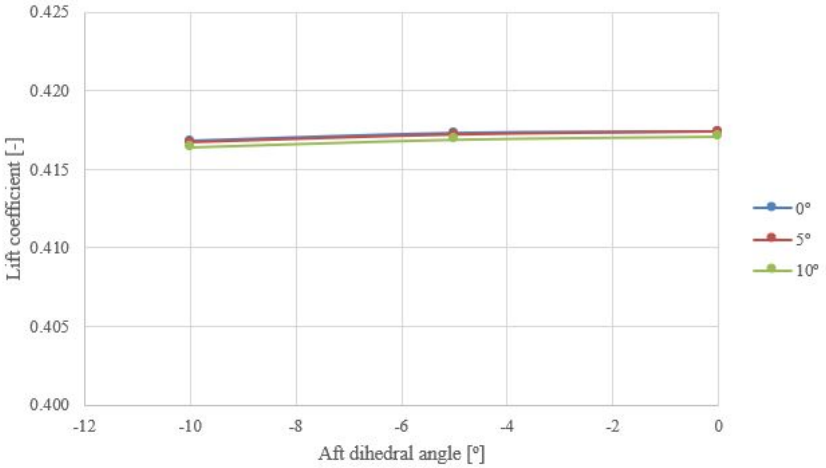

Figure 4.6: Lift coefficient as a function of the dihedral angle.

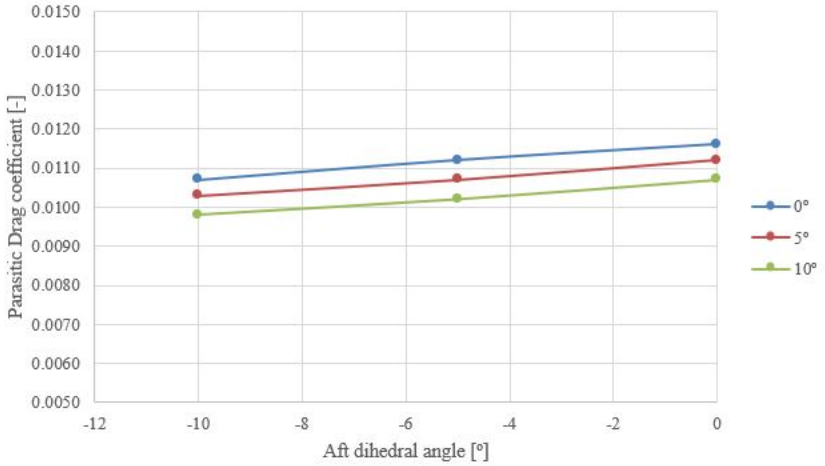

(a) Parasitic drag coefficient.

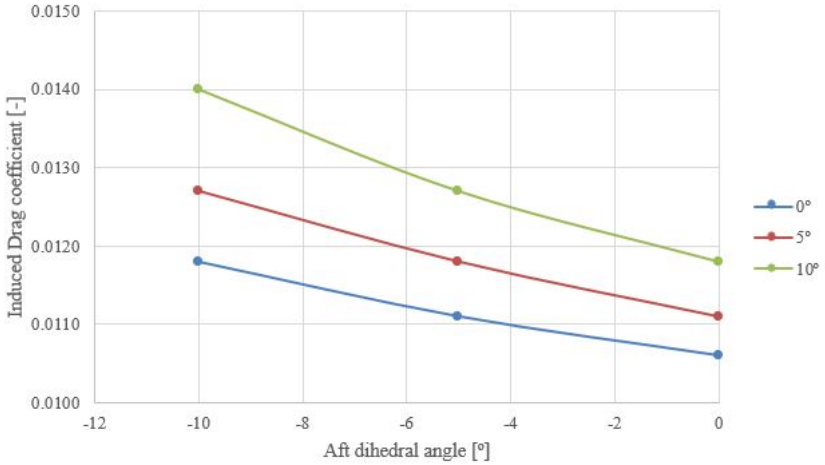

(b) Induced drag coefficient.

Figure 4.7: Drag coefficients as a function of the dihedral angle.

The drag coefficients and aerodynamic efficiency are shown in Figures 4.7 and 4.8, respectively. An increase of the height-to-span ratio along the span (which is equivalent to reduce the dihedral angle) leads to a reduction of the induced drag (Figure 4.7 (b)), since the interference effects among the wings are diminished. On the contrary, the wetted area of the vertical tip fin is increased, and so is the parasitic drag (Figure 4.7 (a)). Nevertheless, according to subsection 2.3.2 and considering the flight conditions established for the analysis, the detrimental effects of viscous drag do not eventually overcome the favourable reduction in induced drag (Figure 4.8).

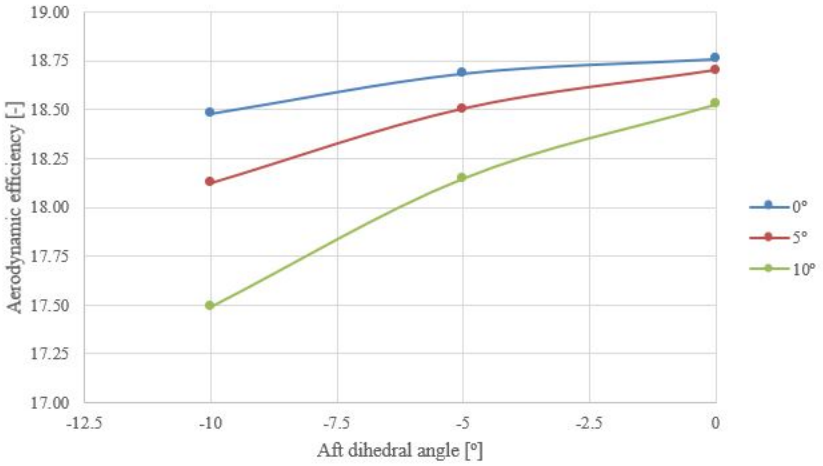

Figure 4.8: Aerodynamic efficiency as a function of the dihedral angle.

In particular, attention is focused on the aerodynamic efficiency. Therefore, the most promising box-wing configuration is exposed (BW-I), including the corresponding sequence for the sweep and dihedral angles in Table 4.3, as well as the stagger-to-span and height-to-span ratios at the tips in Table 4.4.

However, it is still interesting to validate the results obtained not only for the chosen geometry but also for any other, so that the expected trends can be analysed to a greater extent. The additional configuration (BW-II) is selected considering the fact that the aft wing is not directly attached to the fuselage, so it is set as a relevant constraint for the choice of a proper anhedral angle, since it may be the cause of severe structural problems. Therefore, in order not to weaken the wing structure, no anhedral is given to the aft wing. Even though it shows the worst aerodynamic efficiency among the configurations with no anhedral, it will be easier to compare with the BW-I geometry, thus assessing what could be contemplated as upper and lower bounds for the aerodynamic performance, provided by the BW-I and BW-II layouts, respectively.

The supplementary box-wing configuration (BW-II) is also included in the aforementioned tables, together with the BW-I aircraft.

		Sweep angle [º]	**Dihedral angle [º]**
BW-I	**Forward wing**	45	0
	Rearward wing	-30	0
BW-II	**Forward wing**	45	10
	Rearward wing	-30	0

Table 4.3: Sweep and dihedral angles of the selected box-wing configurations: first draft.

	Stagger-to-span [-]	**Gap-to-span [-]**
BW-I	0.023	0.189
BW-II	0.023	0.103

Table 4.4: Stagger and gap to span ratios at the tips of the selected box-wing configurations: first draft.

4.2 Tornado vortex-lattice method

In this section, the relative position of the wings is altered, so new different geometries are created. The procedure is performed in both geometries under study (BW-I and BW-II) by moving the aft wing closer and away from the fore wing a certain percentage of the initial separation (as shown in Table 4.5), but keeping the preselected sweep and dihedral angles constant.

		Relative height [%]				
		+20	**+10**	**0**	**-10**	**-20**
Relative longitudinal separation [%]	**+20**	A	B	C	D	E
	+10	F	G	H	I	J
	0	K	L	M	N	O
	-10	P	Q	R	S	T
	-20	U	V	W	X	Y

Table 4.5: New geometries from the change in the relative position of the wings.

In the preliminar study, every layout that resulted in positive stagger at the wing tips was discarded, so, in order to provide a consistent methodology, even though the number of geometries studied in this section is far more limited, positive stagger is also neglected.

Tornado [25] is a 3-D vortex lattice program that is meant to be used as an additional helpful tool in the conceptual design of aircraft.

The vortex lattice method (VLM) used by Tornado is based on the potential flow theory (linear aerodynamics), so the main assumptions for any analysis are small angles of attack and low Mach numbers. That is, compressibility and thickness effects of the lifting surfaces are neglected, as well as fuselage effects and friction drag. Even so, Tornado allows to design multi-wing layouts with a lot of possibilities for the geometric parameters (such as wing sweep, taper ratio and camber), from which relevant data such as forces acting on each panel or aerodynamic coefficients can be obtained. The mathematical model is composed of a wake trailing downstream from the edge of every lifting surface, which is flexible (it is modified according to the flight conditions) and realigns with the free stream.

In the first place, the aircraft geometry is created. In Tornado, every lifting surface is considered as a flat surface, so there are no actual differences when inputting data for a main wing or a stabiliser. After that, the flight state is set with the flight conditions of the study, so the angle of attack, true airspeed and rotational angular rates (if any) are established.

The geometry is discretised (*meshed*) into several panels distributed over the spanwise and chordwise directions of the planform, and a vortex is associated to each panel, so the panel distribution should be consistent with the geometry of the wings. A cosine-type distribution is generally recommended in the chordwise direction to increase density at the leading and trailing edges, two significant regions of the analysis.

Once the problem is executed, there exists a post-processor menu from which the geometry and data plots are drawn. Among the alternatives, there are a 2-D plot of the planform with the corresponding partitions and panels, a 3-D plot of the geometry layout, and a panel distribution in which the trailing vortices are perceptible.

4.2.1 Total lift coefficient

On account of the difference in the methods used for calculations and the input geometries, the values that Tornado computes for the total lift coefficient differ in approximately a 5 % from those obtained by means of the mathematical and analytical approach implemented in MatLab ® (subsection 4.1.1). The main reason may lie on the lack of accuracy when modelling thickness effects. Still, the output data from Tornado is in agreement with the well-known Prandtl's lifting-line theory.

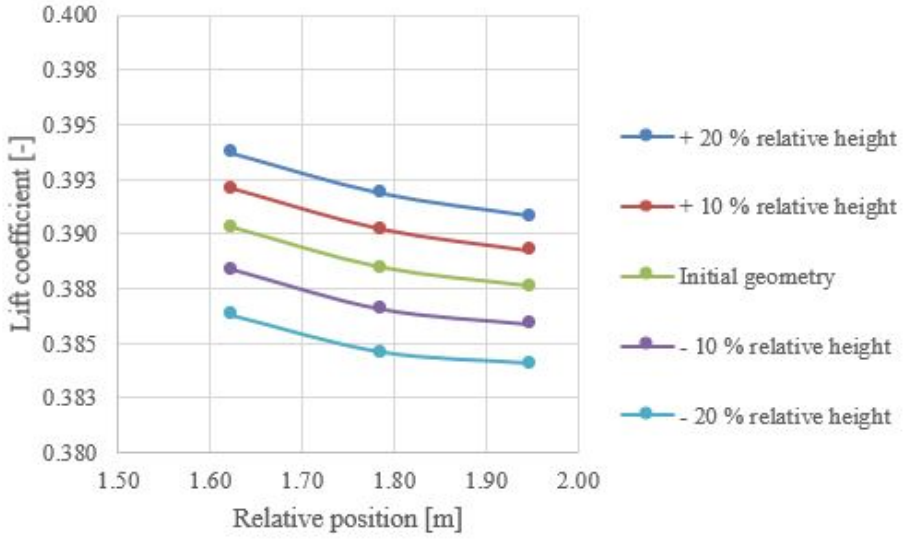

(a) BW-I.

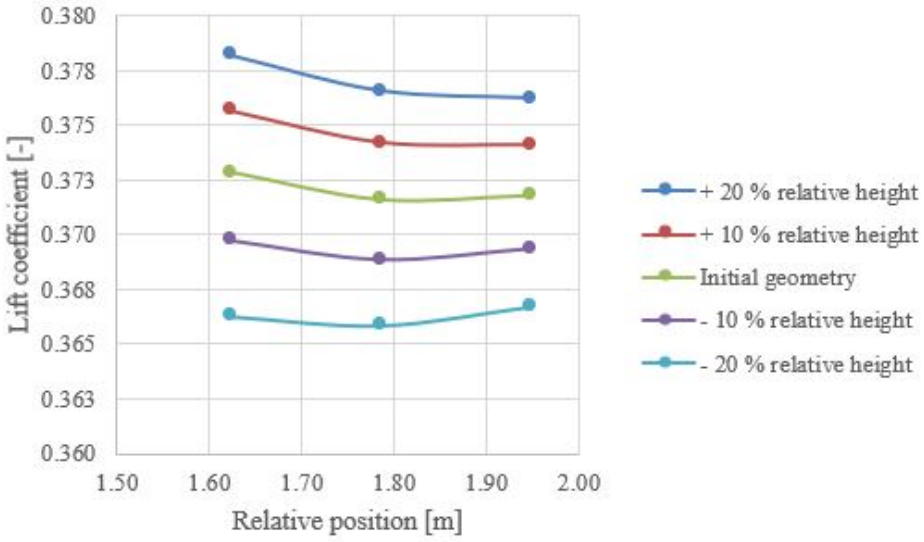

(b) BW-II.

Figure 4.9: Lift coefficient as a function of the relative position of the wings.

Figure 4.9 shows the evolution of the lift coefficient as the relative separation (both vertically and horizontally) of the wings is changed.

In general terms, as the longitudinal distance is increased, the lift coefficient remains practically unaffected, apparently due to the low interaction effects that may appear on the wings at such relative positions, so wings are placed far enough from each other; on

the contrary, the further up the aft wing is placed, the better for the lift coefficient. If both geometries are compared, the BW-I configuration (Figure 4.9 (b)) displays higher values for a given separation of the wings, meaning that the dihedral effect on the wing configuration produces a detriment of the lift generated in about a 4 %.

4.2.2 Total drag coefficient

The total drag coefficient provided by Tornado is much lower than the expected from the analytical resolution, which is expected since no skin friction drag is modeled.

Therefore, no additional analyses are performed on the drag coefficient due to the lack of accuracy.

4.2.3 Pitching moment coefficient

A first approximation to the longitudinal static stability is evaluated on the undertaken geometries to determine whether the pitching moment may be stabilising, destabilising or neutral.

For an aircraft in trimmed position, the total pitching moment is zero. However, if any aerodynamic disturbance in which the angle of attack suffers a sudden change occurs, the aircraft should be able to return to the initial equilibrium position. In order for that to happen, the pitching moment coefficient as a function of the angle of attack (i.e. the damping derivative in pitch) must be negative, so as to get the nose down. That is, the aircraft must be longitudinally stable, so that it recovers the trim position after the disturbance. In other words, a negative pitching moment coefficient involves a nose-down motion that reduces the angle of attack in the absence of any control input, which is an advantageous detail, as the aircraft tends to recover stable flight conditions, rather than the stall unstable conditions.

Longitudinal static stability is quantified in terms of the relative locations of the aerodynamic center of the wings and the center of gravity of the aircraft. There is a particular position of the center of gravity, called the neutral point, where the aircraft has neutral longitudinal static stability. Hence, the neutral point represents a boundary between stability and instability.

There are some basic conditions that should be verified when assessing the static longitudinal stability of an aircraft:

- A controllable aircraft requires a positive pitching moment about the centre of gravity to neutralise the negative pitching moment generated by the wings.

- The slope of the pitching moment coefficient with respect to the lift coefficient (i.e. the damping derivative in pitch) needs to be negative to ensure the stability condition. In other words, the static margin, which is a way of quantitatively indicating the degree of longitudinal static stability of an aircraft (Equation 4.18), must verify that the centre of gravity is ahead of the neutral point of the aircraft.

$$SM = \frac{x_{CoG} - x_{NP}}{c_w} < 0 \tag{4.18}$$

- During trim conditions, the pitching moment coefficient at zero lift should be positive (nose-up).

For the simplified analysis, the lifting surfaces are supposed to be the major contributors.

In box-wing aircraft, the conventional horizontal stabiliser is replaced by an aft wing. Therefore, the third condition mentioned becomes difficult to be accomplished, since the zero lift pitching moment produced by the airfoils of the aft wing is negative, just like for the fore wing, because both lifting surfaces are meant to generate positive lift. Such difficulty results in a more limited range for the centre of gravity. Nevertheless, there are some important requirements that can be fulfilled so as to create a positive zero lift pitching moment [26]:

- A large longitudinal relative separation between both wings.
- Adjustments regarding wing twist and sweep angles.

- **Aerodynamic center**

It has been found both experimentally and theoretically that, if the aerodynamic force is applied at a the quarter chord of a low speed airfoil, the aerodynamic moment remains nearly independent of the angle of attack. This location is called the aerodynamic center of the airfoil.

For trapezoidal wings, the mean aerodynamic centre must be found, since it serves as the average of the whole wing. Hence, the whole computation actually depends on the geometry of the wing.

- **Center of gravity estimation**

The appropriate reference point for the mathematical estimation of the whole aircraft's equilibrium is considered to be the centre of gravity. Consequently, all movements produce a moment (thus, rotations) around the centre of gravity, since it acts as the aircraft's hinge.

As previously stated in section 3.1, the static margin is set somewhere in between that of a typical transport aircraft's range: 5 to 10 %. Hence, from Equation 4.18, an approximation to the actual centre of gravity of the geometries can be obtained, so a further evaluation on which would provide a higher static longitudinal behaviour may be implemented. For that, the neutral point must be approximated beforehand by means of Equation 4.19.

$$x_{NP} = \frac{C_{L_\alpha fore} \cdot \left(\frac{S_{fore}}{S_{ref}}\right) \cdot x_{AC\,fore} + C_{L_\alpha aft} \cdot \left(1 + \frac{\partial \varepsilon}{\partial \alpha}\right) \cdot \left(\frac{S_{aft}}{S_{ref}}\right) \cdot x_{AC aft}}{C_{L_\alpha fore} \cdot \left(\frac{S_{fore}}{S_{ref}}\right) + C_{L_\alpha aft} \cdot \left(1 + \frac{\partial \varepsilon}{\partial \alpha}\right) \cdot \left(\frac{S_{aft}}{S_{ref}}\right)} \tag{4.19}$$

After all, configurations BW-I-A and BW-I-M (which also apply to BW-II-A and BW-II-M, since the longitudinal location of the centre of gravity is not affected by the dihedral angle) are selected and their preliminary drawings are shown in Figure 4.10. The reason lies on the fact that, as one of the previous requirements announced, the further both wings are placed from each other in the longitudinal axis, the easier to fulfil the second (Figure 4.11) and third conditions about static longitudinal stability of aircraft. As a first approach, the BW-I-A configuration is the most potentially beneficial regarding stability, since it registers the highest value for the pitching moment coefficient.

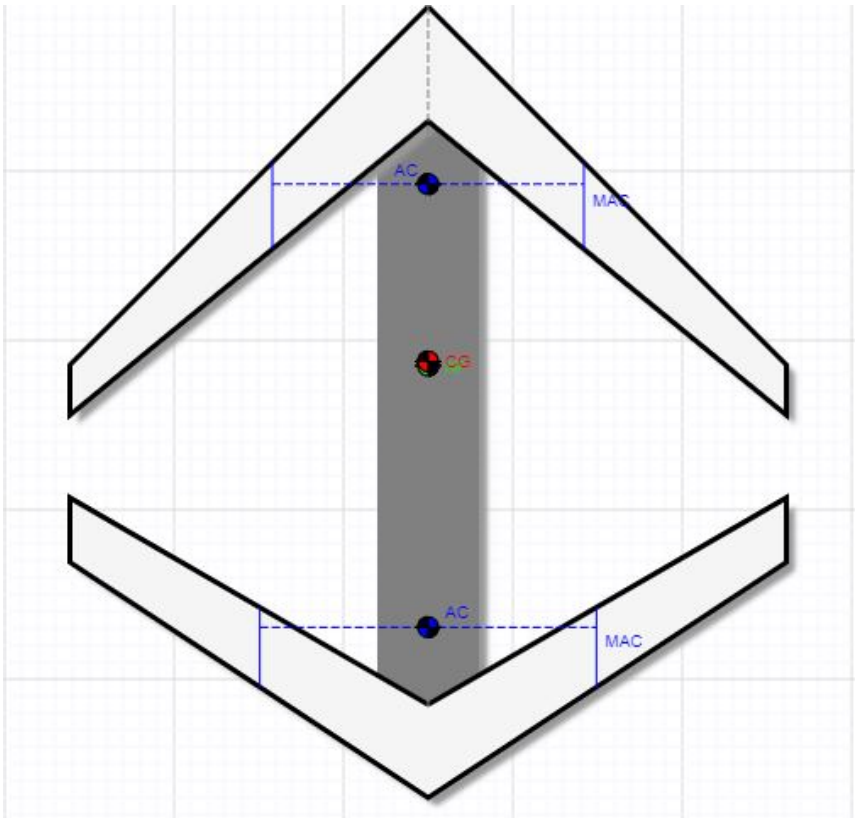

(a) BW-I-A/BW-II-A.

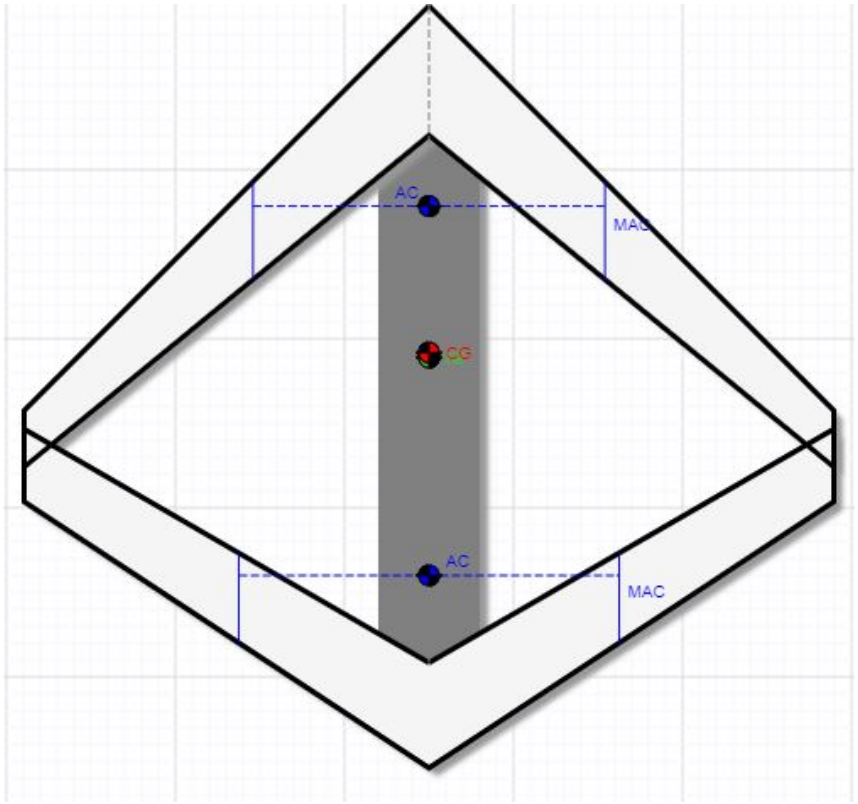

(b) BW-I-M/BW-II-M.

Figure 4.10: Preliminary drawing and centre of gravity estimation.

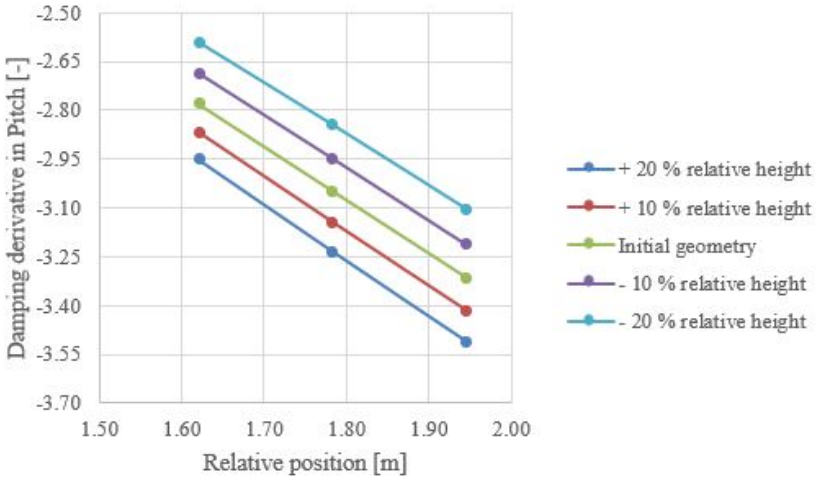

(a) BW-I.

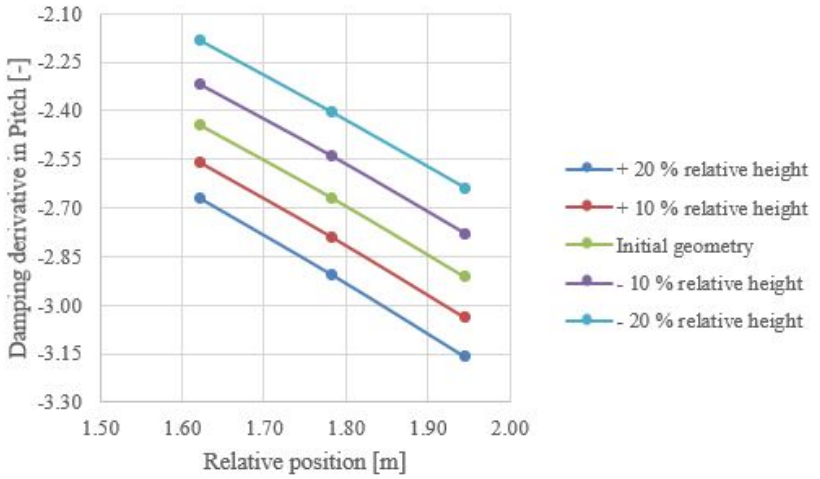

(b) BW-II.

Figure 4.11: Damping derivative in pitch as a function of the relative position of the wings.

Nevertheless, a deeper research regarding stability and control would be required to ensure the proper selection of an optimum wing configuration, since they have not been the subject of detailed investigation.

4.2.4 Pressure field distribution

Tornado provides a first approximation to the pressure coefficient distribution, through the derivative of the doublet strength along the panels, both chordwise and spanwise.

The distribution of pressure is characterised by local air pressures much lower than the atmospheric pressure over the upper surface (negative distribution due to the acceleration of the flow through the higher curvature). As the air flows towards the trailing edge, pressure approaches that of the free-stream flow. On the contrary, positive pressure coefficients represent local pressures higher than the reference atmospheric pressure.

The area enclosed by the distribution accounts for the resultant force coefficient acting on the airfoil. In fact, provided that the angle of attack of the airfoil is known, the lift force

coefficient can be calculated as the integral of the difference in the pressure distribution over the airfoil.

Figures 4.12 and 4.13 show the difference in the distribution of pressure between the upper and lower surfaces of the wings of the four geometries considered.

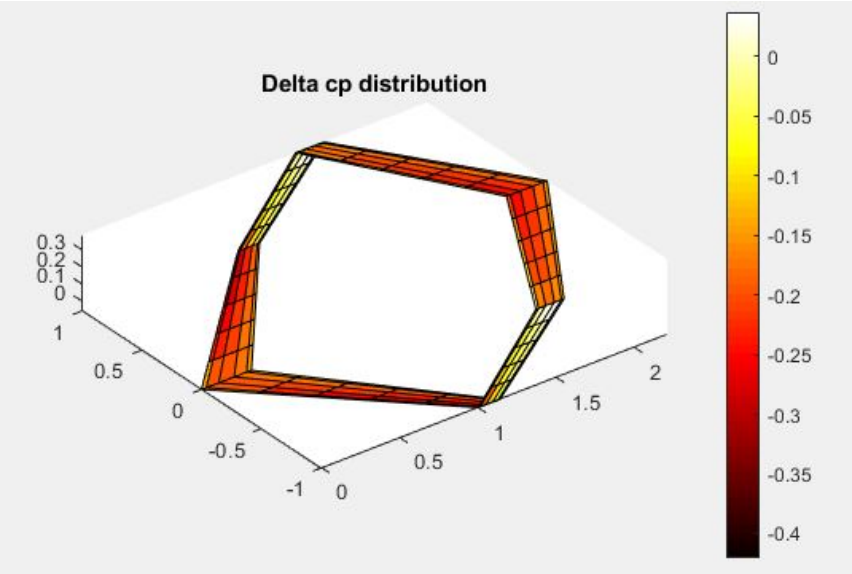

(a) BW-I-A.

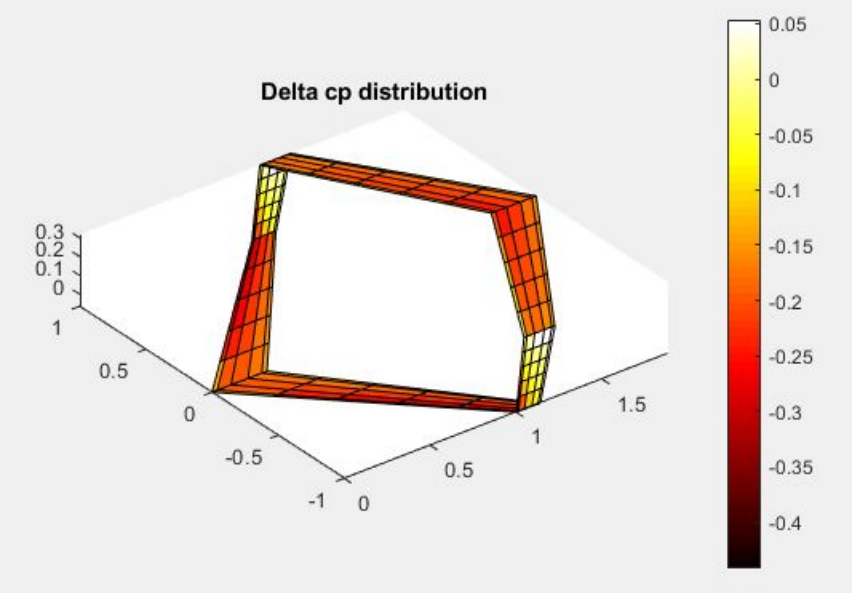

(b) BW-I-M.

Figure 4.12: Distribution of pressure along the wing geometry.

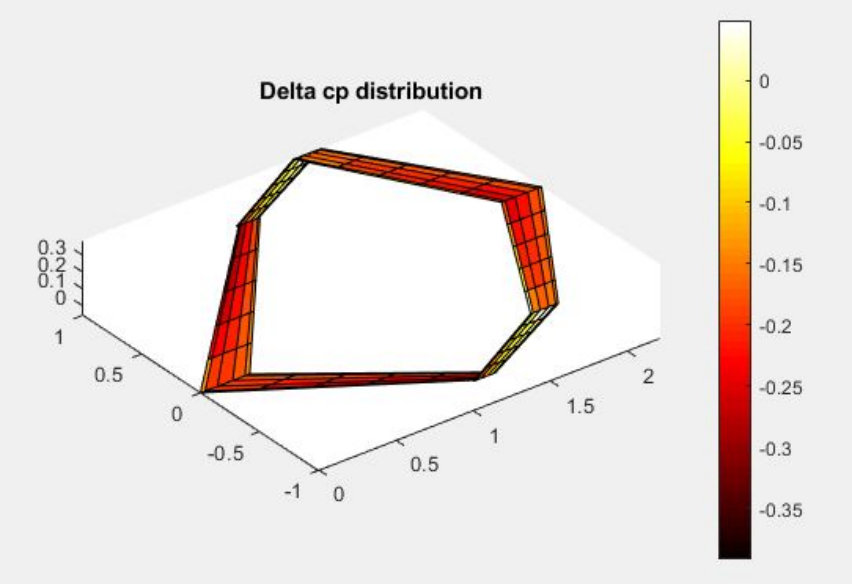

(a) BW-II-A.

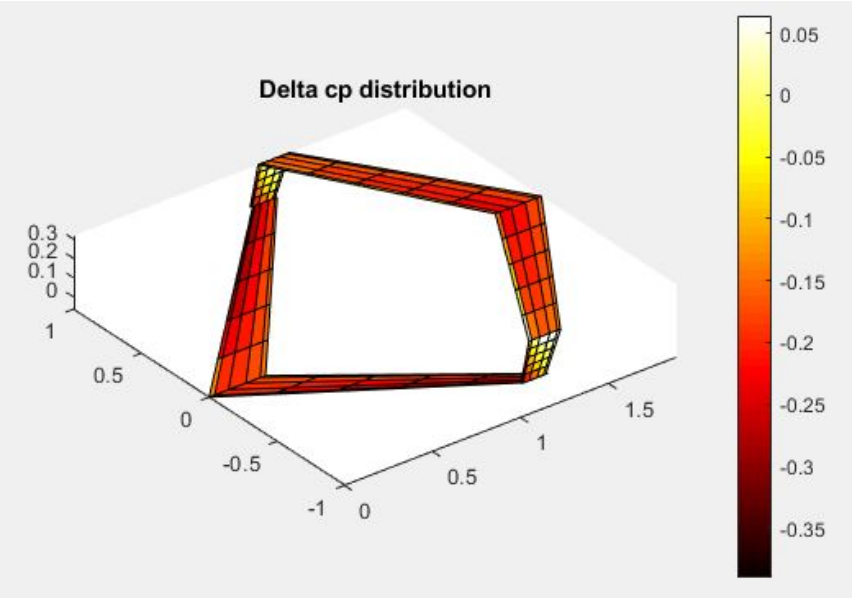

(b) BW-II-M.

Figure 4.13: Distribution of pressure along the wing geometry.

The distribution of a conventional tapered wing is dependent of the taper ratio, producing the greatest amount of lift at approximately 60 to 70 % of the wingspan (measured from the wing root). Therefore, closer to the wing tips, the amount of lift generated is diminished, due to wingtip vortices. Nonetheless, these vortices are significantly reduced in box-wing aircraft. Though, Tornado provides an estimated representation of the difference in pressure distribution for each of the wings: the lower fore wing shows an increasing pressure coefficient distribution in the spanwise direction due to the higher suction towards the tips experienced by swept-back wings (that is the main reason why they are susceptible to tip stall); opposite to what the swept-forward wings undergo.

Moreover, the lack of variation in the pressure distribution over a symmetric airfoil with no angle of attack involves that there is no lift force generated due to the symmetry. That is the reason why vertical fins show such distribution. Nevertheless, due to the lack of

accuracy that the software shows when implementing the attachment between the wings, it may seem that the vertical fins do have some pressure difference on their surfaces.

4.2.5 Conclusions

Despite the fact that Tornado is not able to accurately perform an analysis on viscous forces, such as the drag force, the total lift and pitching moment coefficients estimations are useful so as to define which kind of geometry is more suitable, in terms of aerodynamics. In terms of lift, the higher the aft wing is placed, the better for the lift coefficient. This may be due to the lower interference from the front wing.

Moreover, regarding the aircraft's overall longitudinal static stability, values differ if the reference point is not placed properly, so less accurate results may be found for coefficients which involve any moment on the aircraft.

However, considering the similarities between the basics established in theoretical researches and the data found, the geometry that shows the most potential benefits is configuration BW-I-A, with no dihedral and larger relative separation between the wings (both vertical and longitudinal).

4.3 Numerical approach: 2-D CFD simulation

So far, the BW-I-A box-wing geometry has been set as potentially beneficial for the aerodynamic performance. Nevertheless, as mentioned in subsection 4.1.4, configurations BW-I-M, BW-II-A and BW-II-M (the two latest with positive dihedral angle set at the forward wing) are still evaluated for further comparison. To improve the preliminary aerodynamic design of each one, it is recommendable to perform a Computational Fluid Dynamics (CFD) simulation.

Computational Fluid Dynamics is a computer-based fluid dynamics simulation through the finite volume method for evaluating the behavior of the fluid flow (or any other physical process) on the region of interest of a particular geometry. In that way, quantitative predictions of the phenomena involved are produced, based on the integral, conservative form of the conservation equations of mass, momentum and energy that govern the fluid motion.

4.3.1 Settings

Despite the fact that 3-D simulations usually give better results than 2-D simulations, they are computationally more expensive. Therefore, due to limitations in computing power, only 2-D simulations are performed in the present project. Nevertheless, they can be successfully used for parametric study, so as to illustrate the main parameters of the research: the lift and drag coefficients, and the pressure and velocity field distributions.

Three separate sections of each wing layout are created (at the 30 %, 60 % and 90 % of the wingspan from the longitudinal axis of the configurations), as depicted in Figures 4.14, 4.15 and 4.16 for the BW-I-A. These positions are chosen intentionally, so that approximated conclusions regarding the variation of aerodynamics can be deduced.

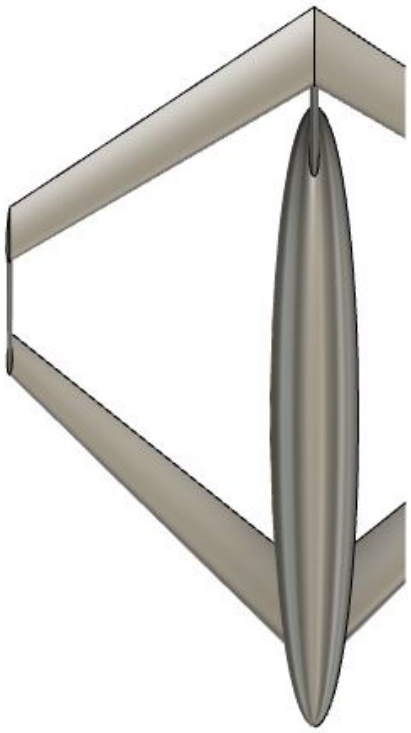

(a) Top view.

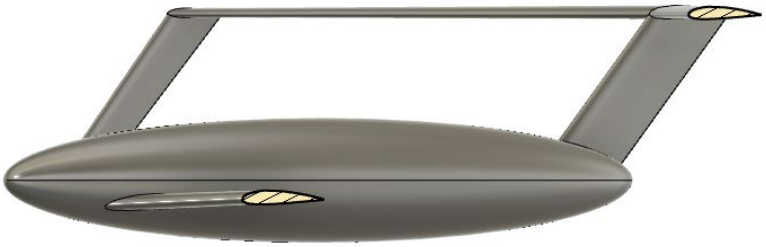

(b) Side view.

Figure 4.14: Section at the 30 % of the span.

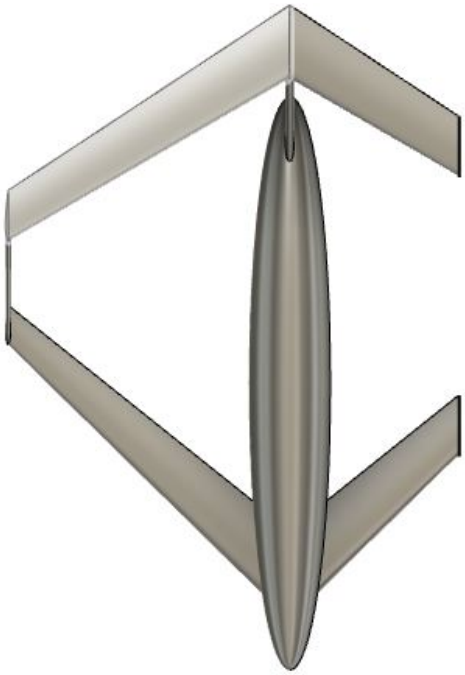

(a) Top view.

(b) Side view.

Figure 4.15: Section at the 60 % of the span.

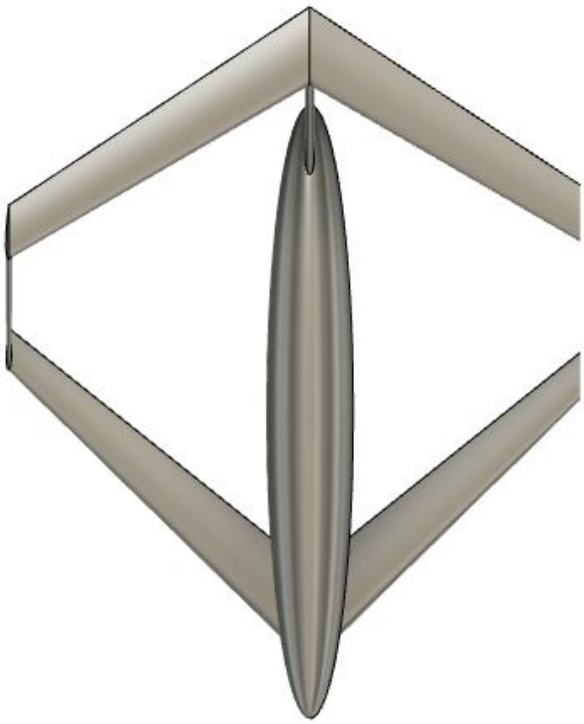

(a) Top view.

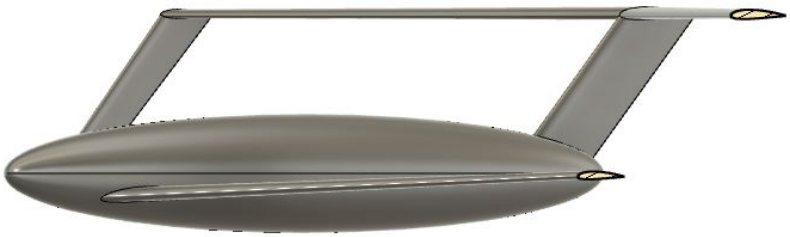

(b) Side view.

Figure 4.16: Section at the 90 % of the span.

- **Conditions of the flow**

The flight conditions introduced in section 3.3 lead to the atmospheric data included in Table 4.6.

Temperature [K]	284.90
Pressure [Pa]	95,460.83
Density [kg/m^3]	1.16727
Dynamic viscosity [kg/m·s]	$1.7737 \cdot 10^{-5}$
Speed of sound [m/s]	338.369
Mach number [-]	0.089

Table 4.6: Atmospheric data for the flight conditions.

- **Domain and geometry**

To set the numerical domain, the boundary conditions should be far enough from the region of interest. For external flow, it is accepted to establish 5 chords above and below,

5 chords upstream, and between 5 to 20 chords downstream (in this case, it has been set to 15), being the reference chord that of the fore wing. Besides, the external surface of the domain is constituted by two different shapes: a rounded inlet and flat top, bottom and outlet sections.

The resulting domain is shown in Figures 4.17 and 4.18.

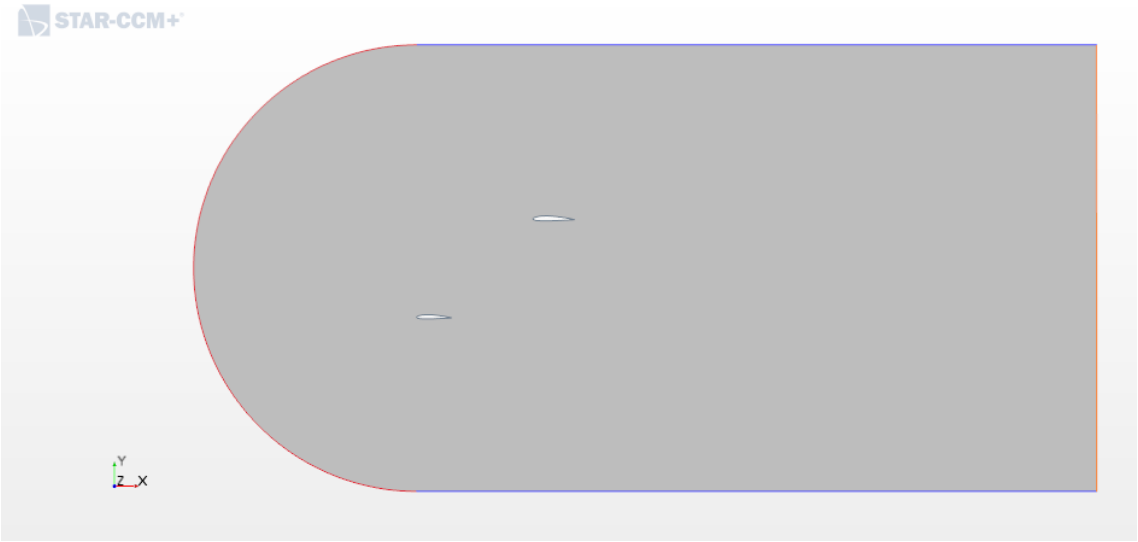

Figure 4.17: Geometry of the numerical domain.

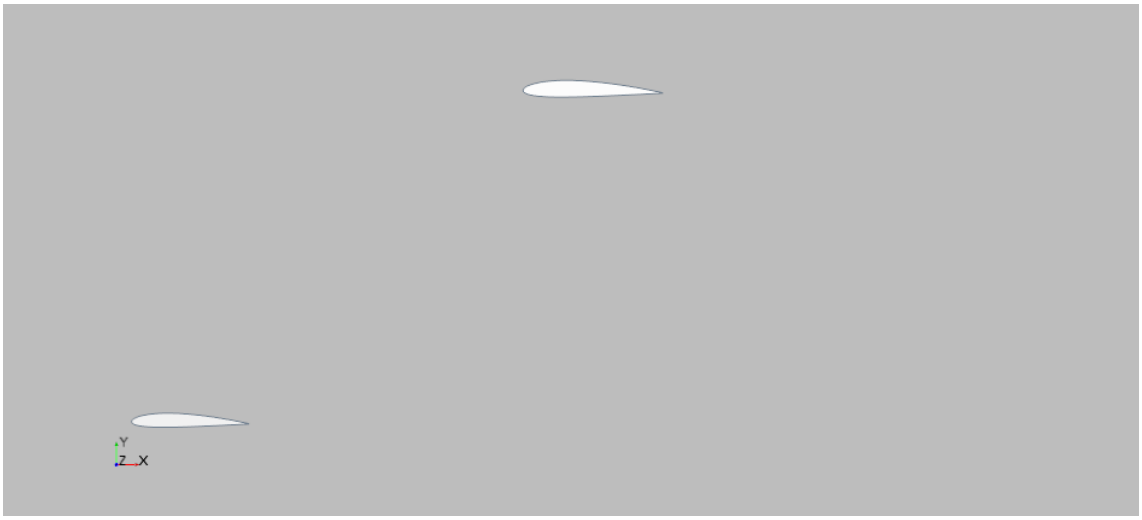

Figure 4.18: Geometry of the numerical domain (close-up).

- **Mesh generation**

Through the mesh generation, geometries are divided into discrete, topological structures, called cells.

For the cases under study, an unstructured mesh is used. This type of mesh has become very popular, due to its fast grid generation, ability to manage complex geometries and the fact that no significant previous experience is required at all.

Regions near both airfoils are of the most interest, so they must be accurately meshed

and refined, thus ensuring that no abrupt changes in the dimensions of adjacent cells that could lead to miscalculations are produced. Thicker cells may be sufficient for the rest of the regions, but still carefully adapting their dimensions to the above-mentioned more defined cells.

Mesh refinement involves increasing the number of cells and reducing the smallest dimension to increase accuracy, but at the expense of higher computational cost. There exist different ways to refine a mesh. In particular, the one used in the following simulations is wake refinement, which allows to evaluate with more precision the area downstream of the airfoils. It is set up to 5 chords.

The more accurate the mesh generated and the boundary conditions imposed are, the more accurate the numerical solution to the problem is. That is the main reason why a mesh refinement in the closest region to the airfoils is performed due to the wake downstream.

Moreover, turbulence models enable to resolve the viscous sublayer in the near-wall region. For that, the first grid cell should be about $y^+ = 1$, and the growth rate of the prism layer must not be higher than 1.2. Hence, the overall number of cells is significantly increased.

For steady-state simulations, to consider that a solution is valid, it must satisfy a series of conditions:

- The residuals (r.m.s. error), which reveal the difference between the actual and predicted values, should take acceptable values (typically 10^{-4} or 10^{-5}).
- The values of the parameters of interest, which are essentially the main outputs of the simulation, must reach a steady solution.
- Imbalances in the domain should be less than a 1 %.

There are also meshing requirements to be implemented in order to achieve valid results that are independent of the mesh resolution. The mesh independence study is an essential procedure to ensure that results do not depend on the mesh. The global mesh sizing is decreased (the relevant parameters are generally divided by 1.5) until the variation of the reference value is negligible (within an allowable tolerance). The smallest mesh that is accurate enough to calculate an acceptable result (i.e. ensures a mesh independent solution) should always be chosen in order to reduce the simulation run time.

In this case, the relevant parameters are set to be the base size of the default element, as well as the prism layer's features, so as to ensure an acceptable approach to the viscous layer. The error tolerance is fixed at approximately a 1 % of variation.

Therefore, mesh sensitivity studies are crucial in numerical simulations for determining the most efficient number of cells to provide satisfactory results. The best way to present a mesh independent solution is by means of a graph, like those in Figure 4.19. The outputs employed to verify the mesh independence are the lift and drag coefficients (the following figures related to the characteristics of the computational analysis are related to the configuration BW-I-A; still, a similar procedure is performed with the other geometries under study).

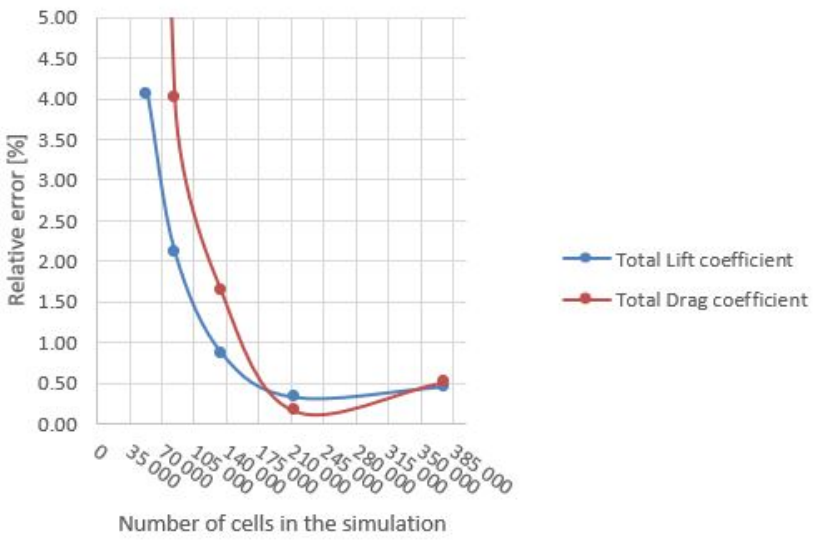

Figure 4.19: Study of the mesh independence.

All factors considered, the most relevant settings of the mesh generated are shown in Table 4.7, and a general representation is displayed in Figures 4.20 and 4.21.

Base Size [m]	0.005
Surface Growth Rate [-]	1.05
Number of Prism Layers [-]	12
Prism Layer Stretching [-]	1.3
Prism Layer Total Thickness [m]	0.00247

Table 4.7: Relevant parameters of the generated mesh.

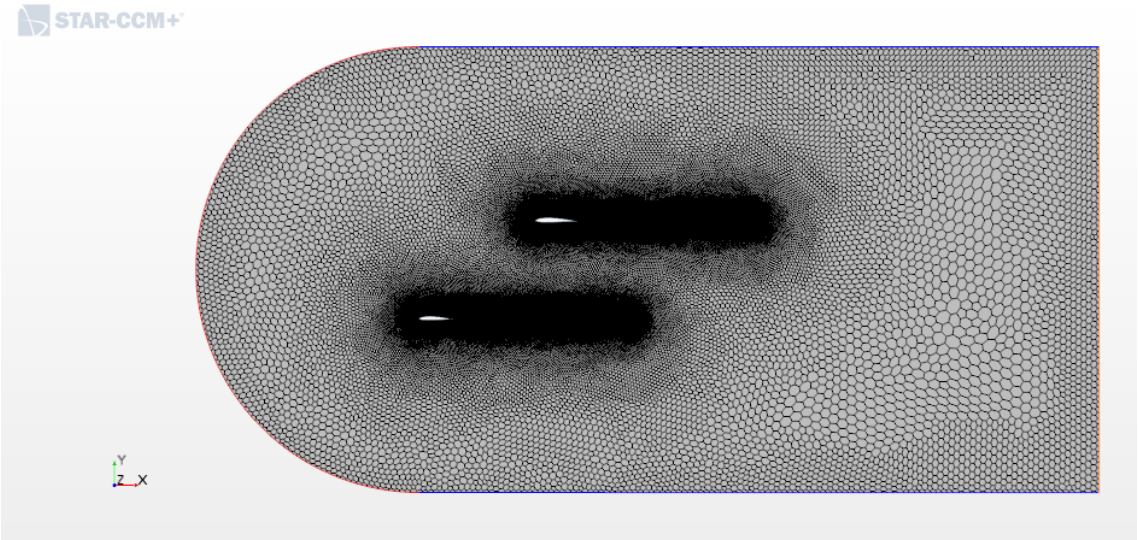

Figure 4.20: Geometry of the generated mesh.

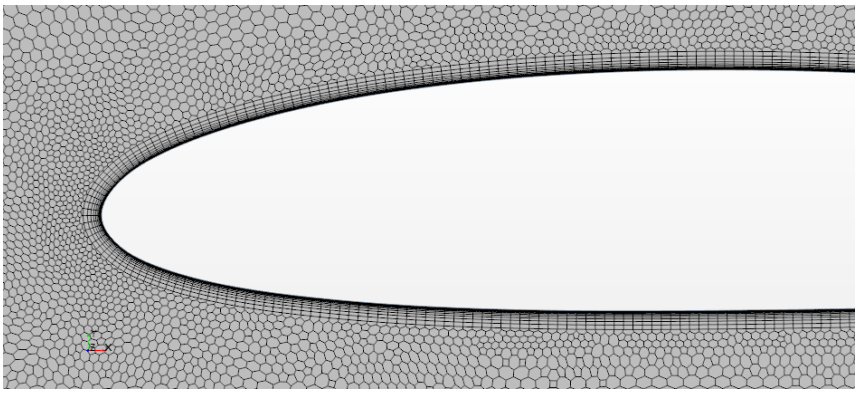

Figure 4.21: Geometry of the generated mesh (close-up).

- **Models and fluid properties**

The air flow moving across the geometries under study is considered to be incompressible, due to the low speeds at which it travels (incompressible flow can be assumed for Mach numbers lower than approximately 0.3). Hence, several air properties, such as temperature, viscosity and density are kept constant during the whole process.

Therefore, a pressure-based solver (also known as segregated solver in STAR-CCM+ ®) is used for the simulations. The principal aspects of the indicated solver are the following:

– All transport equations are solved in a sequential, uncoupled manner.

– Density is calculated from the equation of state, whereas pressure is solved by combining the momentum and continuity equations.

– Simpler, faster and demands lower memory requirements and fewer iterations to achieve convergence than a density-based (coupled) solver.

– Requires acceptable initial conditions, setting a constant temperature to the flow conditions and a constant velocity in the direction of the flow.

The most widely used turbulent model for external aerodynamics in industry is the Reynolds Averaged Navier-Stokes (RANS). It is a robust model ideal for steady-state simulations that obtains the average of all turbulent scales of the flow.

Many different models are available, among which the following stand out in modern engineering applications: Spalart-Allmaras and k–omega.

Spalart-Allmaras is an economical RANS model for large meshes, designed specifically for aerospace and turbomachinery applications. It gives good results for both external and internal flows exposed to moderate adverse pressure gradients (e.g. airfoils), by solving a single transport equation for a modified eddy viscosity. Nevertheless, the most distinctive limitations are its deficient performance in 3-D flows and flows with strong separation and recirculation, so its applicability to all complex engineering flows is restricted.

On the other hand, the k–omega (k-ω) turbulence model is a two-equation turbulence model suitable for a wide range of complex boundary layer flows under adverse pressure gradient, separation and transition, and also for low Reynolds number flows. It shows a much better performance than other models, but it additionally involves an increase in the computational cost per iteration.

In general, turbulence models enable to resolve the viscosity-affected near-wall region, including the viscous sublayer (laminar sublayer), that is, the region that is near a no-slip boundary and in which the flow is laminar. For a modified low Reynolds turbulence model, like the k-ω, to adequately resolve gradients in the sublayer domain, the first grid cells preferably need to be about $y^+ = 1$, so eventually the number of mesh cells significantly increases, and the computational resources required become more demanding. Hence, the choice of a proper turbulence model is relevant to satisfactorily resolve the boundary layer, and to determine the drag and lift forces correctly.

In the end, the low Reynolds k-ω turbulence model is the recommended approach to perform all the analysis, since it is also better for evaluating the forces on the walls (aerodynamic analysis).

- **Boundary conditions**

To define a unique solution and represent a certain operating point for a problem, the information with regard to the flow variables must be specified at the boundaries of the domain. In other words, each domain boundary requires a corresponding boundary condition (BC), defined by the location, type, and magnitude and direction.

A concise summary of all regions and their corresponding boundary conditions is presented in Table 4.8.

Regions	Boundary conditions
Aft and fore airfoils	Wall
Inlet	Velocity inlet
Outlet	Pressure outlet
Top	Symmetry plane
Bottom	Symmetry plane

Table 4.8: Boundary conditions for the CFD simulations.

In order to select the most suitable boundary conditions for the geometry, the fact that the research simulates atmospheric flights and wind tunnel configurations is a key factor:

– For the rounded inlet, a velocity inlet condition (that of the undisturbed flow) is typically appropriate as upstream boundary for incompressible flows (it becomes mass flow inlet for compressible flow). Velocity direction, temperature and the turbulent variables are imposed from the data regarding the flight conditions, but pressure is extrapolated.

– In the case of the outflow flat plane, a pressure outlet is recommended. Only the static pressure is imposed, so the all the other relevant variables are extrapolated.

– The airfoils are replaced by a wall, non-slip (viscous flow) condition. Moreover, since the bodies are non-porous, the velocity component normal to the surface is zero.

– The side walls (i.e. top and bottom for the 2-D simulation) are typically set to symmetry for wind tunnel analysis.

4.3.2 Total lift coefficient

The computational analysis performed is a 2-D evaluation of the relative position of each of the airfoils at the three different sections shown in subsection 4.3.1.

Without considering any three-dimensional wingtip vortices effects over the wing (since they can not be modelled with the present 2-D CFD analysis), a general overview of how the lift coefficient is affected by the relative position of the airfoils is seen in Figure 4.22.

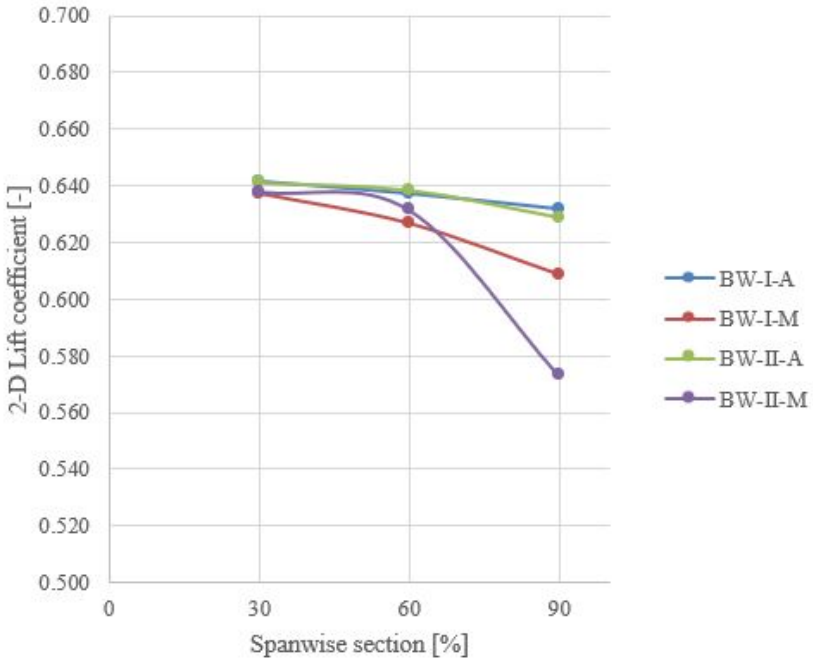

Figure 4.22: 2-D lift coefficient variation along the cross-sectional divisions of the span.

It can be observed that the general tendency of the lift coefficient is to decrease, the closer both airfoils are placed. The main reason for this to happen is more thoroughly explained in subsection 4.3.5. Moreover, airfoils get closer the higher the dihedral angle is, so detrimental effect on the lift coefficient appears, which is more pronounced for the BW-I-M and BW-II-M configurations, due to their proximity; whereas it is almost negligible for the BW-I-A and BW-II-A configurations, since they are far enough from each other so as not to become so relevant.

To estimate the overall three-dimensional lift coefficient (i.e. the one corresponding to the whole lifting system), Equation 4.20 arises. It is widely known that lift generation depends on the cross-sectional shape of the wings. Hence, since different local distributions are obtained at various locations along the span of those wings, a rough approximation is implemented to obtain the value for the total lift coefficient through the mean value of all spanwise cross-sections evaluated, considering the effects of the sweep and dihedral angles.

$$
\begin{aligned}
C_L = & \int_{-\frac{b}{2}}^{\frac{b}{2}} c_l\left(z\right)_{fore} \cdot \cos^2\left(\Lambda_{fore}\right) \cdot \cos^2\left(\Gamma_{fore}\right) \cdot dz + \\
& + \int_{-\frac{b}{2}}^{\frac{b}{2}} c_l\left(z\right)_{aft} \cdot \cos^2\left(\Lambda_{aft}\right) \cdot \cos^2\left(\Gamma_{aft}\right) \cdot dz \approx \\
& \approx \frac{\sum_{i=1}^{N} c_{l\,fore}}{N} \cdot \cos^2\left(\Lambda_{fore}\right) \cdot \cos^2\left(\Gamma_{fore}\right) + \\
& + \frac{\sum_{i=1}^{N} c_{l\,aft}}{N} \cdot \cos^2\left(\Lambda_{aft}\right) \cdot \cos^2\left(\Gamma_{aft}\right)
\end{aligned}
\tag{4.20}
$$

Figure 4.23 displays the estimated lift coefficient of the whole wing for each configuration, which follows the same tendency as for the 2-D case. Moreover, a comparison regarding the three different methodologies used throughout the document (those studied in sections 4.1 and 4.2) is established in Table 4.9.

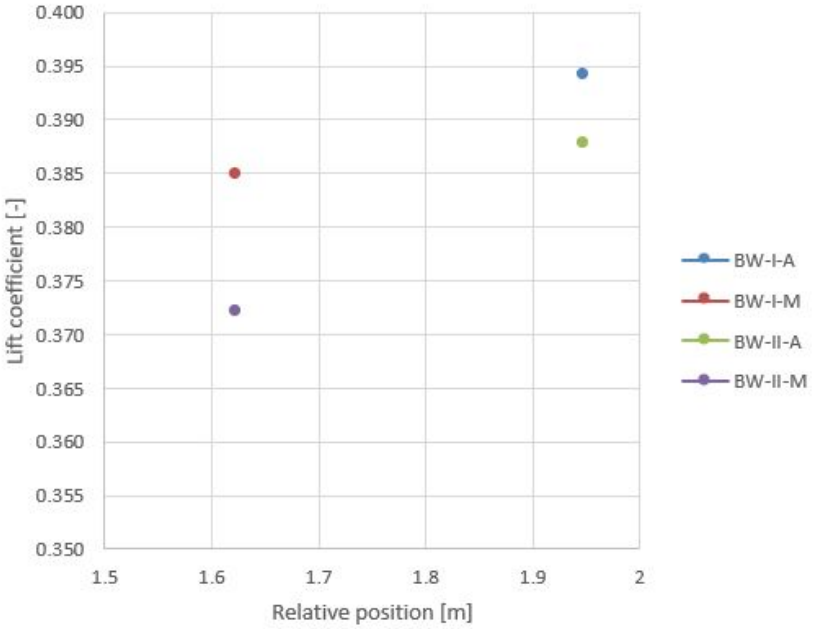

Figure 4.23: Total lift coefficient for the different geometries under study.

	MatLab ®	**Tornado**	**STAR-CCM+ ®**
BW-I-A	-	0.391	0.394
BW-I-M	0.417	0.390	0.385
BW-II-A	-	0.376	0.388
BW-II-M	0.417	0.373	0.372

Table 4.9: Comparison of the total lift coefficient of the different methodologies implemented throughout the project.

From Table 4.9, and recalling subsection 4.2.1, Tornado may give acceptable values for the lift coefficient despite the fact that relevant effects, such as the thickness of the lifting surfaces, are coarsely approximated. Even so, software like STAR-CCM+ ® are meant to provide more reliable data, since calculations of the force coefficient are implemented by

normalising the force that is extracted from the pressure and shear stresses on each cell's surface of the body under study.

4.3.3 Total drag coefficient

Typically, when dealing with airfoils inmersed in 2-D subsonic incompressible flows, drag is the addition of the viscous and the pressure drag components. The former comes from the friction between the fluid and the surfaces of the object over which it flows, which is associated to the formation of boundary layers, and it scales with the Reynolds number; whereas the latter, arises due to the shape of the body, and depends on the flow separation point.

The variation of the drag coefficient is affected by the relative position of the airfoils, as seen in Figure 4.24.

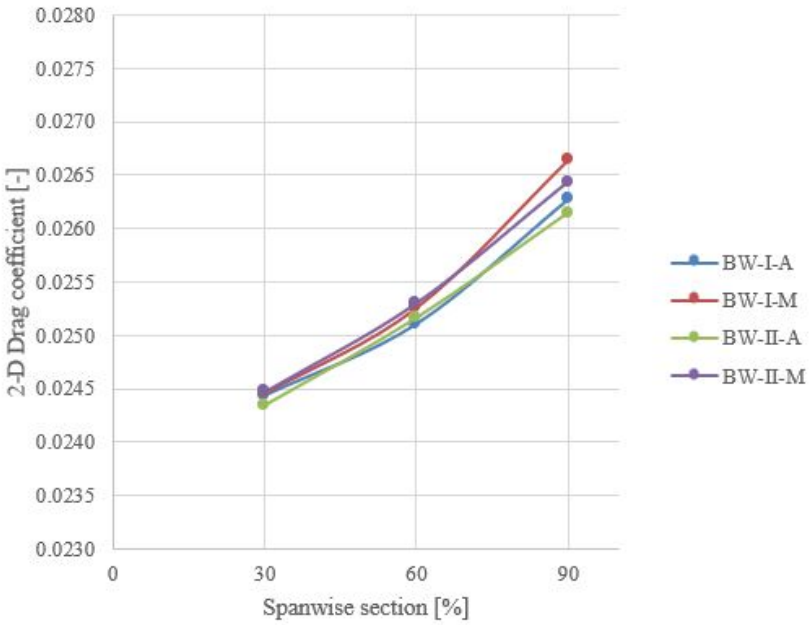

Figure 4.24: 2-D drag coefficient variation along the cross-sectional divisions of the span.

The way to obtain the drag coefficient for the whole wing system (Figure 4.25) is analogous to the procedure followed in subsection 4.3.2 for estimating the overall three-dimensional lift coefficient.

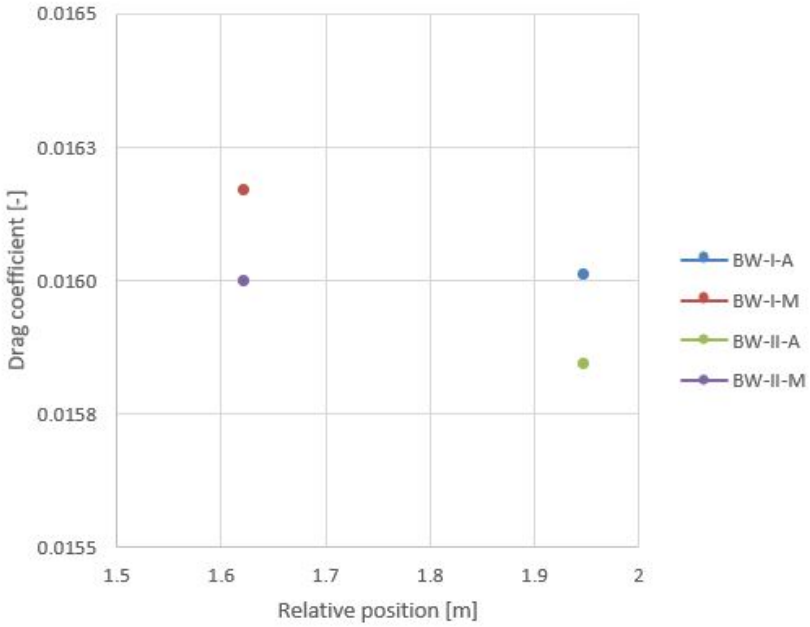

Figure 4.25: Total drag coefficient for the different geometries under study.

As already done for the lift coefficient, a comparison regarding the three different methodologies used throughout the document is established in Table 4.10. In this case, the reduction of the relative height between airfoils due to the increase in the dihedral angle induces an apparent reduction in drag. Nevertheless, the magnitude is not significant and may even be caused by the accuracy of the simulations. Hence, further study related to 3-D simulations is required to better analyse the dihedral effect on the whole wing structure.

	MatLab ®	**Tornado**	**STAR-CCM+ ®**
BW-I-A	-	-	0.0160
BW-I-M	0.0222	-	0.0162
BW-II-A	-	-	0.0158
BW-II-M	0.0225	-	0.0160

Table 4.10: Comparison of the total drag coefficient of the different methodologies implemented throughout the project.

Initially, aft airfoils produce greater amounts of drag, since deviation of the flow caused by the forward wing, causes an increase in the effective angle of attack in the rearward wing, thus increasing the drag.

However, the fact that the drag coefficient increases as the relative longitudinal position is reduced occurs mainly because there exists higher interaction among the air flow circulating in between both airfoils, which, indeed, is prejudicial for the performance of the forward wing. Moreover, such an interaction induces higher velocities in the flow surrounding the aft airfoil, producing less drag as a consequence of a smaller, more stable boundary layer. Consequently, the presence of a lower front wing implies a reduction in drag on the rear one. Refer to subsection 4.3.4 for a more evident visualisation of the phenomena.

MatLab ® provides more accurate results than those calculated by means of STAR-CCM+ ®, due to the fact that the 3-D aerodynamic effects of trailing vortices are not considered in the CFD simulation, and no vertical fins are modelled either.

4.3.4 Velocity field distribution

Not to overload the current subsection with all the different cases under study, only the two most extreme configurations regarding longitudinal and vertical separations (that is, the smallest and largest relative positions) are considered, so as not to compromise the main purpose of the study. That is, configurations BW-I-A (maximum) and BW-II-M (minimum) are considered at both, the 30 % (Figures 4.26 (a) and 4.27 (a), respectively) and 90 % (Figures 4.26 (b) and 4.27 (b), respectively) cross-sections from the root.

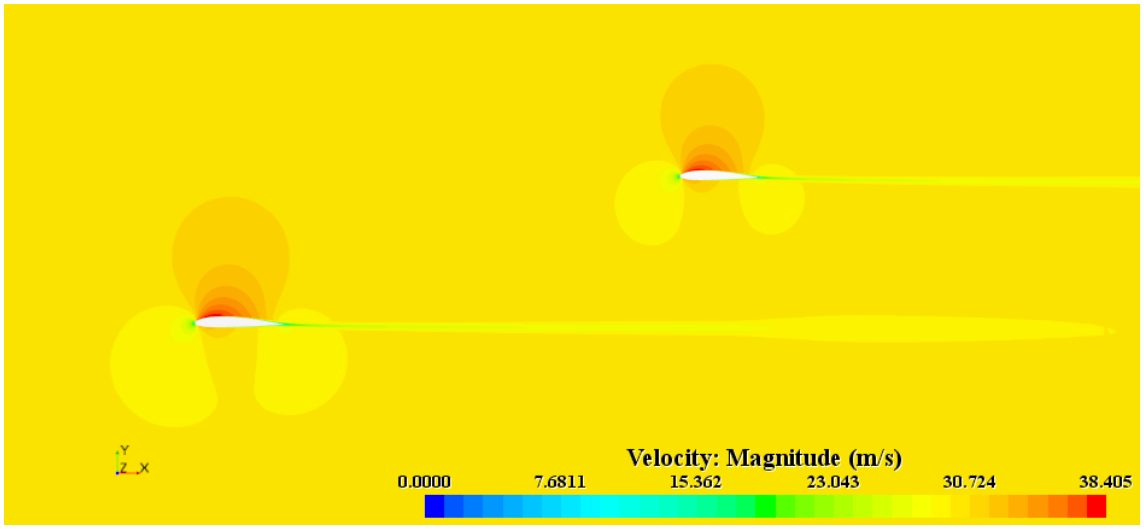

(a) 30 % spanwise cross-section.

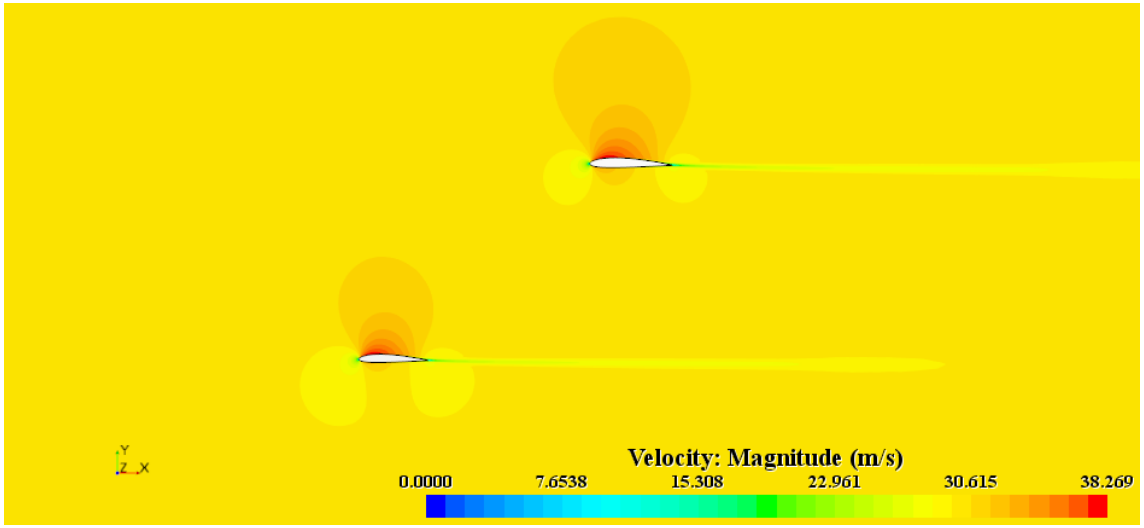

(b) 90 % spanwise cross-section.

Figure 4.26: Velocity field distribution: BW-I-A configuration.

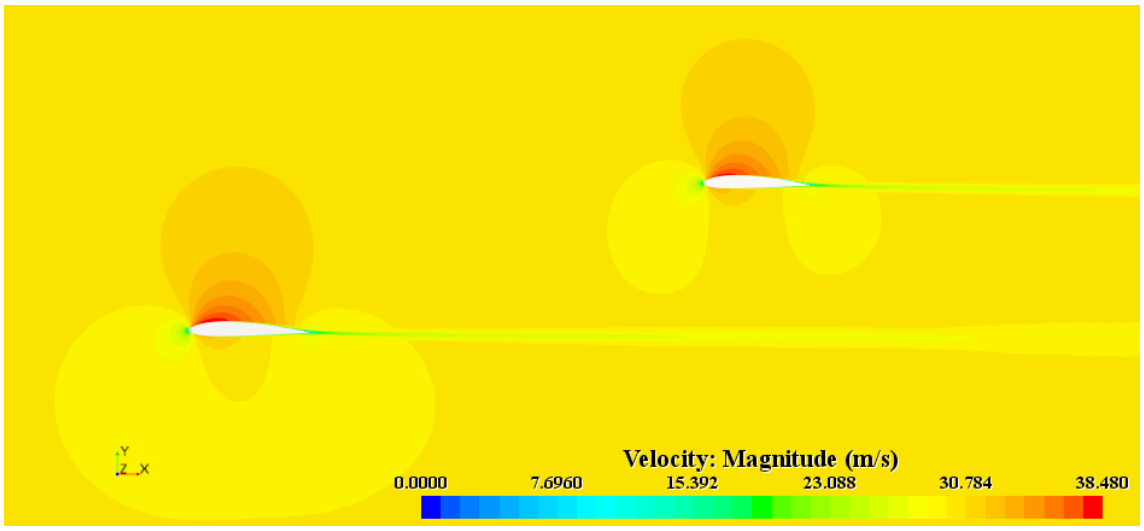

(a) 30 % spanwise cross-section.

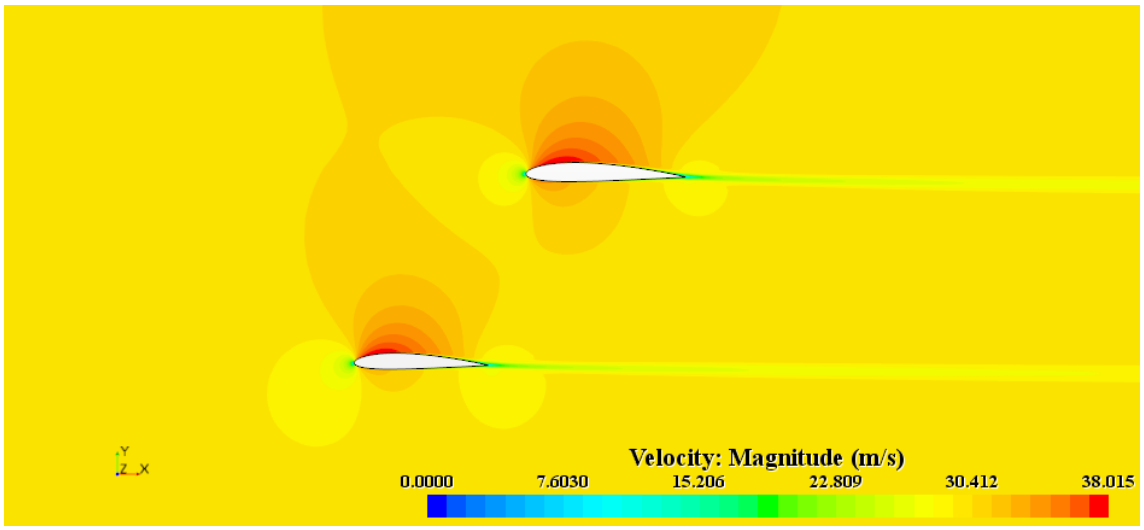

(b) 90 % spanwise cross-section.

Figure 4.27: Velocity field distribution: BW-II-M configuration.

Still, an additional hypothetical location of the airfoils at a relative position of half a reference, fore, chord is established for the sake of better understanding (Figure 4.28).

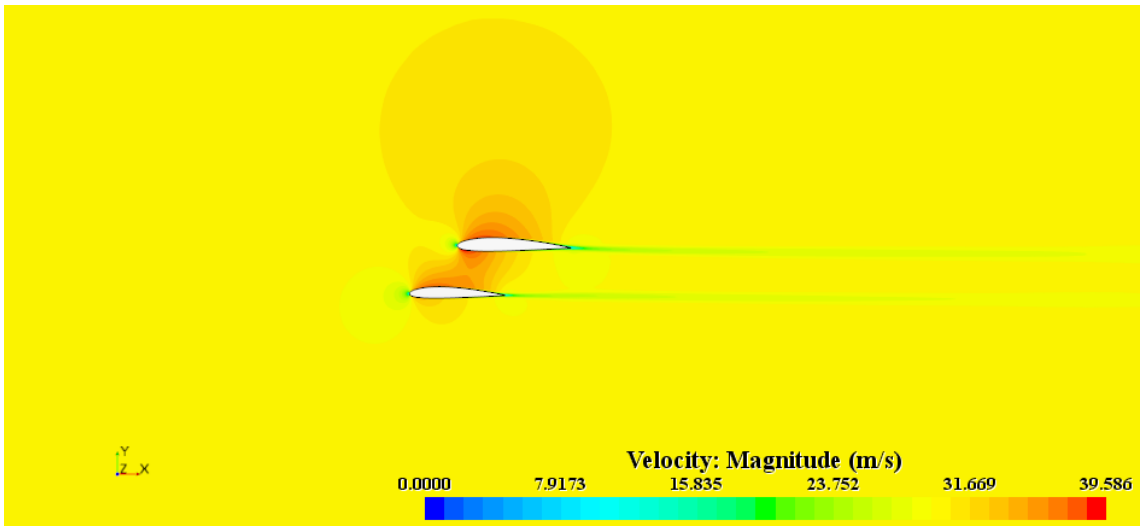

Figure 4.28: Velocity field distribution: additional configuration.

4.3.5 Pressure field distribution

The local lift distribution is obtained through the pressure distribution along the chord of each spanwise location.

Again, configurations BW-I-A (maximum) and BW-II-M (minimum) are considered at both, the 30 % (Figures 4.29 (a) and 4.30 (a), respectively) and 90 % (Figures 4.29 (b) and 4.30 (b), respectively) cross-sections from the root, as well as the additional hypothetical location of the airfoils (Figure 4.31).

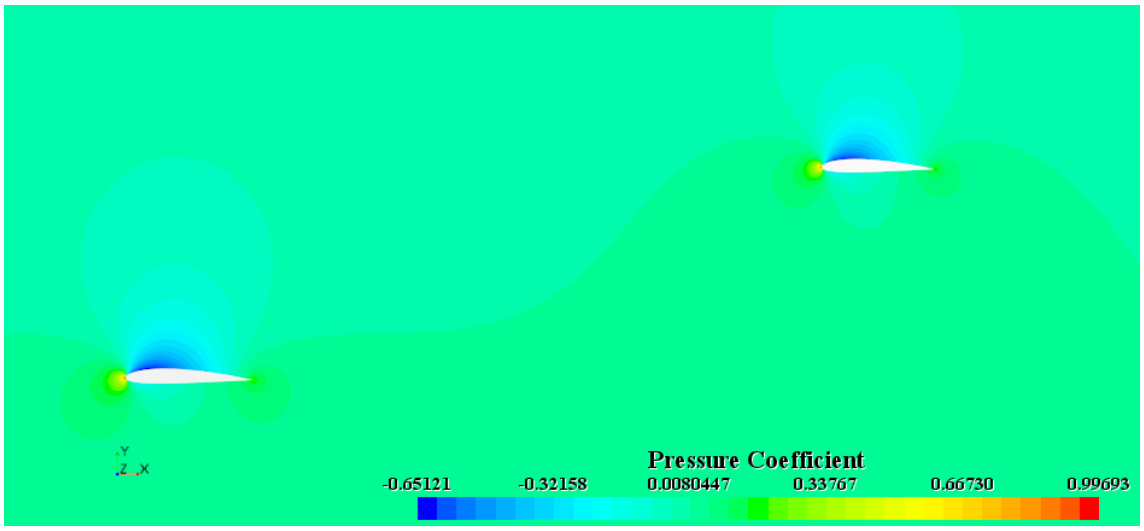

(a) 30 % spanwise cross-section.

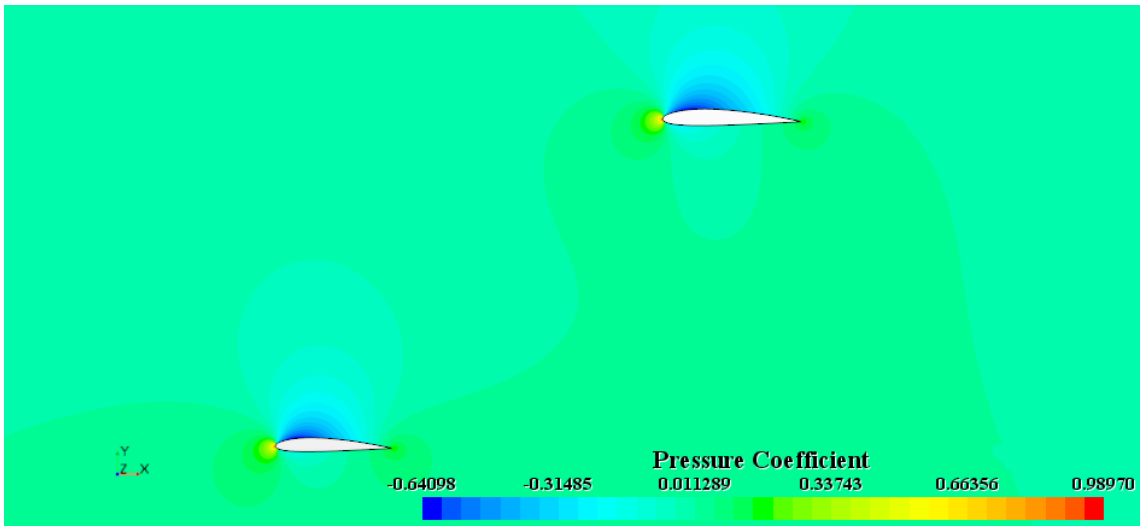

(b) 90 % spanwise cross-section.

Figure 4.29: Pressure coefficient distribution: BW-I-A configuration.

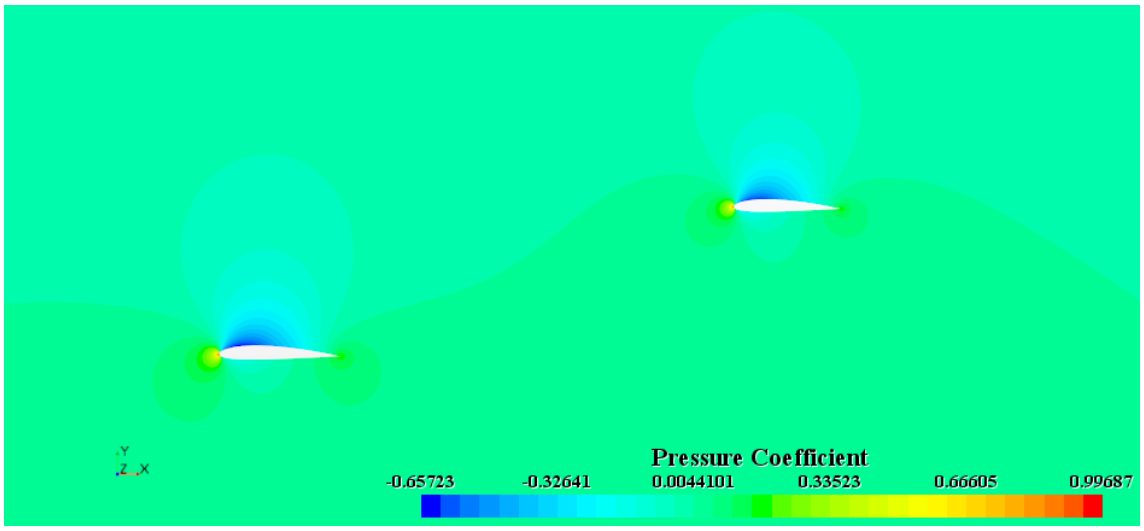

(a) 30 % spanwise cross-section.

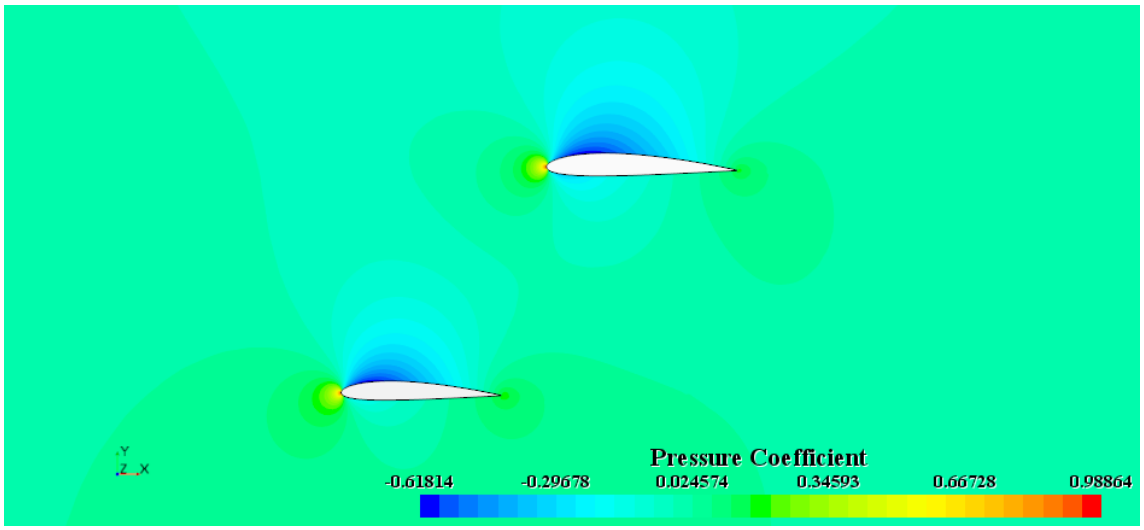

(b) 90 % spanwise cross-section.

Figure 4.30: Pressure coefficient distribution: BW-II-M configuration.

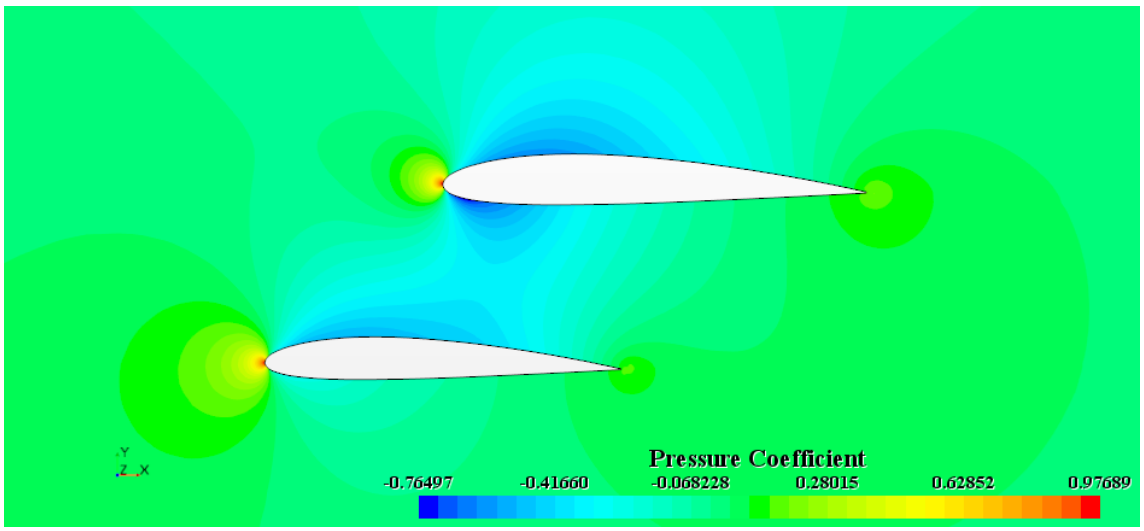

Figure 4.31: Pressure coefficient distribution: additional configuration.

In addition to the figures, it is interesting to further analyse the evolution of the lift coefficient along the span (as previously seen in Figure 4.22) by considering the pressure coefficient distributions (Figures 4.32, 4.33 and 4.34).

A phenomenon that can be observed is that the lift of the fore wing remains practically constant for all situations.

The interaction of the low pressure lobe of the lower airfoil with the *intrados* of the upper one, produces a reduction of the pressure coefficient of the aft airfoil, thus reducing the force generated. In fact, the low pressure zone of the rearward airfoil is smaller than that of the forward airfoil, which also means a reduction in lift.

Due to the limited flight conditions, no more concluding remarks can be extracted. However, it may be foreseen that a higher angle of attack would involve interaction of the wake of the fore wing with the aft one, thus reducing the lift of the latter. This effect is maximised by the proximity of the wings, so a higher separation among them is recommended.

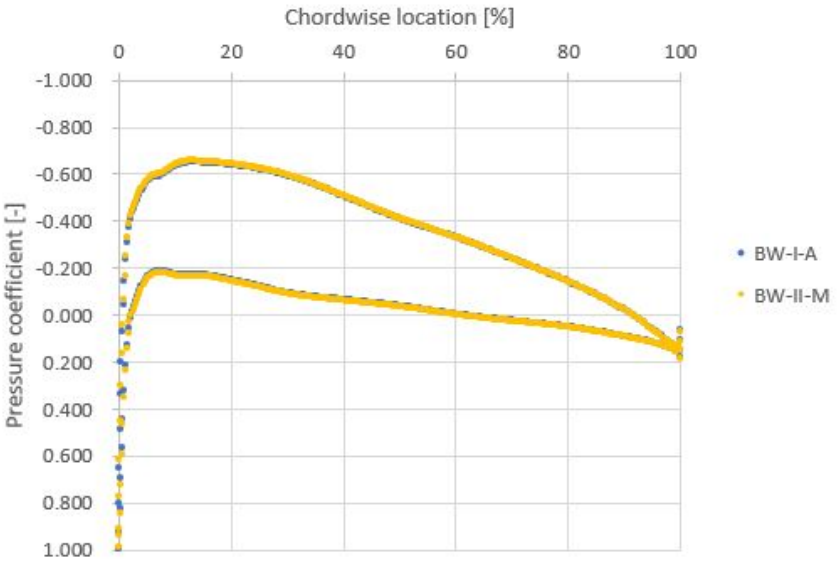

(a) Fore airfoil.

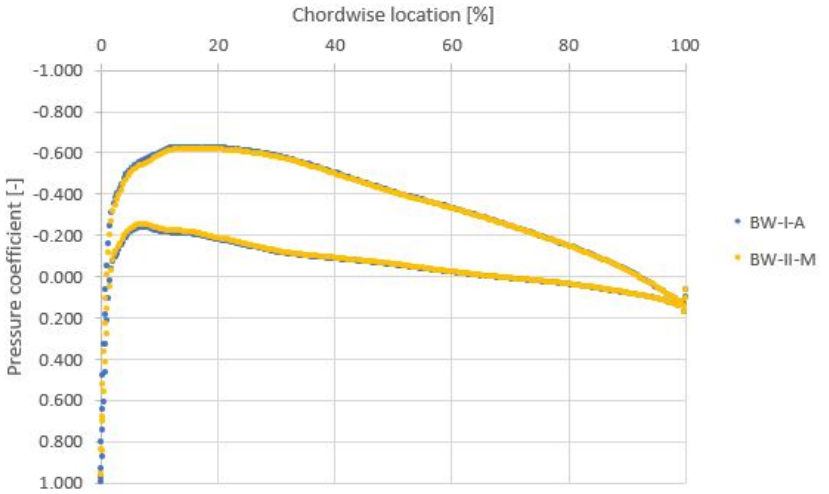

(b) Aft airfoil.

Figure 4.32: Pressure coefficient distribution: 30 % spanwise cross-section.

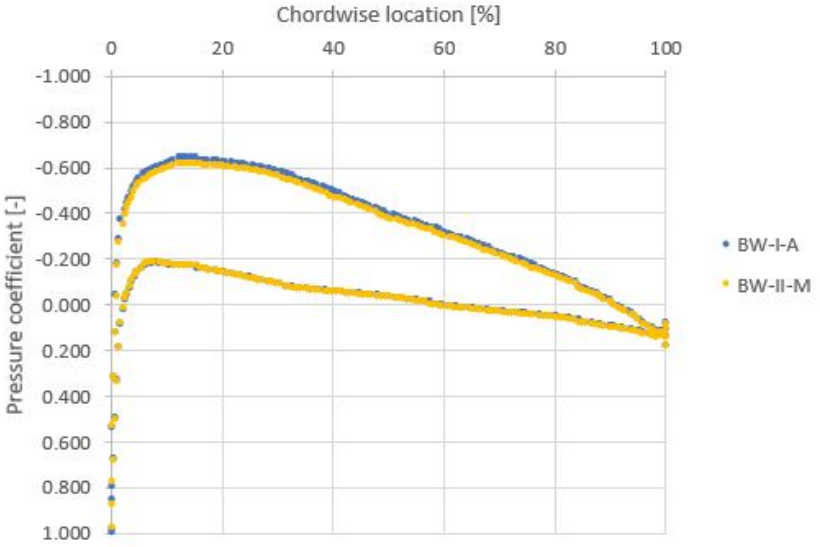

(a) Fore airfoil.

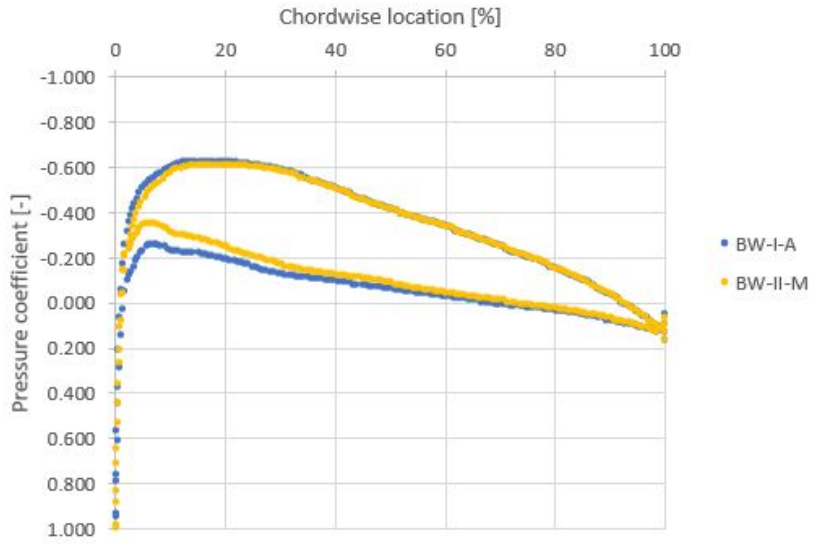

(b) Aft airfoil.

Figure 4.33: Pressure coefficient distribution: 90 % spanwise cross-section.

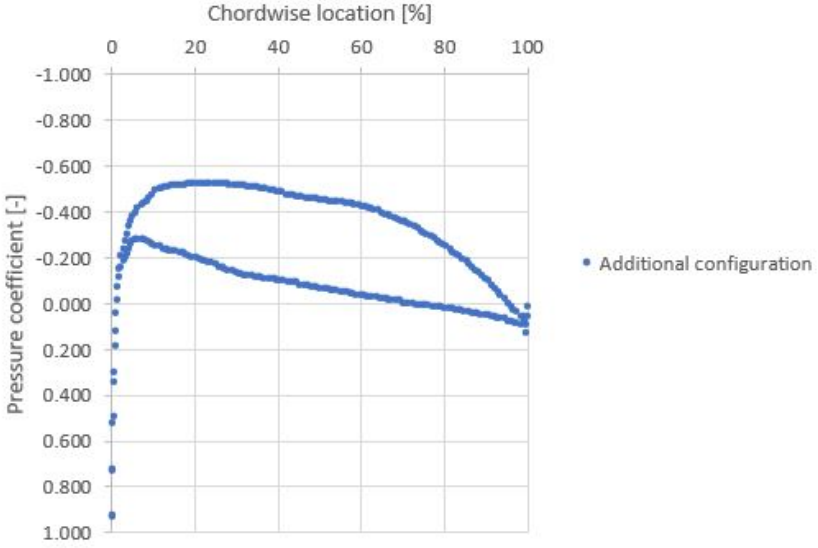

(a) Fore airfoil.

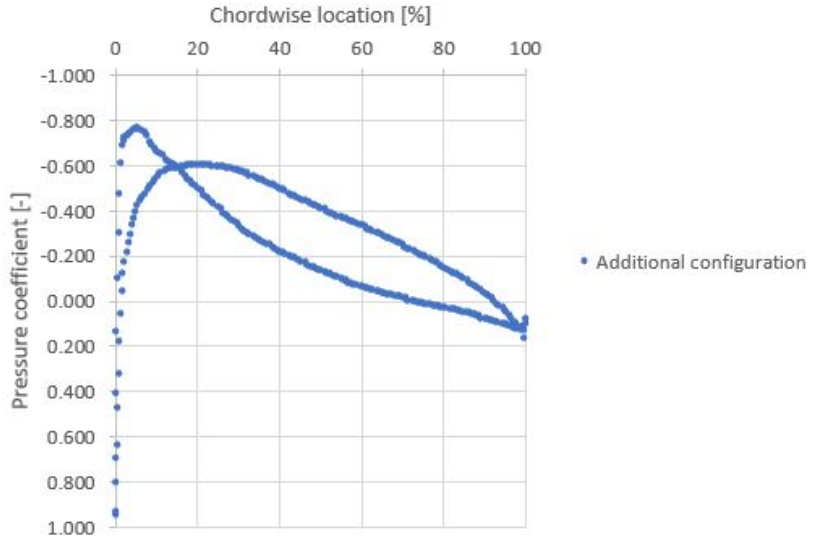

(b) Aft airfoil.

Figure 4.34: Pressure coefficient distribution: additional configuration.

4.3.6 Conclusions

On the whole, a set of significant conclusions can be extracted:

- If the relative position of both profiles is diminished, lift is considerably reduced.
- In addition, if the fore wing is placed underneath, interference effects among the lifting surfaces are also reduced.
- In general, the rear wing induces greater drag due to the deviation of the flow trailing from the front wing, when no other interaction effects are considered.

Therefore, the relative position of the wings must be increased and the forward wing should be placed lower than the rear wing, so as to maximise the lift coefficient without generating too much drag.

Chapter 5

Overall conclusions

In theory, box-wing aircraft are potentially likely to carry more passengers and/or cargo without significant increase in size (within the constraints of actual airports) or fuel consumption, due to the distribution of the lift needed between the two lifting surfaces. Other advantages for such configurations are the improvement in range and endurance, and reduced harmful emissions, as beneficial effects of the reduction in induced drag and the enhancement of aerodynamic efficiency. In addition, it is also suggested that such a configuration is expected to be really stable.

The main basis of the present project is how sweep angles and the relative position between the two wings that arrange the overall wing structure modify the aerodynamic behaviour of the aircraft. In fact, this approach is a drawback itself, due to the extremely large amount of factors to consider. Furthermore, flight conditions are an important parameter that have been fixed for the sake of simplicity. Therefore, depending on the mission, they definitely vary, so it would be convenient to analyse the behaviour at such conditions.

Since the wing configuration notably differs from that of a conventional aircraft, the general theory of aerodynamics and aircraft design is considered to be somewhat outdated, so that is why results have been validated with different analytical and numerical calculation software, in order to provide the most accurate results that can be obtained in a preliminary design phase.

Numerical simulations have been restricted to the 2-D study due to computational limitations. However, set-ups have been implemented sufficiently accurate, so as to avoid any source of misleading calculations.

Regarding the results, significant trends and phenomena have been observed:

- Reducing the sweep angles in both wings involve an adverse effect on the aerodynamic efficiency of the wing configuration. Nevertheless, it is not advisable to increase them excessively, otherwise, both, the parasitic drag induced by the vertical tip fins and the drag due to lift generation itself, would overcome the higher lifting capabilities of the structure. Hence, a trade-off must be established.

- Despite the fact that the overall vertical tip fins surfaces are reduced by the addition of dihedral and anhedral angles, these do not offer improved aerodynamic efficiency due to higher induced drag as wings get closer.

- Disadvantageous interference effects generated between the two wings are attenuated if the forward wing is placed underneath.

- The rearward wing is subjected to the deviated trailing flow from the presence of the forward wing, which involves inferior local aerodynamic performance if compared to the fore wing.

- The further away (both, longitudinally and vertically) the wings are placed from each other, the lower the interactions become, so the wing structure achieves a higher performance. Moreover, the configuration is also supposed to be more stable.

As a conclusion, it can be said that there are numerous benefits for its use in specific applications into the general aviation (GA) category. Nonetheless, more research is required to fully comprehend the aerodynamic behaviour and other practical aspects of these designs. For instance, the development of a scale wind tunnel model would be advantageous to estimate real in-flight performance and validate data achieved from software simulations.

Chapter 6

Final box-wing layout

In accordance with the most relevant conclusions of the project regarding the main parameters under study and their direct effect on aerodynamics, as well as considering the flight conditions under which the configuration is analysed, the most potentially beneficial box-wing configuration is introduced in Figure 6.1, which corresponds to the BW-I-A layout. A 3-view detail drawing is also included in Figure 6.2.

To ease the understanding of how the wing structure attaches to the whole aircraft, the fuselage and vertical stabiliser are modelled.

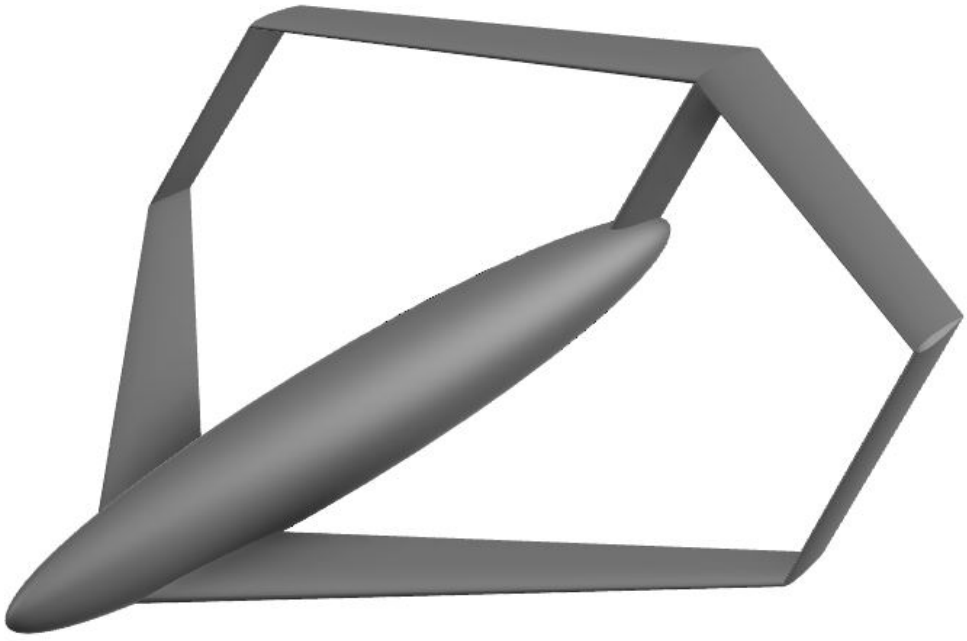

Figure 6.1: 3-D rendering of the BW-I-A box-wing configuration.

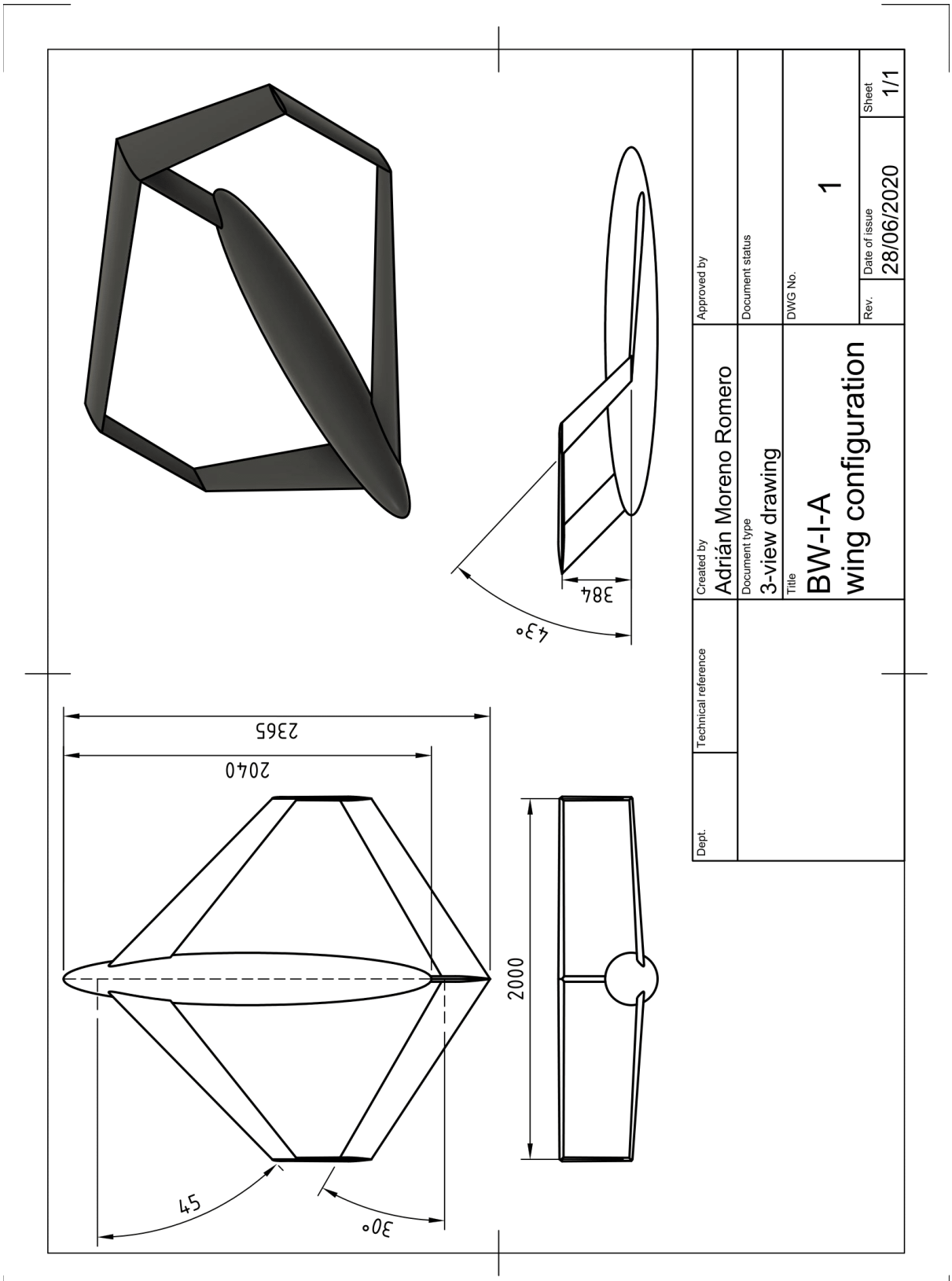

Figure 6.2: 3-D view of the BW-I-A box-wing configuration.

Chapter 7

Future studies

Stability and controllability, stall conditions, aeroelasticity and flight dynamics, are among many other various fields in aeronautical engineering that lack of reliable deep researches in the box-wing's literature. An introduction of each field on box-wing configurations is presented in subsections 7.1 (aeroelasticity), 7.2 (structural effectiveness) and 7.3 (stability and control).

Moreover, in order to strengthen the aerodynamic behavior of the box-wing configuration for low Reynolds numbers, wind tunnel tests with scale models would involve significant advances in the investigation. Test models are completely determined with the geometric parameters. Therefore, it would be interesting to analyse the effect of various design parameters on aerodynamics, such as different angles of attack for each wing, uneven wingspans, a carefully implemented wing twist variation law, and decalage (i.e. relation between the incidence angle of both wings).

A static structural analysis would allow to determine the effects of applied loads on the whole wing configuration, so as to compute the deformations, internal forces and stresses. Such an analysis constitutes a key part of the engineering design, since the results obtained are then used to verify a structure's functionality. However, a more elaborated 3-D configuration would be required so as to perform a meaningful structural analysis, as well as a large computational effort given the type of structure a box-wing aircraft represents.

Therefore, in the present chapter, static aeroelastic phenomena is broached from simple introductory analytical procedures applied to a certain wing section, so that the results can be extrapolated as valid for the complete wing, so as to prepare the way for succeeding investigations.

7.1 Aeroelasticity

7.1.1 Introduction

Aeroelasticity is the branch of engineering that studies the interaction between aerodynamic and elastic forces (static aeroelasticity), and aerodynamic, inertia and elastic forces (dynamic aeroelasticity).

Aeroelastic studies represent an important aspect of aircraft design. In fact, wing torsional divergence and flutter are the two remarkable aeroelastic instabilities that critically affect structural integrity. Divergence occurs when static aerodynamic effects counteract the

torsional stiffness of the wings, whereas flutter is characterized by the oscillation of the wings due to the interaction between the different external forces.

Different features of box-wing aircraft are considered to have a benefitial influence on flutter. Many reports support the previous statement: considering different Mach numbers, Durham and Ricketts [5] found the dynamic pressure for the origin of flutter in joined-wing configurations to be about 1.6 times higher than that of cantilever wings; Weisshaar and Lee found that, as the sweep angle increases for a fixed span, the flutter dynamic pressure also increases.

Jemitola [27] investigated the effect on the structural design of the sweep at the end tip of a box-wing aircraft, concluding that it significantly affects the in-plane bending moment and shear force distributions in the wings, as opposed to those out-of-plane, in which only minor variations were observed. Furthermore, Fazelzadeh [28] studied the 2-D characteristics of a section of a box-wing aircraft and observed as well that the tip fin stiffness and sweep angle have a significant effect on the aeroelastic flutter.

Composite materials allow to modify the lift distribution and, consequently, the general behavior of the aircraft, by simply manipulating the ply angles (alternating the fiber layers' orientations) within the structure (aeroelastic tailoring). It is a special use of an aircraft's structural design process that consists on the embodiment of directional stiffness to control aeroelastic deformation, whether static or dynamic, so as to handle the flutter and divergence speeds of an aircraft.

7.1.2 Preliminar analysis

Air flow behaviour in between both wings of a box-wing aircraft can be exceptionally complex, and so is the aeroelastic analysis involved. Furthermore, bending and torsion equations are coupled for swept wings, so the examination of the problem becomes even more difficult.

In order to better study and understand the behavior of physical systems, mathematical models arise, in which wings are the starting point for the aeroelastic analysis as they are the most deformable structures.

The objective of the preliminar analysis is the modeling using the finite element method of the wing configuration. Thus, it is assumed that the behavior on the whole domain is an interpolation from certain values obtained at particular reference points, called nodes. Figure 7.1 details the problem under study, in which the fundamental aspect is the compatibility of torsion twist and vertical displacement at the vertical tip, so as to generate the stiffness matrix as a function of the general degrees of freedom considered (Equation 7.1).

$$\overrightarrow{u} = \{w, \quad \varphi_x, \quad \varphi_y\} \tag{7.1}$$

For each wing of the system, it is assumed that the functions that describe torsion twist and vertical displacement are polynomials, with the objective to transfer the solution obtained in the nodes to any point of the beam.

A sketch with the local coordinate system is employed (Figure 7.2) to determine the interpolation functions (hence, local degrees of freedom are set) for the fore wing, which, in this case, are polynomial (Equations 7.2 and 7.3).

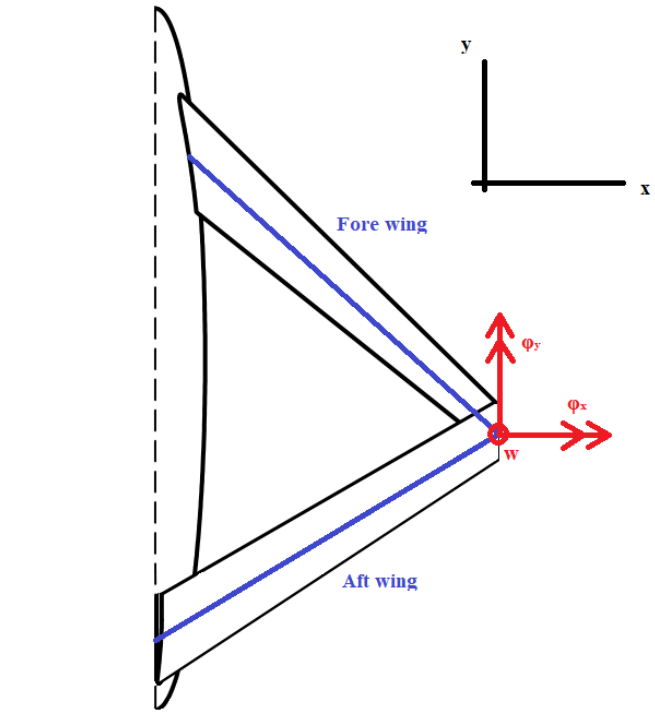

Figure 7.1: Structural analysis.

$$w(x) = a_0 + a_1 \cdot x + a_2 \cdot x^2 + a_3 \cdot x^3 \tag{7.2}$$

$$\theta(x) = x \cdot \theta_{fore} \tag{7.3}$$

To determine the coefficients, fixed conditions that ensure that the approximate solutions acquire the values of the variables in the nodes are needed (Equations 7.4).

$$w(l_{fore}) = w_{fore} \tag{7.4a}$$
$$w'(l_{fore}) = \varphi_{fore} \tag{7.4b}$$

In addition, boundary conditions must also be included in the resolution. That is: at the origin (x = 0), there is no movement nor rotation (Equations 7.5).

$$w(0) = 0 \tag{7.5a}$$
$$w'(0) = 0 \tag{7.5b}$$

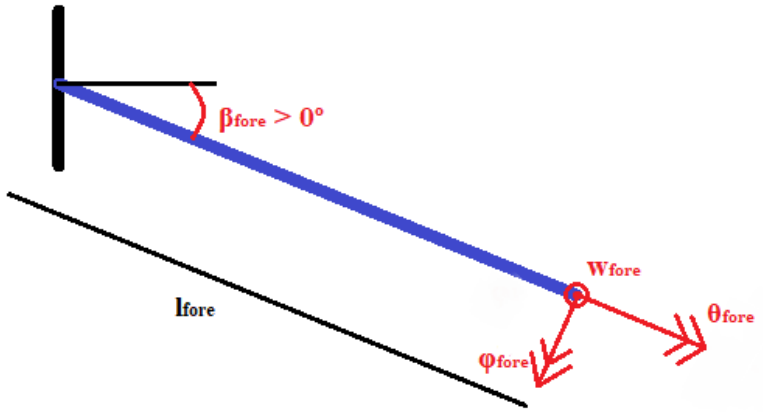

Figure 7.2: Fore wing sketch.

Altogether, the form functions that describe torsion twist and vertical displacement are shown in Equations 7.6.

$$w_{fore}(x) = N_w^T(x) \cdot \overrightarrow{z_{fore}} \tag{7.6a}$$

$$\theta_{fore}(x) = N_\theta^T(x) \cdot \overrightarrow{z_{fore}} \tag{7.6b}$$

$$\overrightarrow{z}_{fore} = \{w_{fore}, \quad \theta_{fore}, \quad \varphi_{fore}\} \tag{7.6c}$$

An analogous procedure is followed for the aft wing, for which the representative sketch in Figure 7.3 is used.

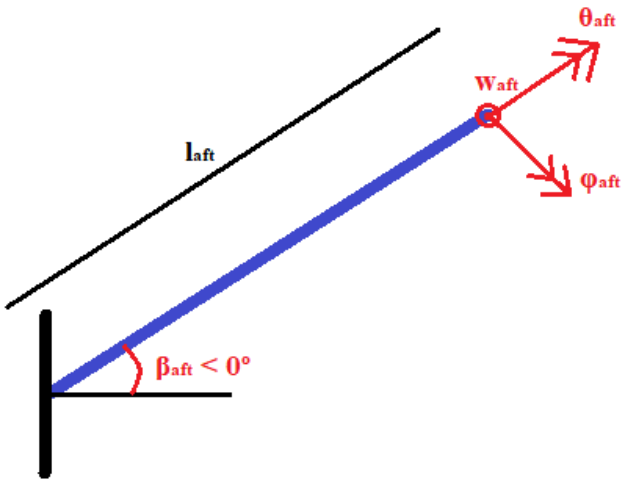

Figure 7.3: Aft wing sketch.

Then, local coordinates are translated into the general coordinates that define the whole system (Equation 7.7 for the fore wing).

$$\psi_{x_{fore}} = \theta_{fore} \cdot \cos(\beta_{fore}) - \varphi_{fore} \cdot \sin(\beta_{fore}) \tag{7.7a}$$

$$\psi_{y_{fore}} = -\theta_{fore} \cdot \sin(\beta_{fore}) - \varphi_{fore} \cdot \cos(\beta_{fore}) \tag{7.7b}$$

Again, an equivalent procedure is set for the aft wing. The rotation matrix that relates both local and general coordinate systems in both wings (i stands for fore or aft) is given in Equation 7.8.

$$\begin{Bmatrix} w_i \\ \varphi_{x_i} \\ \varphi_{y_i} \end{Bmatrix} = \begin{bmatrix} 1 & 0 & 0 \\ 0 & \cos(\beta_i) & -\sin(\beta_i) \\ 0 & -\sin(\beta_i) & -\cos(\beta_i) \end{bmatrix} \cdot \begin{Bmatrix} w_i \\ \theta_i \\ \varphi_i \end{Bmatrix} \rightarrow \overrightarrow{u}_i = T_i \cdot \overrightarrow{z}_i \tag{7.8}$$

Finally, compatibility can be established at the vertical tip (Equation 7.9)

$$\overrightarrow{u_{fore}} = \overrightarrow{u_{aft}} = \overrightarrow{u} \equiv \begin{Bmatrix} w \\ \varphi_x \\ \varphi_y \end{Bmatrix} \tag{7.9}$$

Approaching the problem from a purely energetic point of view, the internal deformation energy, which is the energy accumulated in the flexible parts of the system in its deformation, is calculated as stated in Equation 7.10. Therefore, the stiffness matrix of the structure is obtained (matrix K).

$$\begin{aligned} U = \frac{1}{2} \cdot \int_{x=0}^{l_{fore}} EI \cdot \left(\frac{d^2 w_{fore}(x)}{dx^2} \right)^2 \cdot dx + \frac{1}{2} \cdot \int_{x=0}^{l_{fore}} GJ \cdot \left(\frac{d\theta_{fore}(x)}{dx} \right)^2 \cdot dx + \\ + \frac{1}{2} \cdot \int_{x=0}^{l_{aft}} EI \cdot \left(\frac{d^2 w_{aft}(x)}{dx^2} \right)^2 \cdot dx + \frac{1}{2} \cdot \int_{x=0}^{l_{aft}} GJ \cdot \left(\frac{d\theta_{aft}(x)}{dx} \right)^2 \cdot dx \equiv \\ \equiv \frac{1}{2} \cdot \overrightarrow{z_{fore}^T} \cdot K_{fore} \cdot \overrightarrow{z_{fore}} + \frac{1}{2} \cdot \overrightarrow{z_{aft}^T} \cdot K_{aft} \cdot \overrightarrow{z_{aft}} \equiv \frac{1}{2} \cdot \overrightarrow{u^T} \cdot K \cdot \overrightarrow{u} \end{aligned} \tag{7.10}$$

To perform the aerodynamic analysis, Figure 7.4 is provided. It can be noted that, as a result of sweep, the effective angle of attack is altered by bending (Equation 7.11). This coupling between bending and torsion affect the static aeroelastic behaviour of the wings.

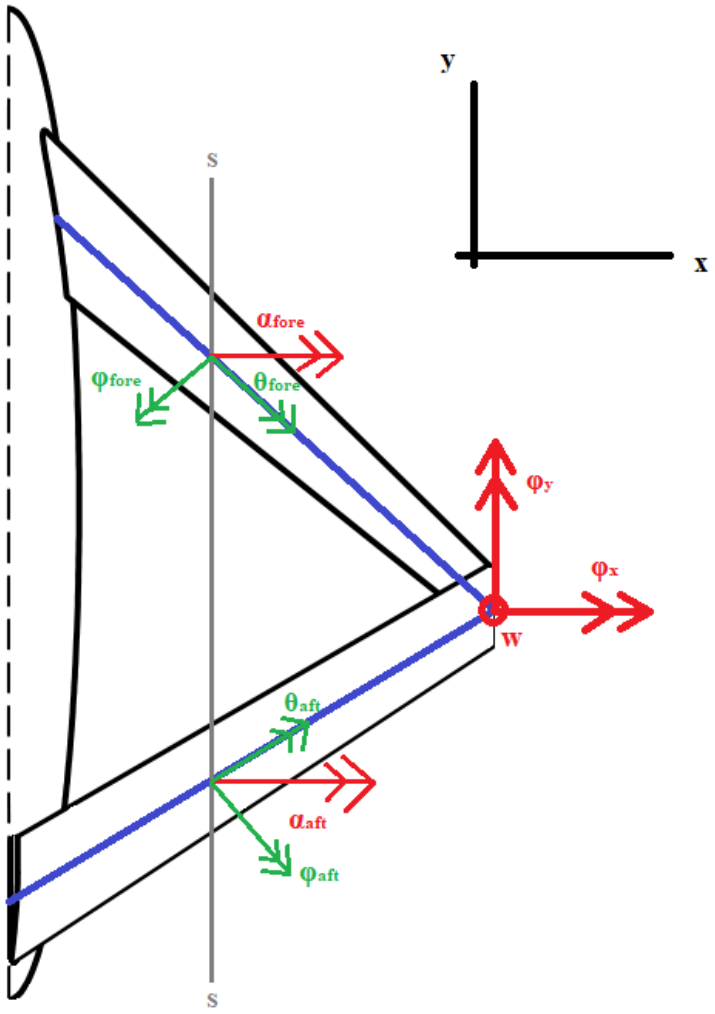

Figure 7.4: Effective angle of attack sketch.

$$\begin{aligned} \alpha_i(x) &= \theta_i(x) \cdot \cos(\beta_i) - \varphi_i(x) \cdot \sin(\beta_i) \\ &\equiv B_i(x) \cdot \overrightarrow{z_i} \equiv B_i(x) \cdot T_i \cdot \overrightarrow{u} \end{aligned} \tag{7.11}$$

The so-called panel method is used in order to divide the lifting surfaces up into panels, modelling the lift distribution using vortices (Figure 7.5). A whirl is placed at a quarter-chord from the leading edge (A) and its effect is studied at a quarter-chord from the trailing edge (B).

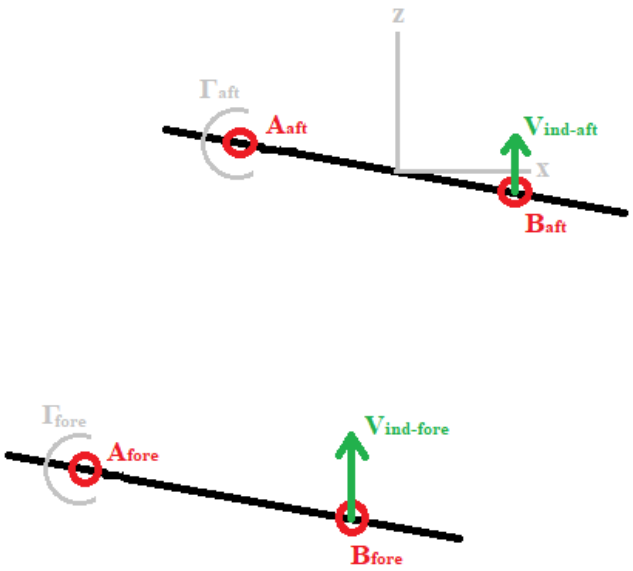

Figure 7.5: Panel method sketch.

The key calculation in such an approach is to determine the aerodynamic effect that each panel has on the other (Equation 7.12, where: i, j stand for fore and aft, respectively).

$$\begin{cases} L_i = q \cdot c_i(x) \cdot \left[C_{L_{\alpha ii}} \cdot \alpha_i(x) + C_{L_{\alpha ij}} \cdot \alpha_j(x) \right] \equiv q \cdot \overrightarrow{d}_i^T(x) \cdot \overrightarrow{u} \\ L_j = q \cdot c_j(x) \cdot \left[C_{L_{\alpha ji}} \cdot \alpha_i(x) + C_{L_{\alpha jj}} \cdot \alpha_j(x) \right] \equiv q \cdot \overrightarrow{d}_j^T(x) \cdot \overrightarrow{u} \end{cases} \tag{7.12}$$

The work of lift is measured on the displacements of the aerodynamic centres when the degrees of freedom (in this case, the vertical displacement of both aerodynamic centres) undergo a virtual displacement (Equation 7.13).

$$\delta W = \int_{x=0}^{l_{fore}} \delta w_{AC_{fore}} \cdot L_{fore} \cdot dx + \int_{x=0}^{l_{aft}} \delta w_{AC_{aft}} \cdot L_{aft} \cdot dx \tag{7.13a}$$

$$\delta w_{AC_i}(x) = \delta w_i(x) + \delta \alpha_i(x) \cdot e \equiv \overrightarrow{d}_i^T \cdot \delta u \tag{7.13b}$$

Then, the generalized forces associated with degrees of freedom are found, so the problem of divergence can be formulated (Equation 7.14).

$$Q = q \cdot \left[\int_{x=0}^{l_{fore}} \overrightarrow{d_{fore}}(x) \cdot \overrightarrow{d}_{fore}^T(x) \cdot dx + \int_{x=0}^{l_{aft}} \overrightarrow{d_{aft}}(x) \cdot \overrightarrow{d}_{aft}^T(x) \cdot dx \right] \cdot \overrightarrow{u} \equiv q \cdot A \cdot \overrightarrow{u} \tag{7.14a}$$

$$\frac{\delta U}{\delta u} = Q \rightarrow (K - q \cdot A) = 0 \tag{7.14b}$$

7.2 Structural effectiveness

There is considerable interest in the use of different unconventional non-planar aircraft designs, due to their potential benefits regarding structural characteristics.

For conventional cantilever wing configurations, the lift loads that must be resisted by the wing-fuselage structure usually include critical bending moments induced by the aerodynamic and weight loads on the wings. Actually, box-wing aircraft present design challenges in the matter of weight and structural interactions that significantly differ from conventional cantilever wing configurations.

7.2.1 Weight and structural features

Joined-wings differ from conventional wings in their external configuration, but also in their internal structure.

Wolkovitch revealed that the lift loading on each wing can be divided into a normal and a parallel component with respect to the truss structure formed by both wings (the rear wing root is located at a higher elevation than the front wing root) [29]. The system performs well under in-plane bending moments, but under out-of-plane components wings tend to bend forward about the tilted bending axis shown in Figure 7.6. Hence, the distribution of the structural elements should be as far away as possible from this axis, so the material must be concentrated near the upper leading edge and lower trailing edge to resist the wing bending. In fact, weight is reduced (and the strength-to-weight ratio is maximized) if the internal wing structure (structural box) is optimised occupying the section of the airfoil that comprises between the 5 % and 75 % of the chord (Figure 7.7), since it is restricted by the space needed for de-icing systems, high-lift devices and actuators.

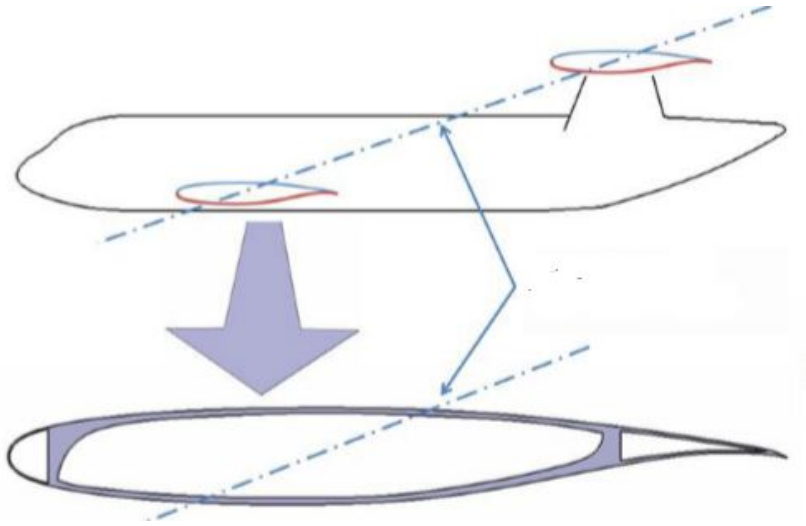

Figure 7.6: Tilted bending axis of a joined-/box-wing aircraft [30].

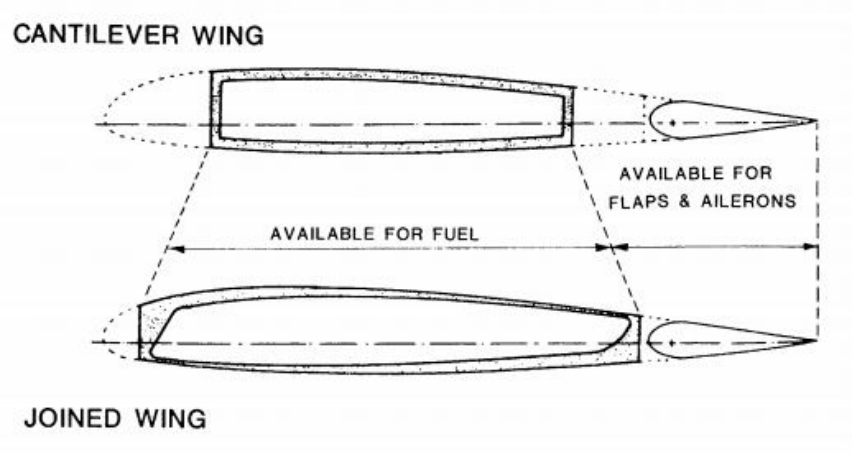

Figure 7.7: Optimum structural box design [29].

Muira showed through a parametric study that the structural weight of joined-wing aircraft firmly depends on the geometry and wing structural arrangement. Furthermore, Wolkovitch suggested that the structural weight could be minimised by increasing the wing dihedral/anhedral and using a high taper ratios. Other geometrical parameters also influence the overall structural weight, such as the tail height and the wing sweep (as explained in Subsection 2.3.1).

As for the connections of the rear and forward wing tips to the end fin, several researchers [31], [27] conclude that the greatest and most practical structural benefit occurs for fixed rigid joints (cantilever-like connections).

The truss structure formed by both wings represents a serious challenge for the rear wing, which suffers from combined bending and compression. Then, it must be designed with enough stiffness so as not to buckle [5]. Overall, the stiffness of a box-wing aircraft is elevated because the torsion of one wing is resisted by the flexural motion of the other.

Unfortunately, such an unconventional structure results in a structure that is extremely difficult to analyze. Together with the lack of detailed and reliable designs, companies have been reluctant to make important investments in the box-wing configuration, due to significant economical risks.

7.3 Stability and control

Stability and control are related to the actions required to achieve and ensure equilibrium in an aircraft.

Regarding box-wing configurations, Perez and Andrew [32] assessed the longitudinal stability. According to their study, longitudinal stability is achieved by either reducing the wing surface of the forward wing or moving the centre of gravity of the aircraft towards the nose. However, an unusual behaviour due to the asymmetric distribution of the downwash of both wings.

Wolkovitch [33] provided representations showing different modes of controlling a joined-wing aircraft (Figure 7.8).

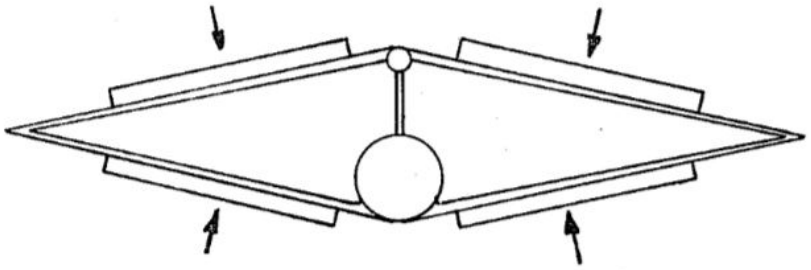

(a) Pitch control.

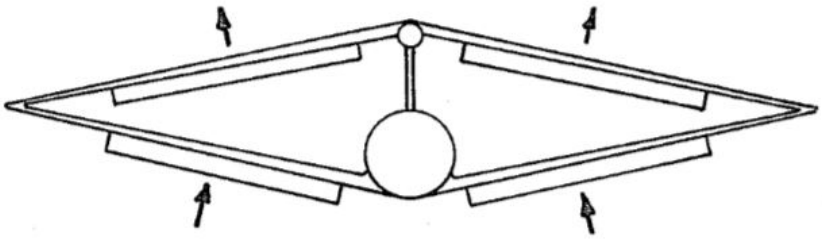

(b) Direct lift control.

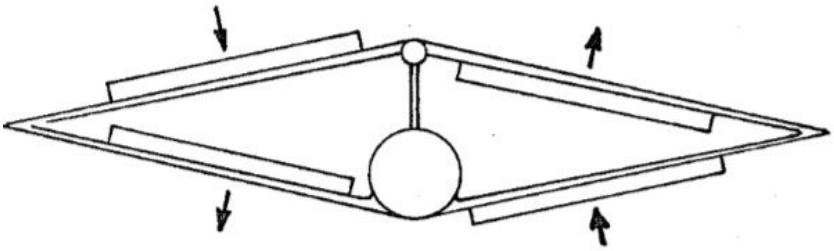

(c) Roll control.

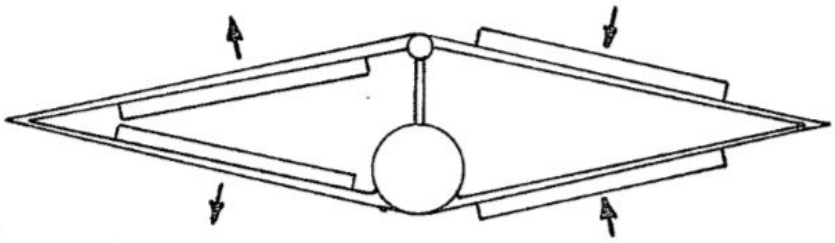

(d) Direct side-force control.

Figure 7.8: Modes of controlling a joined-wing aircraft.

Chapter 8

Budget

The budget is evaluated according to different estimates regarding the time spent by the author on each of the tasks in which the present project is divided (research, preliminary design, CFD simulations, analysis of the results and report writing).

The cost of IT equipment and software licenses used are also taken into account.

The theoretical wage related to the author of the document is estimated at 11.6 € per hour [34].

8.1 Project tasks costs

8.1.1 Information search process

Table 8.1 comprises the costs related to the research prior to the development of the project, as well as all the understanding of all the theoretical concepts involved.

	Labour time [h]	**Unit cost [€/h]**	**Sum total [€]**
Graduate engineer	63	11.6	730.8

Table 8.1: Information search process.

8.1.2 Design process

This subsection includes in Table 8.2 all costs related to the preliminary and final designs of the box-wing configuration, and in Table 8.3, those of the software licenses involved (some of which are free for personal use or more economical only for academic use).

	Labour time [h]	**Unit cost [€/h]**	**Sum total [€]**
Graduate engineer	138	11.6	1,600.8

Table 8.2: Design process: graduate engineer.

	Labour time [h]	Unit cost [€/year]	Sum total [€]
Fusion 360	12	0	0
MATLAB	105	500	500
Tornado	63	0	0

Table 8.3: Design process: software licenses.

8.1.3 CFD simulations

All costs with regard to every simulation, from the generation of the geometry, control volume and mesh, to the final results are included in the STAR-CCM+ software license. Simcenter STAR-CCM+ offers lots of flexibility with different licensing options. In the present project, its cost is estimated to be around 3,000 €.

8.1.4 Analysis of the results

The analysis of the results obtained and the drawing of the right conclusions are comprised in Table 8.4.

	Labour time [h]	Unit cost [€/h]	Sum total [€]
Graduate engineer	42	11.6	487.2

Table 8.4: Analysis of the results.

8.1.5 Report writing

This section deals with the production of the final report (Tables 8.5 and 8.6).

	Labour time [h]	Unit cost [€/h]	Sum total [€]
Graduate engineer	84	11.6	974.4

Table 8.5: Report writing: graduate engineer

	Labour time [h]	Unit cost [€/year]	Sum total [€]
Overleaf	84	0	0

Table 8.6: Report writing: software licenses.

8.2 IT equipment costs

The technological equipment used to carry out the project are basically a laptop and a desktop computer (Table 8.7). The laptop is a Lenovo IdeaPad 100-15IBD i5-5200U/6GB and the desktop computer is an HP Pavilion i5-2400/6GB.

	Labour time [h]	Unit cost [€/unit]	Sum total [€]
Laptop	348	579	579
Desktop computer	348	773.73	773.73

Table 8.7: IT equipment.

8.3 Total cost

The total cost amounts to eight thousand six hundred forty-five euros and ninety-three cents (Table 8.8).

	Sum total [€]
Information search process	730.8
Design process	2,100.8
CFD simulations	3,000
Analysis of the results	487.2
Report writting	974.4
IT equipment	1,352.73
Total	8,645.93

Table 8.8: Total cost.

Appendix A

Estimation of the significant parameters

A.1 Reference aircraft

		Wingspan [-]	Surface's ratio [-]	Sweep angle [º]	Dihedral angle [º]	Root chord [-]	Taper ratio [-]
JW-3	Forward wing	0.71	2.29	30.5	5	-	0.4
	Rearward wing			-32	-20	-	0.6
Boeing EX	Forward wing	1.23	-	40	16.1	0.17	0.39
	Rearward wing			-36.3	-11.1	0.22	0.74
PrandtlPlane	Forward wing	0.96	0.95	45	-	0.21	0.21
	Rearward wing			-30	-	0.18	0.18
Wolkovitch's	Forward wing	0.97	1.11	30	-	0.10	0.5
	Rearward wing			-25	-	0.13	0.74
Schiktanz's	Forward wing	1.03	1	28.5	6	-	0.24
	Rearward wing			-28	0	-	0.8

Table A.1: Significant parameters.

A.2 Mean aerodynamic chord

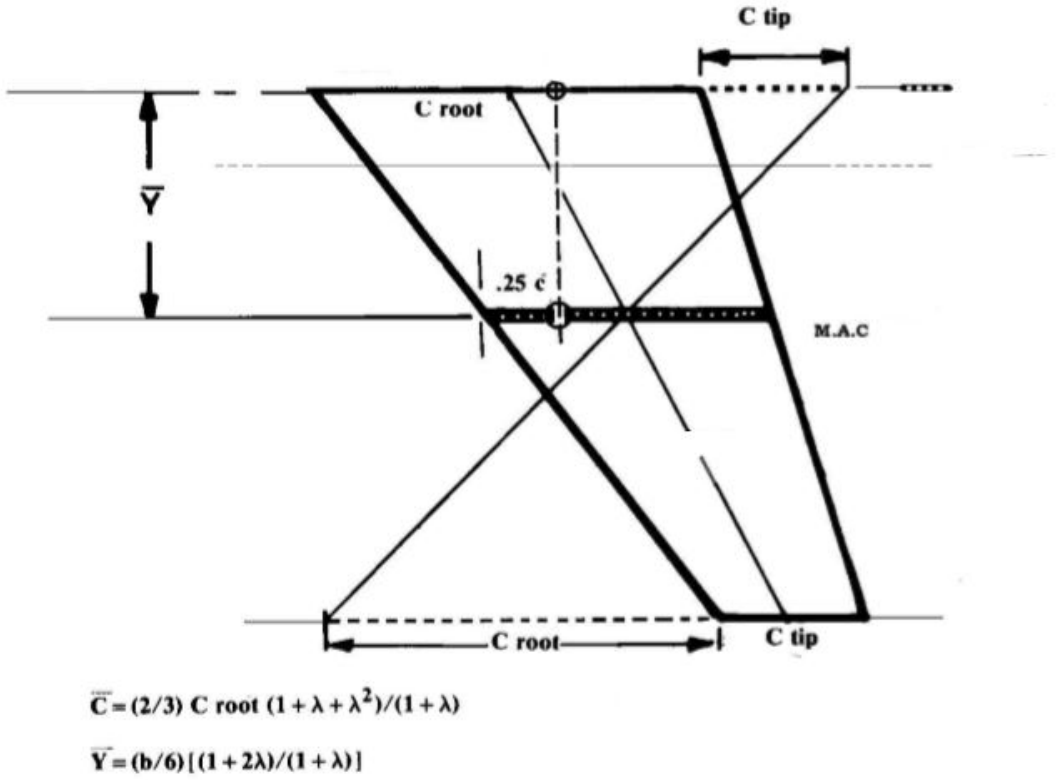

Figure A.1: Graphical procedure for calculating the MAC.

Bibliography

[1] European Commission. *Reducing emissions from aviation*. 2017. URL: https://ec.europa.eu/clima/policies/transport/aviation_en#tab-0-0.

[2] T. A. Boden, R. J. Andres, and G. Marland. "Global, Regional, and National Fossil-Fuel CO2 Emissions (1751 - 2013) (V. 2016)". In: (Jan. 2016). DOI: 10.3334/CDIAC/00001_V2016.

[3] Air Transport Action Group. *Facts & Figures*. 2020. URL: https://www.atag.org/facts-figures.html.

[4] T. Pruijsers. "Prandtl's best wing system". In: *Leonardo Times* (2013).

[5] J. R. Chambers. *Innovation in flight: research of the NASA Langley Research Center on revolutionary advanced concepts for aeronautics*. 2005.

[6] R. Cavallaro and L. Demasi. "Challenges, Ideas and Innovations of Joined-Wing Configurations: A Concept from the Past, an Opportunity for the Future". In: *Progress in Aerospace Sciences* (2016).

[7] J. Wolkovitch. *Application of the joined wing to cruise missiles*. Report ONR-CR212-266-1. Rancho Palos Verdes, California: Office of Naval Research, 1980.

[8] E. E. Larrabee. *7.4 Trim Drag in the light of Munk's Stagger Theorem*. Report N76 11021. NASA, 1975.

[9] I. Kroo. "Drag due to Lift: Concepts for Prediction and Reduction". In: *Annual Review of Fluid Mechanics Vol. 33* (2001), pp. 587–617.

[10] D. P. Raymer. *Aircraft Design: A Conceptual Approach*. American Institute of Aeronautics and Astronautics, Inc., 1992.

[11] B. Maggin and R. E. Shanks. *The effect of geometric dihedral on the aerodynamic characteristics of a 40° swept-back wing of aspect ratio 3*. Technical note 1169. Langley Memorial Aeronautical Laboratory Langley Field, VA: National Advisory Committee for Aeronautics, 1947.

[12] L. Prandtl. *Induced drag of multiplanes*. Report 182. NACA, 1924.

[13] I. Kroo. "Nonplanar wing concepts for increased aircraft efficiency". In: *VKI lecture series on Innovative Configurations and Advanced Concepts for Future Civil Aircraft* (2005).

[14] S. A. Andrews and R. E. Perez. "Parametric Study of Box-Wing Aerodynamics for Minimum Drag Under Stability and Maneuverability Constraints". In: *33rd AIAA Applied Aerodynamics Conference*. Royal Military College of Canada. Kingston, Ontario, Canada: American Institute of Aeronautics and Astronautics, Inc., June 2015.

[15] T. Chau and D. W. Zingg. *Aerodynamic Shape Optimization of a Box-Wing Regional Aircraft Based on the Reynolds-Averaged Navier-Stokes Equations*. Toronto, Ontario, Canada: Institute for Aerospace Studies, University of Toronto.

[16] J. D. Anderson Jr. *Fundamentals of Aerodynamics*. Avenue of the Americas, New York, NY: McGraw-Hill, 2011.

[17] A. Filippone. "Data and performances of selected aircraft and rotorcraft". In: *Progress in Aerospace Sciences* (2000).

[18] I. Kroo. "Highly Nonplanar Lifting Systems". In: *Transportation Beyond 2000: Technologies Needed for Engineering Design* (1995), pp. 331–370.

[19] I. Kroo and J. Gallmant. *Aerodynamic and Structural Studies of Joined-Wing Aircraft*. Report 1. Moffett Field, CA: NASA Ames Research Center, 1990.

[20] A. Frediani et al. "Development of a PrandtlPlane aircraft configuration". In: ().

[21] D. Schiktanz. "Conceptual Design of a Medium Range Box Wing Aircraft". Master Thesis. Hamburg University of Applied Sciences, 2011.

[22] S. C. Smith and R. K. Stonum. *Experimental Aerodynamic Characteristics of a Joined-Wing Research Aircraft Configuration*. Technical note 89-24285. National Aeronautics and Space Administration, 1989.

[23] E. Torenbeek. *Synthesis of Subsonic Airplane Design*. Springer-Science+Business Media, B. V., 1982.

[24] Airfoil Tools. *NACA 2412 (naca2412-il)*. URL: `http://airfoiltools.com/airfoil/details?airfoil=naca2412-il`.

[25] T. Melin. "A Vortex Lattice MATLAB Implementation for Linear Aerodynamic Wing Applications". Master Thesis. Royal Institute of Technology (KTH), 2000.

[26] D. Schitktanz and D. Scholz. "Box wing fundamentals - An aircraft design perspective". In: *Deutscher Luft- und Raumfahrtkongress*. Hamburg University of Applied Sciences. Hamburg, Germany, Sept. 2011.

[27] P. O. Jemitola, J. Fielding, and P. Stocking. "Joint fixity effect on structural design of a box wing aircraft". In: *The Aeronautical Journal 116* (2012), pp. 363–372.

[28] S. A. Fazelzadeh et al. "Flutter characteristics of typical wing sections of a box wing aircraft configuration". In: *Advanced Aircraft Efficiency in a Global Air Transport System (AEGATS 2018)* (2018).

[29] J. Wolkovitch. "The Joined Wing: An Overview". In: *Journal of Aircraft, 23rd* (1986), pp. 161–178.

[30] P. Jemitola and P Okonkwo. "Review of Structural Issues in the Design of a Box Wing Aircraft". In: *Journal of Aerospace Engineering and Mechanics* (2019), pp. 161–166.

[31] H. Lin, J. Jhou, and R. Stearman. "Influence of joint fixity on the structural static and dynamic response of a joined-wing aircraft". In: *31st AIAA/ASME/ASCE/AHS/ASC* (1990).

[32] S. A. Andrews and R. E. Pérez. "Analytic study of the conditions required for longitudinal stability of dual wing aircraft". In: *Journal of Aerospace Engineering 232* (2018), pp. 213–246.

[33] J. Wolkovitch. "Joined wing aircraft". United States Patent 4,365,773. 1980.

[34] Ministerio de Trabajo Migraciones y Seguridad Social. "III. Otras disposiciones". In: *Agencia Estatal Boletín Oficial del Estado Núm. 251* (Viernes 18 de octubre de 2019), Sec. III. Pág. 114772.